

Dissertation
submitted to the
Combined Faculties for the Natural Sciences and for
Mathematics
of the Ruperto-Carola University of Heidelberg, Germany
for the degree of
Doctor of Natural Sciences

presented by
Diplom-Physicist Jens Kessler
born in Dillingen/Saar

Oral examination: 31.10.2007

**Search for Drell Yan
in $\sqrt{s} = 41.6$ GeV p-N Collisions
at HERA-b**

Referees:

Prof. Dr. Franz Eisele
Prof. Dr. Karl-Tasso Knöpfle

Abstract

In this thesis, the data taken with the HERA-b detector in the running period 2002/2003 is used to measure the cross section of the Drell Yan process $q\bar{q} \rightarrow l^+l^-$, where quark and antiquark annihilate and produce a lepton pair. HERA-b, a fixed target spectrometer, is one of the four experiments at the storage ring HERA at DESY. It uses the proton beam to produce collisions with wire targets of different materials.

The main challenge of the thesis is to extract a Drell Yan signal from the dataset without losing too many events and to find a suitable background simulation which can be subtracted from the kinematical distributions. For this purpose, a Single Track Monte Carlo is generated to calculate event weights, which are applied to the likesign dataset. This procedure is necessary since the detector acceptance of HERA-b is dependant on the charges of the leptons.

After background subtraction and acceptance and luminosity corrections, differential cross sections of the Drell Yan process are plotted, for the first time in the negative x_F regime. These are compared to results from E772 and NA50. Also, the dependance of the Drell Yan cross section on the mass number of the target material is calculated.

Kurzfassung

Im Rahmen dieser Arbeit werden Daten, die am HERA-b Detektor gesammelt wurden, benutzt um den Wirkungsquerschnitt des Drell Yan Prozesses $q\bar{q} \rightarrow l^+l^-$ zu messen. Bei diesem Prozess annihilieren Quark und Antiquark und bilden ein Leptonenpaar. HERA-b ist ein Fixed-Target Experiment am Speicherring HERA am DESY in Hamburg. Dort wird der Protonenstrahl von HERA mit Drähten aus verschiedenen Materialien zur Kollision gebracht.

Die größte Herausforderung dieser Arbeit ist, aus den Daten das Drell Yan Signal zu extrahieren, ohne zuviele Ereignisse zu verlieren. Ausserdem muss eine geeignete Untergrundsimulation gefunden werden, um in den kinematischen Verteilungen den Untergrund abziehen zu können. Zu diesem Zweck werden Ereignisse mit Leptonenpaaren gleicher Ladung mit Gewichten versehen, die aus einer speziellen Einzelspur-Monte Carlo Simulation gewonnen werden. Diese Gewichte sind notwendig, da die Akzeptanz des HERA-b Detektors von der Ladung der Leptonen abhängig ist.

Nach der Subtraktion des Untergrundes und der Korrektur auf Detektorakzeptanz und Luminosität werden differentielle Wirkungsquerschnitte gezeigt, die zum ersten Mal im negativen x_F Bereich gemessen wurden. Diese werden mit Ergebnissen der Experimente E772 und NA50 verglichen. Ausserdem wird die Abhängigkeit des Drell Yan Wirkungsquerschnitts von der Massenzahl des Materials, in dem die Wechselwirkung stattfindet, berechnet.

Contents

1	The HERA-b Experiment	7
1.1	Storage Ring	7
1.2	HERA-b	8
1.2.1	Target	10
1.2.2	Vertex Detector	11
1.2.3	Tracking	11
1.2.4	Ring Imaging Cherenkov Detector	13
1.2.5	Electromagnetic Calorimeter	13
1.2.6	Muon System	14
1.2.7	Trigger	17
2	Drell Yan Theory	19
2.1	The Drell Yan Process	19
2.2	Quark Parton Model and Pertubative QCD	20
2.3	Angular Distributions	24
2.4	Violation of the Lam Tung Relation	25
2.4.1	Higher Twist Contributions	29
2.4.2	Spin and p_t Correlations of Quarks	30
3	Data Selection & Background Subtraction	33
3.1	Event Selection	35
3.2	Event Mixing to Simulate Background	36
3.3	Likesign Data as Background	39
3.3.1	Acceptance Differences between Likesign and Unlikesign Data	39
3.3.2	Corrections for the Acceptance Difference of Opposite- and Likesign Data	45
3.3.3	Single Track Monte Carlo to calculate Acceptance Correc- tion Factors	46
3.3.4	Reweighting of Likesign Data to the Acceptance of the Op- posite sign Background	52
3.3.5	Crosscheck of Acceptance Reweighting Method	56
3.4	Simulation of the Drell Yan Process	60
3.5	Optimization of Event Selection	65

3.5.1	Consecutive Kinematic Cuts	65
3.5.2	Further Geometrical Cuts	70
3.5.3	Cut on Event Likelihood	73
3.5.4	Final Data Sample	75
3.6	Electron Data	76
4	Determination of Cross Sections	79
4.1	Luminosity Determination	79
4.2	$\Upsilon(1S)$ Cross Section	84
4.3	Detector Acceptances	87
4.4	Acceptance corrected Kinematic Distributions	89
4.5	Systematic Checks of the Mass Distribution	93
4.6	Angular Distributions	98
4.7	Comparisons with other Experiments	100
4.7.1	E772	100
4.7.2	NA50	102
4.8	Systematic effects	104
5	Conclusions	107
	List of figures	111
	List of tables	113
	Bibliography	115

Chapter 1

The HERA-b Experiment

1.1 Storage Ring

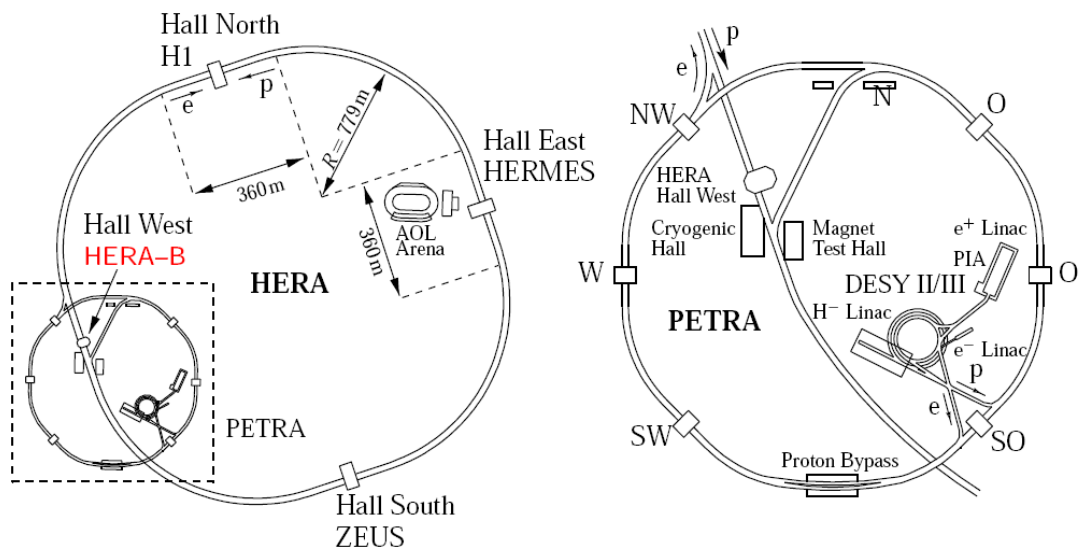


Figure 1.1: Overview of the HERA accelerator complex. The left side shows HERA with the four experiments, the right side shows an enlarged view of the PETRA preaccelerator and the injection points into HERA ([Des00]).

The storage ring HERA (Hadron-Elektron Ringanlage – hadron electron ring facility) is an electron proton collider at DESY (Deutsches Elektronen Synchrotron – german electron synchrotron) in Hamburg. A schematic view is shown in Fig. 1.1. HERA consists of two separate rings sharing a tunnel measuring 6.3 km in circumference, one for protons and one for electrons or positrons. Protons are accelerated to 920 GeV, electrons in the opposite direction to 27.5 GeV.

The two beams are brought to collision at two points along the accelerator. At these points, the two largest experiments, H1 and ZEUS are situated. Both use the e-p collisions to measure the proton structure functions via deep inelastic scattering of the electrons. The HERA-b experiment is located in Hall West and utilizes the proton beam only, while the fourth experiment at HERA, HERMES only uses the electron beam which is polarized before reaching it.

The proton beam is divided into bunches of 30 cm length. The circumference of the storage ring can accommodate 220 of such bunches. The time between two bunches crossing the interaction region is 96 ns. Only 180 bunches are filled with protons, as the preaccelerator PETRA (Positron-Elektron-Tandem-Ring-Anlage – Positron Electron Tandem Ring Facility) can only contain 60 bunches at a time. The other 40 bunches remain empty.

1.2 HERA-b

The HERA-b detector is one of the four experiments at HERA. Unlike the experiments H1 and ZEUS which examine electron proton collisions, HERA-b is a fixed target experiment where the proton beam is brought into collision with wire targets of different materials. The original physics goal was to measure CP violation in neutral B mesons via the “golden decay” channel, where a neutral B meson decays into J/ψ and K_S^0 ([Abt94]).

A schematic view of the detector is given in Fig. 1.2. In the picture, the protons enter the detector from the right. The first component interacting with the proton beam is the wire target. The silicon strip vertex detector (VDS) shares the vacuum vessel with the wire target. Behind the VDS, the tracking system starts which consists of an Inner Tracker (ITR) and an Outer Tracker (OTR). After the first tracking station, a magnet with a field strength of 0.85 T and a horizontal deflection plane is situated. At the far end of the tracking system, a Ring Imaging Cherenkov detector (RICH) and an electromagnetic calorimeter (ECAL) provide particle identification. Behind the last tracking station follows the muon system, consisting of detector stations and layers of absorbing material.

The coordinate system of HERA-b has the z axis pointing in direction of the proton beam, the y axis up and the x axis to the left, to the center of the storage ring.

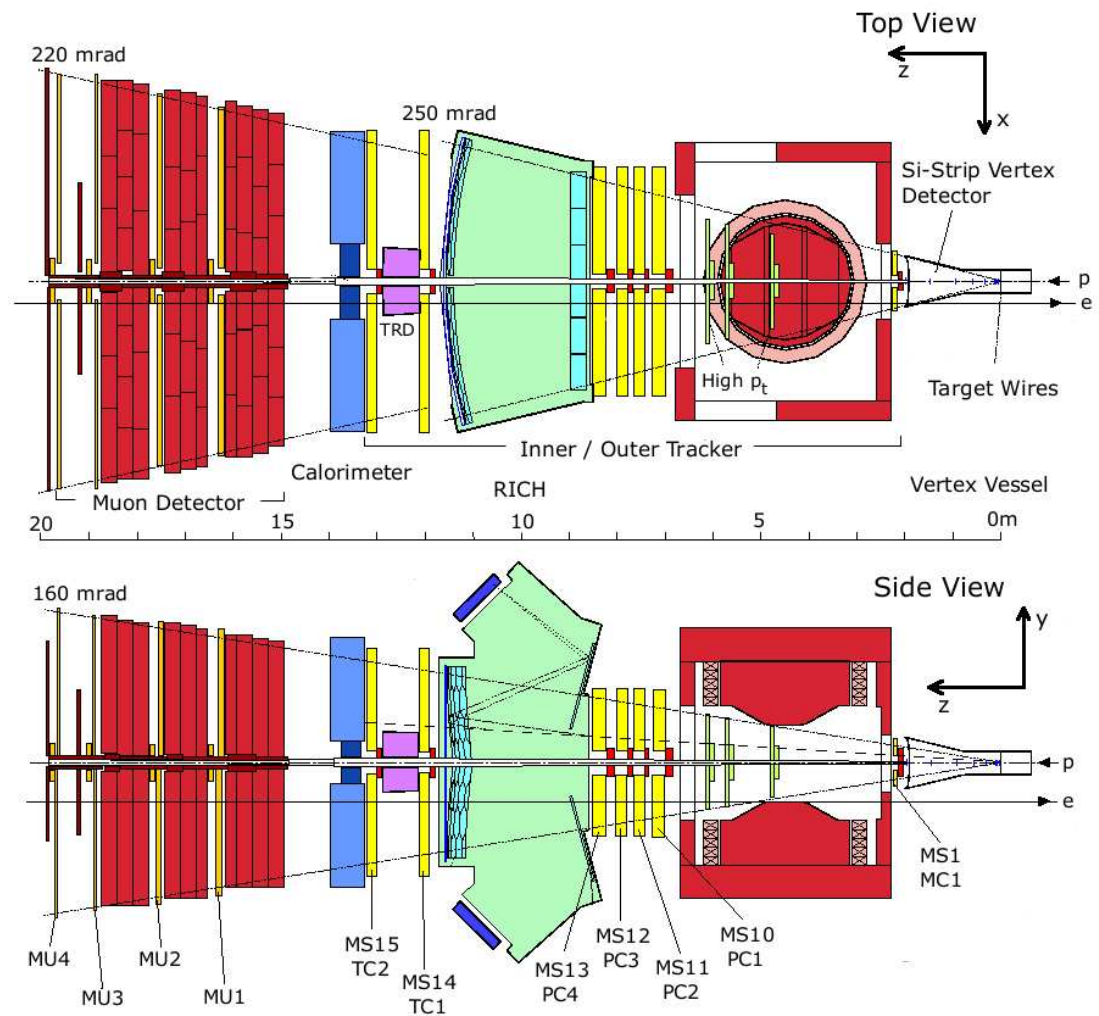


Figure 1.2: Schematic overview of the detector ([Spe04]). The top picture shows a view from above the detector, the bottom picture from the side. The detector components and tracking stations are labelled.

1.2.1 Target

The wire target system consists of two stations with four wires each. Wires made of different materials can be used in these stations. Carbon, Tungsten, Titanium, Palladium and Aluminum wires were installed during the data taking period. Only Carbon and Tungsten wires were inserted into the beam in lepton triggered runs which were used in this analysis for a significant amount of time. The wires are moved perpendicular to the beam by a target steering system. Charge integrators on each wire are used to measure the current interaction rate, which is kept constant by the steering system. If the beam position changes during a run, the interaction rate changes and the steering system adjusts the wire position until the nominal interaction rate is restored. The target wires are only moved into the outer halo of the proton beam in order not to disturb the beam to keep it usable for the collision experiments. More than one wire can be used at a time, which is important for target mass dependance studies. Fig. 1.3(a) shows a schematic drawing of the vacuum vessel containing the vertex detector and the target stations. In Fig. 1.3(b), the reconstructed primary vertex positions mea-

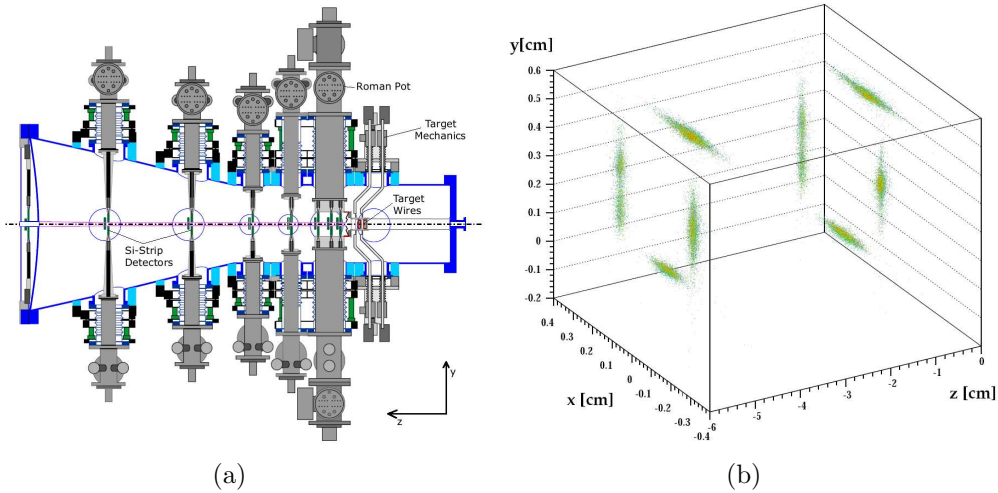


Figure 1.3: (a): Schematic view of the vertex detector and the target system ([Brü01]). Protons enter the system from the right. (b): Reconstructed primary vertex positions during a special multiwire run which used all eight target wires ([Mas00]).

sured during a special run using all eight wires are plotted. The position of the eight wires can easily be distinguished.

1.2.2 Vertex Detector

The silicon strip based vertex detector shares a vacuum vessel with the wire target. It consists of eight superlayers of detectors which contain four modules each. Two double sided microstrip detectors mounted orthogonally make up one module. The first seven superlayers are mounted on roman pots which can retract the detectors from the beam during machine studies and proton injection. The eighth superlayer is in front of the exit window of the vacuum vessel. With all superlayers in their nominal position, the angular acceptance of the VDS extends from 10 to 250 mrad.

Monte Carlo simulations have shown that the vertex resolution achieved by the VDS is roughly $50 \mu\text{m}$ perpendicular to and $500 \mu\text{m}$ along the beam axis. These values were confirmed in data taken in 2000. [Bau03] gives a value of $530 \pm 40 \mu\text{m}$ for the resolution along the beam axis in data.

1.2.3 Tracking

The tracking system is responsible for connecting hits in muon chambers, RICH and ECAL to vertices found in the VDS. Also, particle momenta can be measured in conjunction with the dipole magnet. Two separate detector systems make up the tracking system. The Inner Tracker covers the inner part of the detector up to a distance of about 30 cm to the beampipe, the Outer Tracker the rest of the acceptance of 250 mrad in the horizontal plane and 160 mrad in the vertical. The tracking system consists of seven stations. One station (MS1/MC1) is placed in front of the magnet, four (MS10/PC1 to MS13/PC4) between magnet and RICH, and two (MS14/TC1 and MS15/TC2) between RICH and ECAL. The names given in parentheses are the names of the Inner and Outer Tracker modules in each station.

Inner Tracker

The Inner Tracker consists of MicroStrip Gaseous Chambers (MSGC). MSGCs are a type of drift chamber, where both anodes and cathodes are in the form of alternating strips of conductive material on a glass plate. A schematic view of such a chamber is shown in Fig. 1.4. The ionization produced by charged particles crossing the chamber drifts to the glass plate. The charge is multiplied in the field between anodes and cathodes. Extensive ageing tests have shown that MSGCs of the size used in HERA-b ($25 \times 25 \text{ cm}^2$) suffer from severe damage in hadronic environments. Large gains are needed to reach an acceptable ratio of signal to noise, which increases the danger of damage to the strip anodes by large discharges caused by heavily ionizing particles. Thus, a gas electron multiplier (GEM) foil was introduced which provides a second signal amplification step and

reduces the gain factor needed at the microstrip plates.

During the shutdown 2000/2001, the ITR chambers were removed from the de-

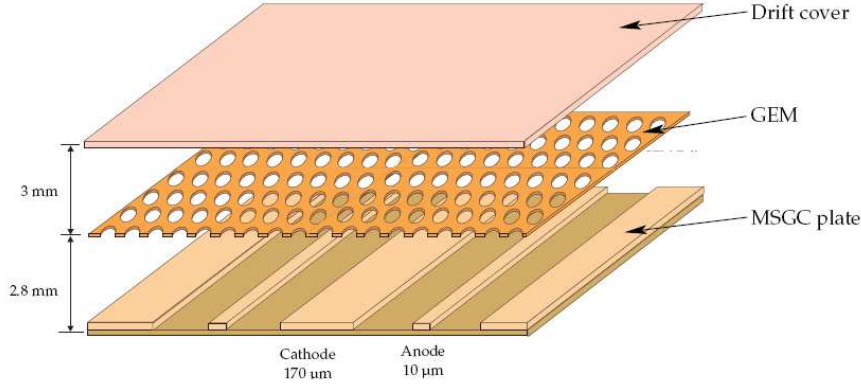


Figure 1.4: *Schematic representation of a GEM MSGC ([Bag02]). The main gas gain occurs on the MSGC plate at the anode. By applying a second high voltage to the two sides of the GEM foil, an additional source of gain is introduced which allows the gain on the MSGC plate to be lowered. The drift cover is used as a cathode and to seal the gas volume.*

tector to upgrade the readout electronics of the chambers included in the trigger chain. Unfortunately, during the reattachment of the electronics to the chambers a problem occurred with the conducting glue used for the bonding. Not all readout strips were connected to the electronics. In stations MS10, MS13 and MS15, between 50 – 60% of the readout channels were not usable, in stations MS11, MS12 and MS14, 18% of channels were dead. Station MS01 was relatively unaffected, only 8% of the strips were not read out ([Gor03]).

Outer Tracker

The Outer Tracker is made up of small drift chambers with a hexagonal profile (“honeycomb”) of two diameters. The honeycomb profile, the construction method and the cross section of a single and a double layer section are illustrated in Fig. 1.5. The inner chambers consist of drift volumes of 5 mm diameter, the outer ones are 10 mm in diameter. Each drift volume contains a wire along the main axis as the anode, while the hexagonal walls made out of conducting foil function as cathode. Stereo layers¹ provide position information in the direction of the y axis, along the wires.

¹Stereo layers are detector layers rotated along the beam axis by $\pm 5\%$ with respect to the vertical orientation of the standard chambers.

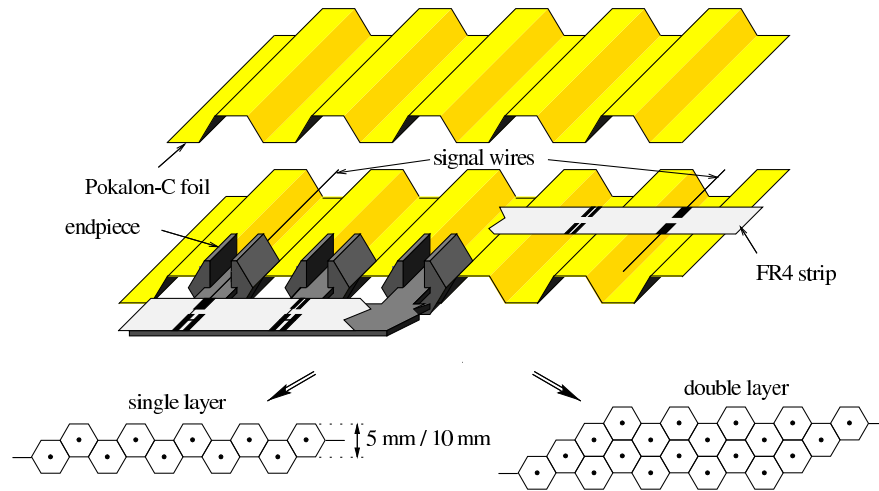


Figure 1.5: Illustration of the honeycomb structure used for the Outer Tracker ([Otr02]). The top picture shows the construction out of two layers of preshaped material, the lower sketch shows the geometry of a single and a double layer.

1.2.4 Ring Imaging Cherenkov Detector

The RICH detector uses the Cherenkov effect to separate light particles (e.g. pions and muons) from heavier ones (kaons, protons). Charged particles emit photons at the Cherenkov angle $\theta_C = \arccos(1/\beta n)$ when travelling through a medium of refractive index n if their speed is larger than the speed of light in the medium, or if $\beta > 1/n$. The RICH focuses these photons using a series of spherical and planar mirrors onto a focal plane outside the acceptance of the detector, where they are detected via photomultipliers. Photons coming from a single particle form a ring in the focal plane.

Fig. 1.6(a) shows a cross section of the RICH detector. The mirrors and the path of the Cherenkov photons are shown. Fig. 1.6(b) is a plot of the relation between particle momentum and Cherenkov angle for several particle types. Pions, kaons and protons are clearly separated up to a momentum of 40 GeV.

1.2.5 Electromagnetic Calorimeter

The electromagnetic calorimeter used at HERA-b is built using cells stacked in Shashlik style. Layers of plastic scintillators and absorber plates are assembled in sandwich fashion. The area covered by the ECAL is divided into three concentric areas: outer, middle and inner. These areas are shown in Fig. 1.7(a). Cells in the outer area are the largest at $11.18 \times 11.18 \text{ cm}^2$. middle ECAL cells are smaller, $5.59 \times 5.59 \text{ cm}^2$, while cells in the inner part, where the track density is highest,

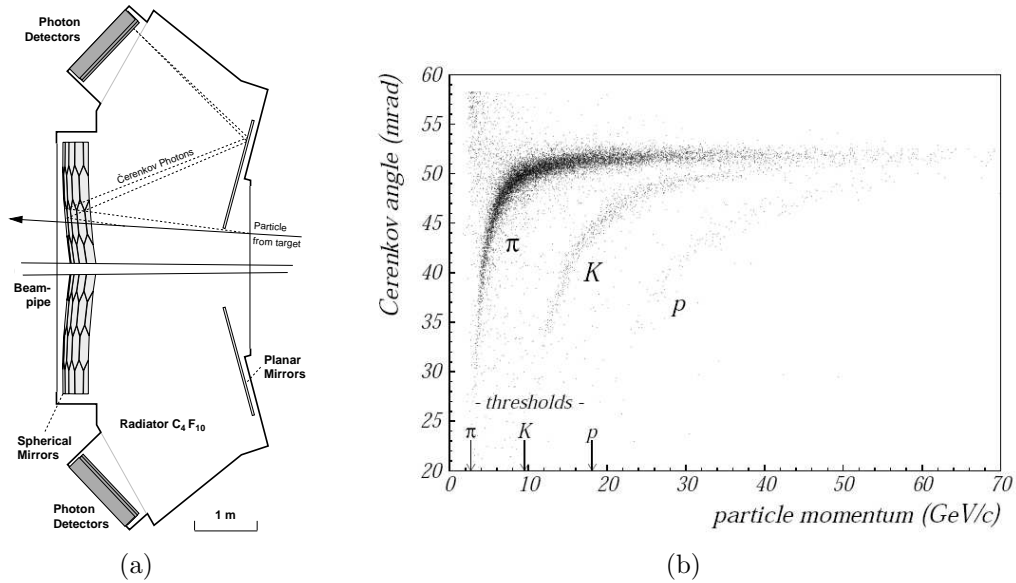


Figure 1.6: (a): Schematic view of the Ring Imaging Cherenkov Detector. Protons enter the system from the right. (b): Cherenkov angle of pions, kaons and protons depending on momentum. A clear separation between the three particles is seen (both figures [Ari04]).

are $2.24 \times 2.24 \text{ cm}^2$. Due to the difference in flux between outer and inner detector, different materials were used. Both outer and middle cells are built out of lead absorber and standard plastic scintillators, while the cells in the inner part consist of a radiation hard polystyrene based material and absorbers made out of a tungsten iron nickel alloy. The scintillation photons created by the impact of a charged particle are guided by wavelength shifter rods to photomultiplier tubes behind the sandwich cells. Each cell has its own photomultiplier tube. A schematic drawing of a cell is given in Fig. 1.7(b).

1.2.6 Muon System

The muon system consists of four stations. In front of the first three stations, hadron absorbers made of iron are placed. There is only a small absorber between station three and four to increase the precision of the track measurement and remove uncertainties induced by multiple scattering. Similarly to the tracking system, the muon system also consists of an inner and an outer part. The inner detector in all stations consists of gas pixel chambers of size $9 \times 9 \times 30 \text{ mm}^3$. Each station contains five wires oriented along the beam axis, a central anode wire and four thicker potential wires.

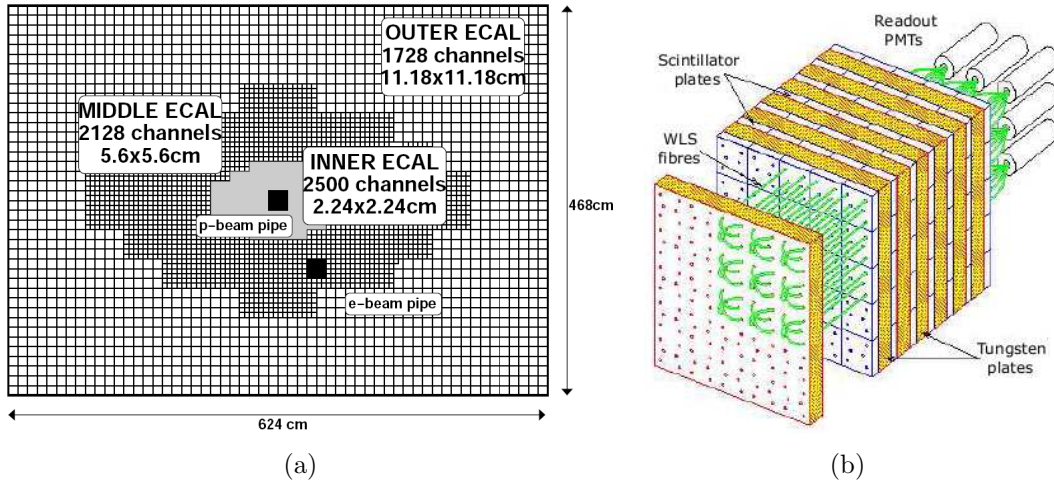


Figure 1.7: (a): Schematic overview of the three detector regions of the ECAL ([Bru02]. (b): Overview of a single detector cell of the ECAL ([Har95]).

The outer muon detector part uses two different technologies. Each of the first two stations (MU1 and MU2) consists of three layers of tube chambers. These are built from closed cell proportional wire chambers. The last two stations use pad chambers. These are similar to the tube chambers but are built from an aluminum profile open on one side, which is closed by a panel containing additional cathode pads. These pads are used in the muon pretrigger. Since there is no large absorber between the two stations, a coincidence between two pads can be required to cause a pretrigger signal. A cutout schematic drawing of the detector is shown in Fig. 1.8.

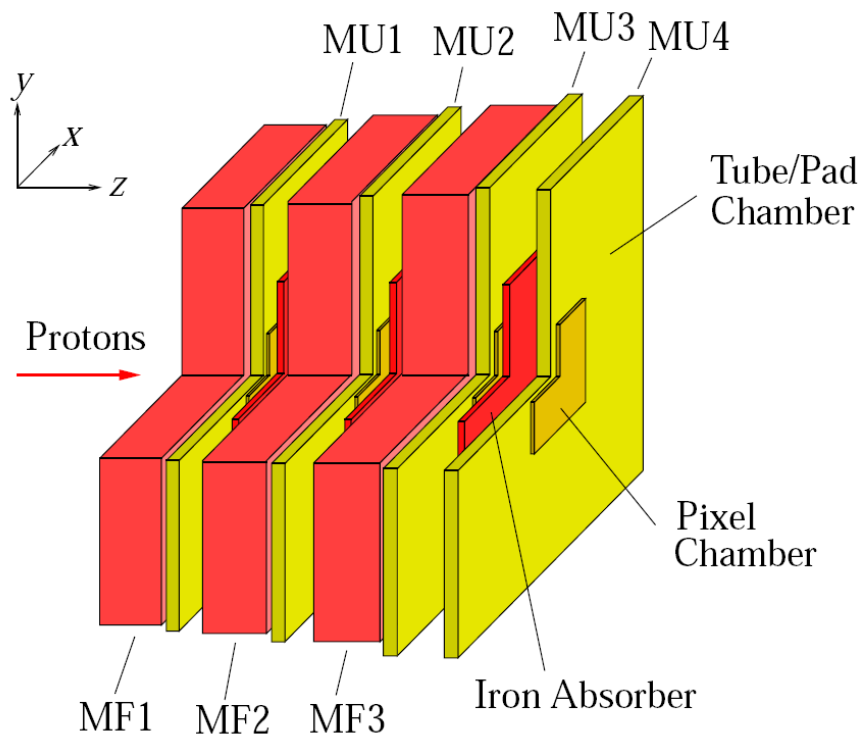


Figure 1.8: *Cutout illustration of the muon stations ([Hus05]). The four stations consisting of inner pixel and outer tube/pad chambers and the three large iron/concrete absorbers in front of stations MU1, MU2 and MU3 are shown.*

1.2.7 Trigger

The trigger system at HERA-b has two methods of operation. The first one is the Minimum Bias trigger mode which is an interaction trigger that discards empty events without enriching any special physics states. The second one was designed to trigger the decay products of the “golden decay” of the B meson. These are lepton pairs produced by the decay of a J/ψ . Both triggers were used at different times in the data taking period of 2002-2003, but only data taken with the dilepton trigger is used in this analysis.

The dilepton trigger consists of several stages which reduce the event rate from the maximum of 10.4 MHz down to the rate of 1 kHz at which events can be written to the data storage system. For further information, see [Dam04].

Pretrigger

The pretrigger system is designed to find two tracks with large transverse momentum. The muon pretrigger uses data from the last two muon stations and searches for coincidental pad hits in both stations which show a large p_t . The electron pretrigger looks for two ECAL clusters, again with sufficiently large p_t . If either pretrigger finds two candidates in an event, the information is passed on to the First Level Trigger stage. The muon pretrigger suffers from a low overall efficiency of roughly 10%. The main contribution to this is the efficiency of the muon pads, which is on average 40% when requiring two coincident hits in stations MU3 and MU4. The efficiency of the muon pretrigger was studied in [Hus05].

First Level Trigger (FLT)

The First Level Trigger is implemented by custom made electronic boards dedicated to a fast reconstruction of tracks starting with the pretrigger candidates. Hits in the muon stations MU4, MU2 and MU1 and in the tracking stations TC2, TC1, PC4 and PC1 are used, in that order. Starting out from the pretrigger message in either the muon system or the ECAL, the algorithm (similar to a Kalman filter algorithm) follows the tracks iteratively from station to station by defining regions of interest (RoI) in the next chamber based on the hit in the current and all previous chambers. Hits in all stereo layers of the tracking stations are required to improve track quality and reduce the event rate.

The FLT can be used in two modes, as a count trigger where the trigger decision is based on the number of events surviving the FLT track criteria, or as a pair trigger, where a minimum reconstructed mass of a track pair can be required. During the data taking period of 2002/2003, the FLT was set to count trigger mode with a single track as the requirement.

The data is transferred between the components of the FLT via optical links.

These links suffered from irreparable problems, leading to spontaneous loss of data (see [Sch01]). This inefficiency is implemented in the Monte Carlo simulations used at HERA-b by a detector map giving an FLT efficiency relative to the Second Level Trigger.

Second Level Trigger (SLT)

The Second Level Trigger is a software trigger running on a PC farm of 240 CPUs. It fully reconstructs two tracks based on the pretrigger seeds independantly of the FLT. The reconstruction includes a track following through the magnet and a vertexing step using information from the VDS. Track pairs with a vertex fit with $\chi^2 > 20$ are discarded.

Third Level Trigger (TLT)

It was originally foreseen to implement a Third Level Trigger step which uses a full reconstruction of the event to be able to trigger on additional tracks in an event, e.g. single leptons from semileptonic decays of mesons. During the data taking period of 2002/2003, this trigger was not used.

Fourth Level Trigger (4LT)

The Fourth Level Trigger consists of an online full reconstruction of events. Track segments are built in VDS and the tracker and matched to full tracks. Information from the muon system, ECAL and RICH are used for particle identification. Finally, tracks are assigned to primary and secondary vertices.

Chapter 2

Drell Yan Theory

2.1 The Drell Yan Process

The invariant mass spectrum of dileptons above 2 GeV observed at hadronic collisions consists of two parts: a series of sharp peaks and a continuum that drops with increasing mass. The peaks are produced by the charmonium and bottomium resonances (J/ψ , ψ' , Υ etc), while the continuum production of lepton pairs is known as the Drell Yan process ([Dre70]). In hadronic collisions, it has been the object of study for quite some time. Its basic reaction, the annihilation of quark and antiquark into a virtual photon and the subsequent decay into lepton and antilepton, $q\bar{q} \rightarrow \gamma^* \rightarrow l^+l^-$ is an ideal testing ground for perturbative QCD and a tool for probing the parton distributions of hadrons, especially mesons.

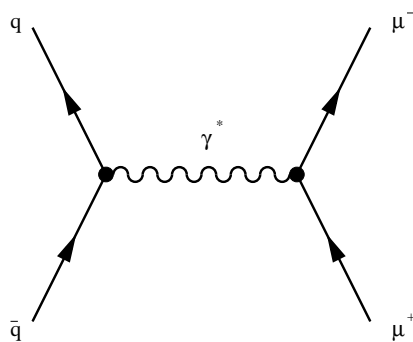


Figure 2.1: Feynman graph of the Drell Yan process at parton level.

2.2 Quark Parton Model and Perturbative QCD

The Drell Yan process is an example of a hard process at parton level. The parton model was ([Fey69]) used first in explaining the deep inelastic electron nucleon scattering. It describes a nucleon as consisting of constituents, the so called partons, which were later identified as quarks. The basic assumption of the model is that the typical time scale of an interaction between electron and parton is much less than that of the binding effects inside the nucleon.

Drell and Yan were the first to use the parton model to explain lepton pair production and to derive the Drell Yan cross section. Fig. 2.1 shows the Feynman graph of the reaction. The cross section of this process in leading order is

$$\hat{\sigma}_{q\bar{q}} = \frac{4\pi\alpha^2}{3\hat{s}} \cdot \frac{Q_q^2}{N}, \quad (2.1)$$

where \hat{s} corresponds to the center-of-mass energy available in the process ($\hat{s} = (p_1 + p_2)^2$), Q_q to the charge of the quark flavor and N to a color factor giving the probability that quark and antiquark have the same color charge ($N = 3$). \hat{s} is related to the total center-of-mass energy s by $\hat{s} = x_1 x_2 s$, where x_1 and x_2 are the momentum fraction of quark and antiquark inside the hadrons. This cross section corresponds to that of the creation of quarks in electron positron annihilation.

The differential cross section as a function of the dilepton mass is

$$\frac{d\hat{\sigma}_{q\bar{q}}}{dM_{ll}} = \frac{4\pi\alpha^2}{6M_{ll}} \cdot \frac{Q_q^2}{N} \cdot \delta(\hat{s} - M_{ll}^2), \quad (2.2)$$

where M_{ll} is the invariant mass of the lepton pair.

To find the cross section of the proton colliding with a nucleon of the target wires, it is necessary to include the parton density functions $f_{i/h}(x)$, which give the probability to find a parton i with momentum fraction x inside of a hadron h . This separation between density functions and cross section of the subprocess is the factorisation model ([Col89]), which is illustrated in Fig. 2.2. Convoluting the parton cross section with the density functions then yields after summing, over all possible flavors i and integrating over the momentum fractions x_1 and x_2 of the two quarks then yields:

$$\sigma_{h_1 h_2 \rightarrow l^+ l^-} = \sum_q \int dx_1 dx_2 f_{q/h_1}(x_1) f_{\bar{q}/h_2}(x_2) \hat{\sigma}_{q\bar{q} \rightarrow l^+ l^-} \quad (2.3)$$

The corresponding differential cross section again as a function of the dilepton mass M_{ll} is given by:

$$M_{ll}^3 \cdot \frac{d\sigma}{dM_{ll}} = \frac{1}{2N} \cdot \frac{4\pi\alpha^2}{3} \cdot \tau \cdot \mathcal{F}(\tau), \quad (2.4)$$

where

$$\mathcal{F}(\tau) = \int_0^1 dx_1 dx_2 \delta(x_1 x_2 - \tau) \left(\sum_q Q_q^2 (f_{q/h_1}(x_1) f_{\bar{q}/h_2}(x_2) + (q \leftrightarrow \bar{q})) \right). \quad (2.5)$$

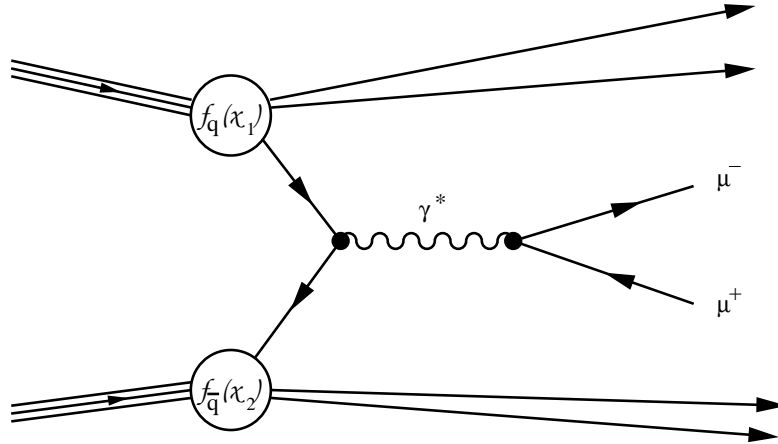
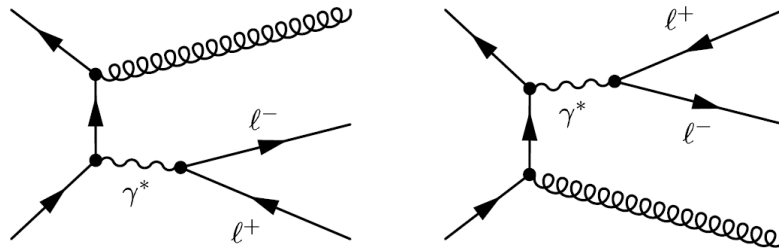


Figure 2.2: Factorisation model of the Drell Yan Process. Quark and antiquark out of two incident hadrons interact and annihilate, the hadron remnants disappear along the beam axis.

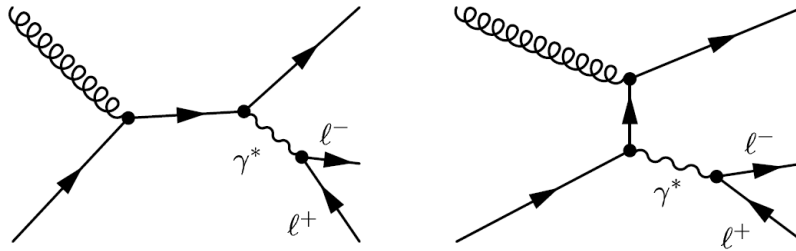
In leading order the Drell Yan differential cross section Eq. (2.4) only depends on the dimensionless variable $\tau = M_U^2/s$, not on M_U or s individually. This scaling behavior makes it possible to compare results measured at different center-of-mass energies.

However, contributions from higher order processes are not negligible. The Feynman graphs of the most important processes of order $\mathcal{O}(\alpha_s)$ and $\mathcal{O}(\alpha_s^2)$ are given in Fig. 2.3. These include initial state radiation of gluons, a process alike to Compton scattering in QED and gluon exchange between the incident quarks.

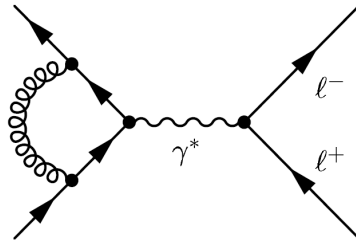
At energies attainable by current fixed target and collider experiments, these next to leading order corrections are large, up to 50% of the total cross section in the mass range covered by this thesis, 4 to 9 GeV. Fig. 2.4 shows a calculation of the differential Drell Yan cross section in the mass range of 8 to 70 GeV in $\mathcal{O}(\alpha_s^0)$, $\mathcal{O}(\alpha_s^1)$ and $\mathcal{O}(\alpha_s^2)$. The difference is clearly visible.



(a) Gluon Bremsstrahlung



(b) Compton like QCD processes



(c) Vertex correction

Figure 2.3: QCD corrections in leading (a, b) and next to leading order (c) to the Drell Yan Process. Figures from [Gra01].

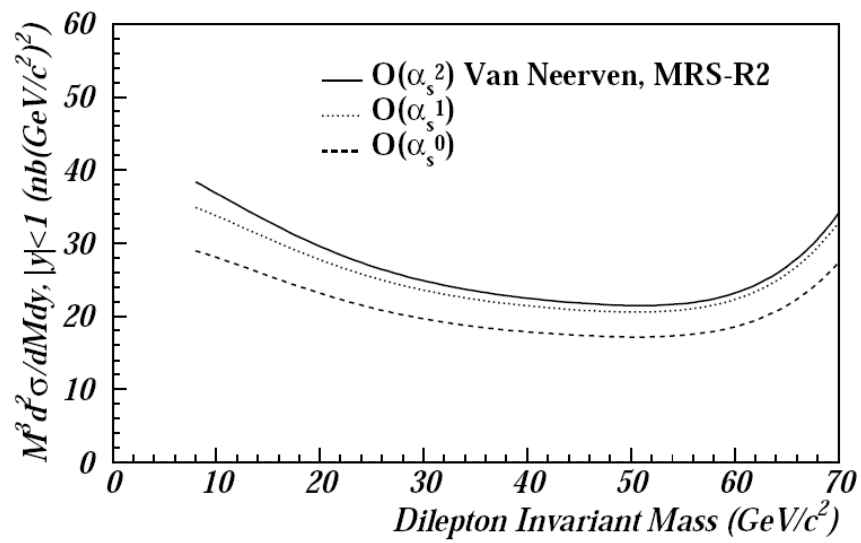


Figure 2.4: Theoretical calculation of the differential Drell Yan cross section including corrections of $\mathcal{O}(\alpha_s)$ and $\mathcal{O}(\alpha_s^2)$. Calculations by [Nee92].

2.3 Angular Distributions

The large correction factors from higher order contributions discussed in Sec. 2.2 diminish the use of the integrated Drell Yan cross sections as tests of the parton model. The angular distribution of the lepton pair is more useful for this.

In the parton model with massless quarks, the lepton pair is produced by the decay of a transversely polarized virtual photon. The differential cross section is then expected to be:

$$\frac{d\sigma}{d\Omega} \propto 1 + \cos^2 \theta, \quad (2.6)$$

where θ is the polar angle of the positive lepton in the rest frame of the virtual photon. There are several possible choices for a coordinate system in which the virtual photon is at rest. In this thesis, the so called Collins Soper frame ([Col77]) will be used.

In the Collins Soper frame the virtual photon is at rest. It's $x-z$ plane is spanned

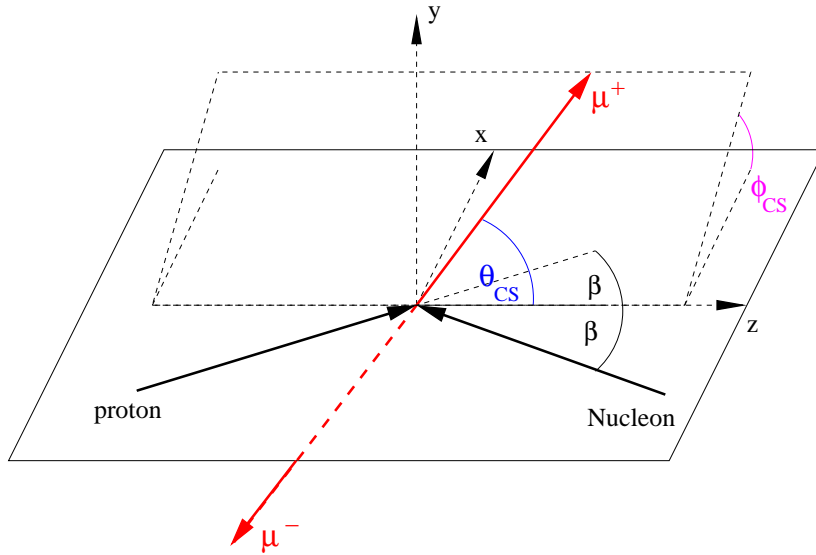


Figure 2.5: Illustration of the Collins Soper reference frame and of the angles θ_{CS} and ϕ_{CS} .

by the momentum vectors of proton and nucleon, which are not collinear if the virtual photon has a nonzero transverse momentum. The z axis is defined to be the bisector of the angle between incoming nucleon and inverse incoming proton. The definition of the CS reference frame is illustrated in Fig. 2.5. The angle ϕ_{CS} is defined as the angle between the xz plane and the plane spanned by the positive muon and the z axis, the angle θ_{CS} as the angle between positive muon and z axis.

The inclusion of the higher order processes given in the last section leads to a

cross section that not only depends on the polar, but also the azimuthal angle:

$$\frac{1}{\sigma} \frac{d\sigma}{d\Omega} = \left[\frac{3}{4\pi} \frac{1}{\lambda + 3} \right] \left(1 + \lambda \cos^2 \theta + \mu \sin 2\theta \cos \phi + \frac{\nu}{2} \sin^2 \theta \cos 2\phi \right) \quad (2.7)$$

Here, ϕ is the azimuthal angle of the positive lepton. The three coefficients λ , μ and ν are structure functions. While they are independent of the angles, they may depend on other kinematic variables, such as the transverse momentum or the mass of the virtual photon. The parameter μ is only relevant at energies where contributions by the exchange of a Z boson instead of a photon are significant. The other two coefficients are correlated via the Lam Tung relation ([Lam80]):

$$1 - \lambda - 2\nu = 0 \quad (2.8)$$

This relation is the analogon to the Callan Gross relation ([Cal69]), which relates the structure functions $F_1(x)$ and $F_2(x)$ in deep inelastic scattering. Unlike the Callan Gross relation though, the Lam Tung relation is unchanged by QCD corrections of first order. Even after the inclusion of higher order corrections it is still approximately valid, but $1 - \lambda - 2\nu$ is predicted to be slightly positive.

2.4 Violation of the Lam Tung Relation

Two experiments have performed measurements of the angular dependance of the Drell Yan cross section in collisions of pion beams with fixed targets. These were NA10 ([And84]), a fixed target experiment located at CERN and E615 ([Bii86]), a Fermilab experiment. Both experiments reported a violation of the Lam Tung relation in $\pi - N$ collisions at large transverse momenta of the virtual photon. The results of NA10 are given in Fig. 2.6, those of E615 in 2.7. Both measurements clearly show an increasing value of ν at large transverse momenta, while λ stays constant. This leads to a dependancy of $1 - \lambda - 2\nu$ on p_t which is a violation of the Lam Tung relation. Interestingly both experiments give a negative value for $1 - \lambda - 2\nu$, the opposite of the prediction of higher order QCD. The measurements of μ do not agree. While NA10 measured no dependance of μ on the transverse momentum, E615 does see a correlation; at higher p_t μ is measured to be positive and large, up to 0.5.

More recently, the Fermilab experiment E866 ([Web02]) measured the angular distributions of Drell Yan using an 800 GeV proton beam at a fixed target. The results published in [Zhu06] show no violation of the Lam Tung relation and no dependance of ν on the transverse momentum in $p - N$ collisions. Fig. 2.8 shows the three coefficients and the value $2\nu - (1 - \lambda)$ as a function of the transverse momentum of the virtual photon for the three experiments listed above. None of the coefficients show a dependance on the transverse momentum in $p - N$ data.

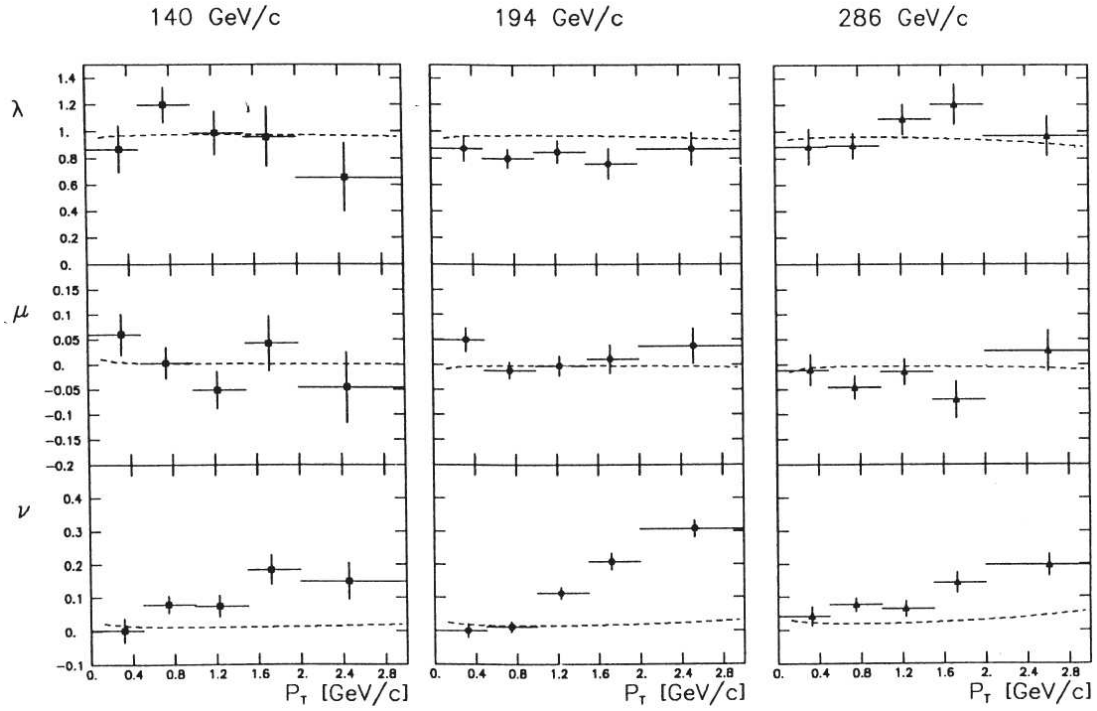


Figure 2.6: Measurement of λ , μ and ν as a function of p_t of the muon pair and for three different beam energies at NA10 ([Gua88]). The dashed lines show the QCD predictions including terms of $\mathcal{O}(\alpha_s)$. The discrepancy for ν between measurement and prediction at large p_t is distinctive.

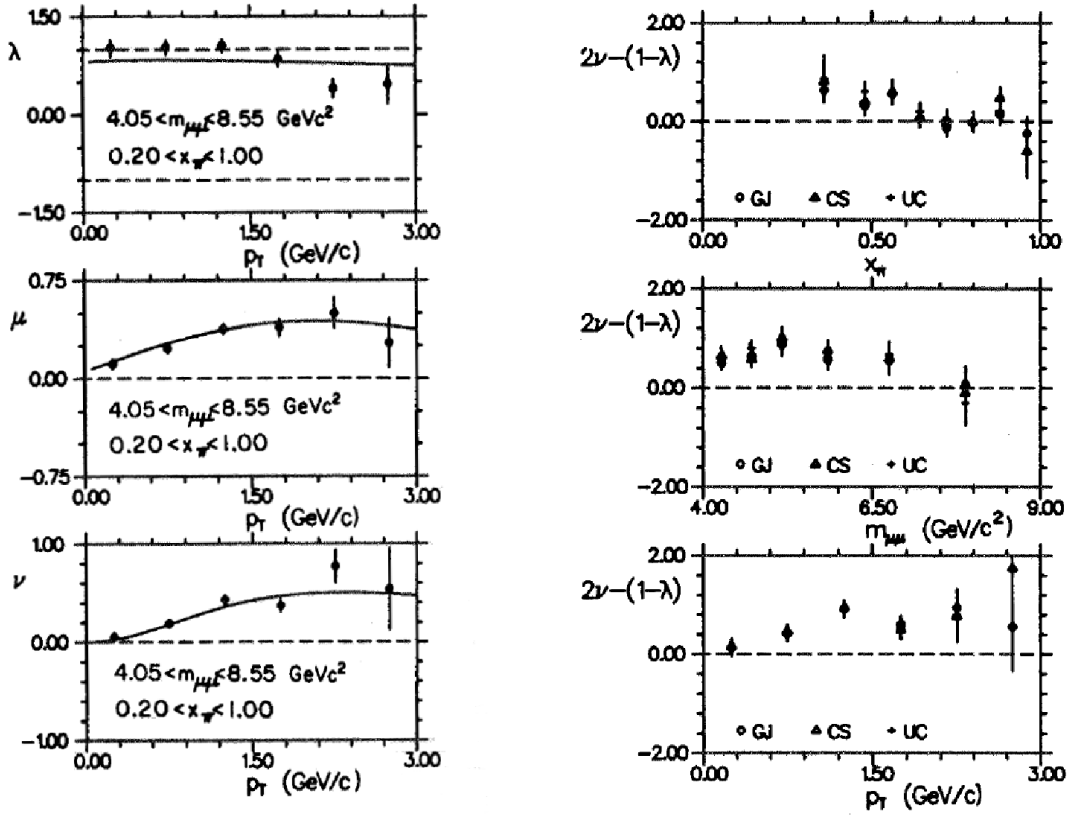


Figure 2.7: Left plots: Measurement of λ , μ and ν as a function of p_t of the muon pair at E615 ([Con89]). Right plots: from the measured values of λ and ν , the Lam Tung relation is plotted as a function of the momentum fraction of the parton in the incident pion x_π , mass and p_t of the muon pair in three reference frames (Gottfried Jackson, Collins Soper and u channel).

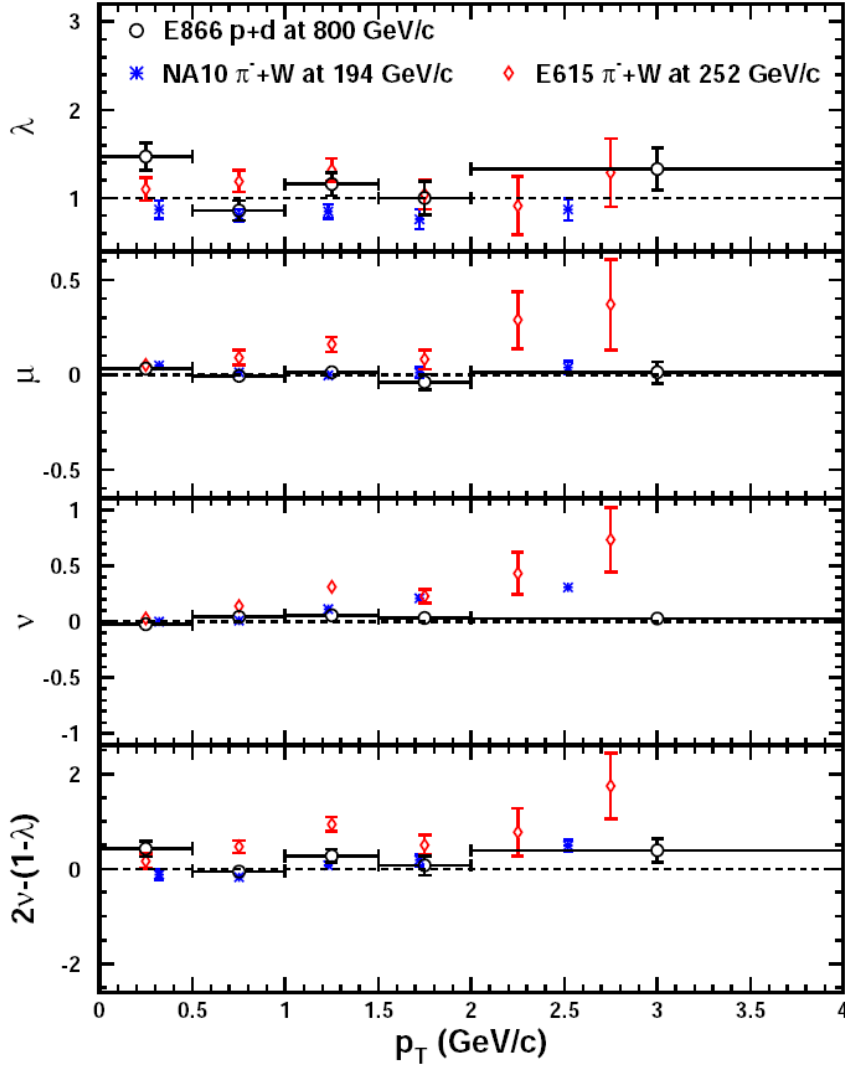


Figure 2.8: Measurement of λ , μ and ν as a function of p_\perp of the virtual photon at E866, compared to the measurements of NA10 and E615. While the latter show a deviation of the value $2\nu - (1 - \lambda)$ from zero, the measurement from E866 ([Zhu06]) is compatible with zero.

Several theoretical models beyond conventional perturbative QCD have been suggested to explain the violation seen in pion–nucleon collisions.

2.4.1 Higher Twist Contributions

Higher Twist Contributions to the Drell Yan cross section are caused by interactions of the annihilating quarks with spectator quarks prior to the collision by gluon exchange. In [Bra94] this model is applied to the Drell Yan process. It is found that the angular coefficients λ , μ and ν are still defined as in Eq. (2.7) but are explicit functions of the kinematic variables $x_L = 2p_t/\sqrt{s}$, p_t^2/M^2 and M^2/s . The prediction of the model strongly depends on the parton density function of the incident pion, as can be seen in Fig. 2.9, where the predictions for different parton density functions are compared with the data measured by E615.

Especially at high transverse momenta of the virtual photon, the model cannot

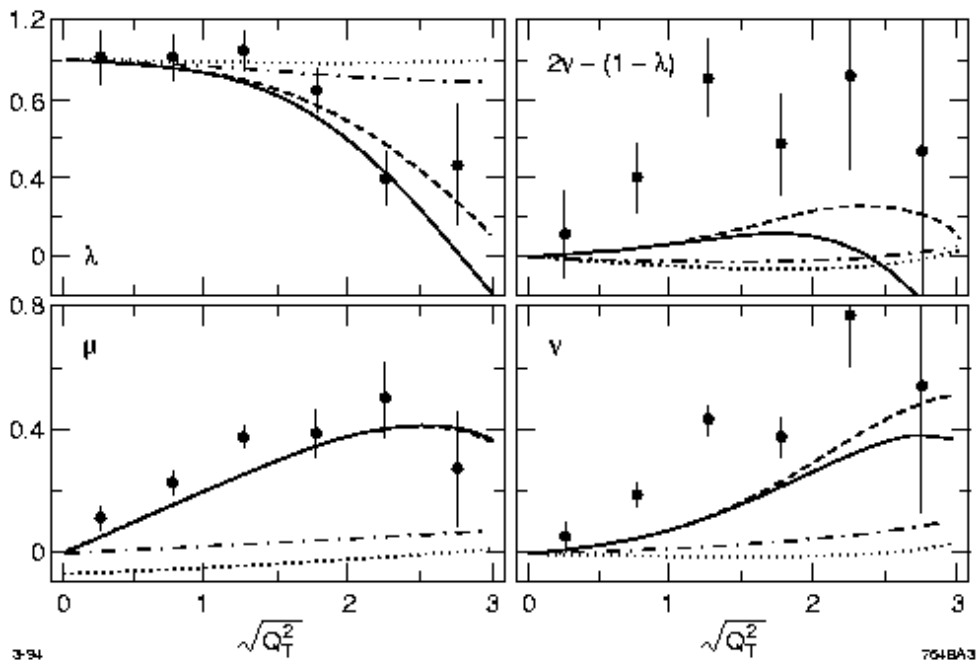


Figure 2.9: Comparison of the predictions of the Higher Twist model to data measured by E615 ([Bra94]) as a function of p_t of the virtual photon. The four lines represent calculations using different parton density functions of the incident pion. The model fails to reproduce the violation of the Lam Tung relation measured by E615, especially at high p_t .

reproduce the violation of the Lam Tung relation seen at $\pi - N$ collisions. While the dependance of λ and μ on p_t is simulated, the values of ν disagree.

2.4.2 Spin and p_t Correlations of Quarks

The underlying assumption of the Lam Tung relation is that the incident quarks are not polarized if the corresponding hadrons are unpolarized. Two separate approaches suggest that this is not necessarily the case. The first approach published in [Bra93] suggests that non perturbative vacuum fluctuations induce correlations between the partons of the colliding hadrons via initial state interactions. It assumes a general two particle spin density matrix for the quark antiquark pair before annihilation which contains a correlation term that connects the spins of the two interacting quarks. It was shown that for a non zero correlation coefficient κ , the experimental observation of the violation of the Lam Tung relation can be explained. Fig. 2.10 shows a calculation of the model prediction for the dependance of the structure functions λ , μ and ν on the transverse momentum of the virtual photon, once for a correlation coefficient $\kappa = 0$ and once with a non zero value of κ fitted to the data.

The second approach ([Boe99]) suggests time reversal (T) odd distribution functions, which introduce non trivial spin and p_t correlations between the quarks even in unpolarized hadrons. This again leads to a non zero value of the correlation coefficient κ . A calculation of the p_t dependance of the value of ν is shown in Fig. 2.11. In [Boe05] it is suggested that a measurement using a different type of beam than the pions used at E615 and NA10 would help to distinguish between the two approaches, as while the vacuum fluctuations are independant of the flavor of the quarks, the distribution functions used in [Boe99] may well depend on the flavor. For this, HERA-b and the proton beam of HERA was thought to be an ideal testing ground.

The sensitivity of HERA-b to the Drell Yan process was investigated in [Gra01], which estimated that 25,000 events would be needed to measure the angular distributions. This would correspond to a year of data taking with a good detector performance. First extrapolations of the yield of Drell Yan events from the number of detected J/ψ show that the dataset of 2002/2003 only contains roughly 1,500 Drell Yan produced dimuons and the same number of events with dielectrons. Nevertheless an analysis searching for Drell Yan events was performed, as the HERA-b detector is uniquely sensitive in the negative x_F range and can extend existing measurements into this region.

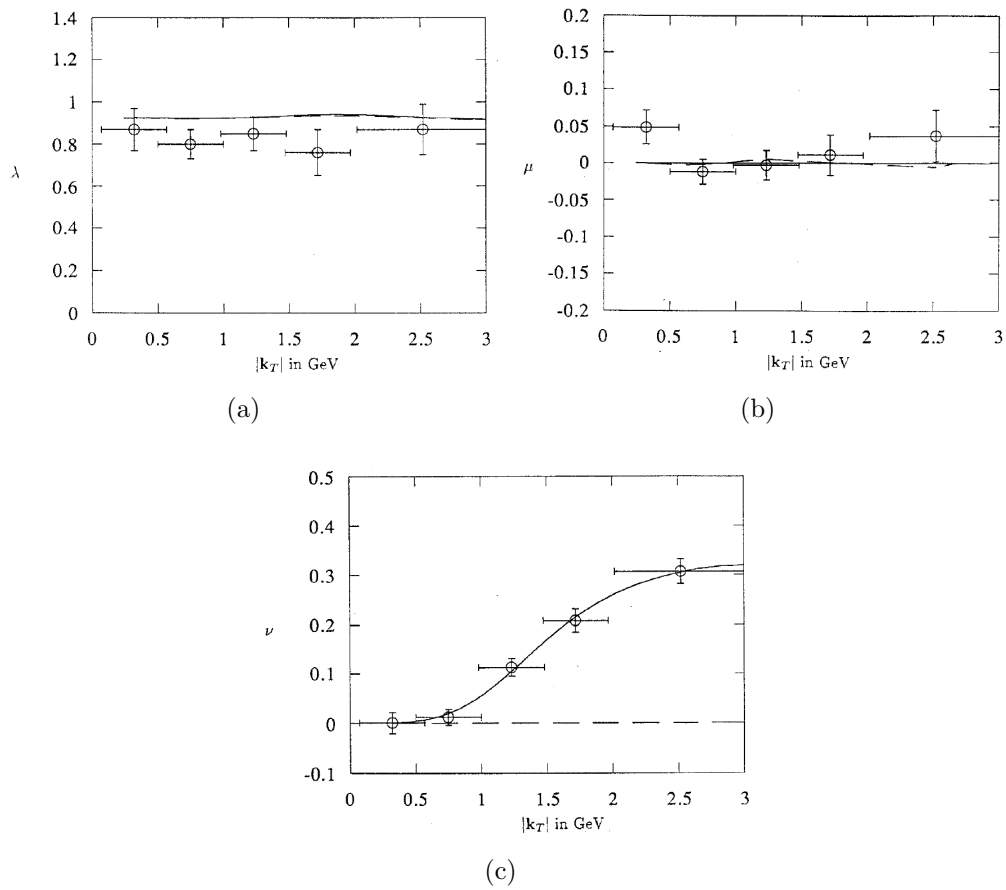


Figure 2.10: The dependance of the three structure functions λ , μ and ν on the transverse momentum of the virtual photon ([Bra93]). The dashed lines correspond to the prediction of the parton model for $\kappa = 0$ and no quark polarization, the full lines to the prediction with a non zero value of κ . The data points are from E615.

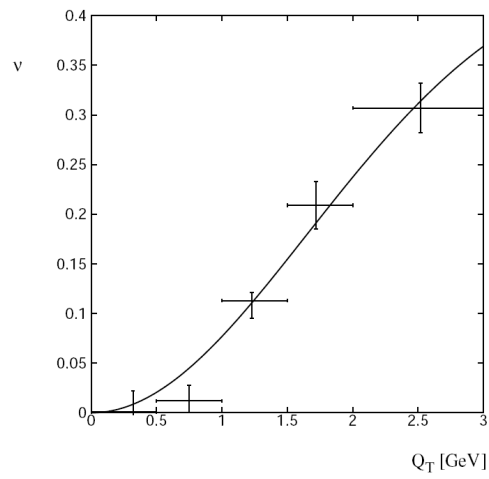


Figure 2.11: Dependence of ν on the transverse momentum of the virtual photon. Data from E615 and a calculation using a non zero value of κ ([Boe99]) are shown.

Chapter 3

Data Selection and Background Subtraction

The data used in this analysis has been taken at the HERA-b detector using the dilepton trigger during the period from November 2002 to February 2003. After this time, the accelerator was shut down for upgrades and repairs.

To extract the Drell Yan signal from the data, selection criteria have to be applied. Choosing these cuts requires a good knowledge of signal and background distributions. While the Drell Yan signal is described by a Monte Carlo simulation, no such simulation exists for the background. Monte Carlo studies ([Egb02]) have shown that while it is possible to simulate the processes involved, the computer time needed to generate a sufficient number of events is prohibitively large due to the small phase space involved. To simulate one second of data taking with full event reconstruction, a Pentium III processor would need about ten years of CPU time at an interaction rate of 10 MHz. A dedicated Monte Carlo simulation concentrating on pions and kaons decaying in flight can reduce the time needed by a factor of four to five, which is still not enough. For this reason, other methods of background description have to be found.

The data runs used for this analysis have been selected by the charmonium analysis group for acceptable data quality ([Cha03]). In total, they consist of roughly 150 million events.

This analysis is based on the preselection of the dimuon group, which uses a different analysis software. As a first step, the data available in the ARTE¹ dst format was converted into root files for use in the BEE² analysis framework. The BEE software has the advantage of smaller data files and useful routines, e.g. to find vertices.

During this conversion the data was reduced by asking for a minimum of two

¹The Event Reconstruction and Analysis Tool ARTE is the main framework used to analyse data and Monte Carlo events ([Alb95]).

²The analysis framework BEE discards detector hit information contained in the ARTE files and only keeps reconstructed tracks for faster processing ([Gle01])

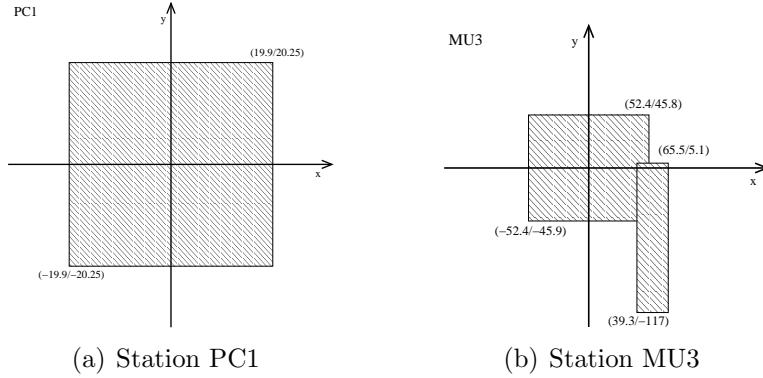


Figure 3.1: Fiducial cuts in the stations PC1 (a) and MU3 (b). Tracks crossing the hatched regions are removed. The coordinates of the corners of the removed areas are given in cm.

tracks triggered by the Second Level Trigger (SLT) with at least five hits in the muon chambers and a muon likelihood of greater than 0.01 per event. Events without at least two muons are not relevant for the analysis, neither are muon track candidates with extremely low muon likelihood or too few hits in a muon chamber.

Three fiducial cuts proposed in [Hus05] are applied to real and Monte Carlo data to remove detector areas which are not described correctly by the simulation. One cut is applied at the z position of station PC1 around the Inner Tracker area, the other two at the z position of station MU3. They are shown in Fig. 3.1. The two cuts around the beampipe area remove tracks in the transition region between inner and outer tracker, which poses problems for the Monte Carlo simulation. The second cut in station MU3 removes tracks in muon chamber 99, which also shows inefficiencies which are not present in the simulation.

After clone removal³ and a cut on the minimum number of tracker hits per muon trigger track of four hits, the dimuon sample consists of 3.1 million events. As the muon trigger has no requirements concerning the muon charge, this sample contains muon pairs with opposite and with equal charge, namely 1.8 million unlikesign, 775,000 positive likesign and 605,000 negative likesign muon pairs.

Since the magnetic field inside the detector is oriented upwards, positive particles are deflected to the right (seen from the interaction point) while negative particles are deflected to the left. Due to their track configuration, unlikesign muon pairs travelling through the detector with the negative muon on the left and the positive on the right are called “outbending”, as the magnet deflects both muons away from each other. Likewise, $\mu^+\mu^-$ pairs with the opposite charge dis-

³If a particle passing the silicon detector undergoes a hard scattering, it is possible that the reconstruction algorithm assigns two tracks to this particle. The second track is called clone and is flagged during reconstruction ([Kis99])

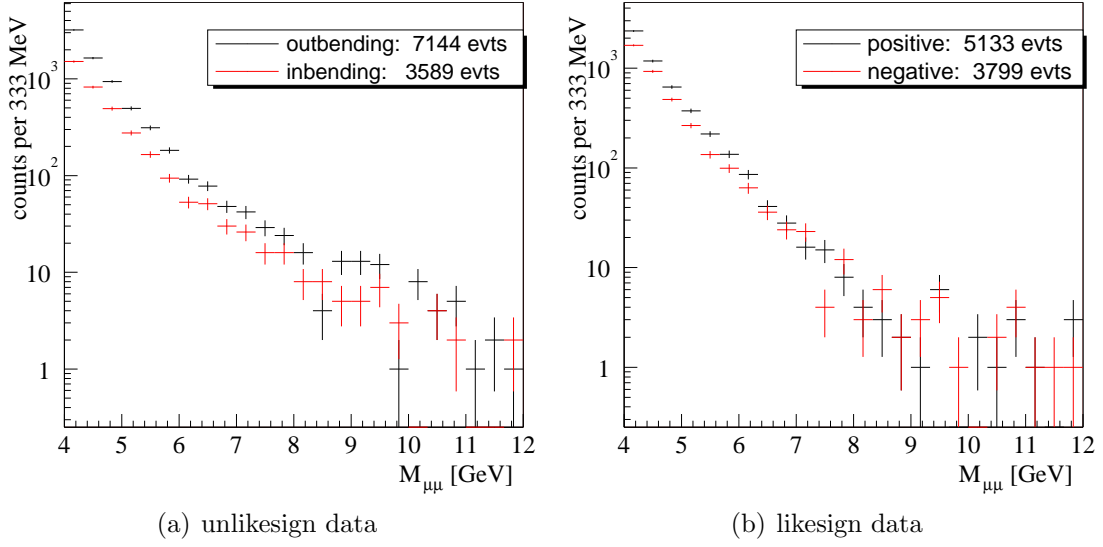


Figure 3.2: *Invariant mass of muon pair data after preselection:*
 (a) *unlikesign muon pairs, divided into inbending and outbending,*
 (b) *likesign muon pairs, divided into positive and negative pairs.*

tribution are called “inbending”.

The distribution of the dimuon mass is shown in Fig. 3.2, separated into the four categories unlikesign out-/inbending and positive and negative likesign muon pairs in the mass range above $M_{\mu\mu} = 4\text{GeV}$. As one can see the number of events in this mass range is much lower than the total number of muon pairs, as most of them have a lower reconstructed invariant mass.

3.1 Event Selection

The background in the dimuon channel has two contributions:

- Combinatorial background consisting of pairings of unrelated particles. These are muons from pions and kaons decaying in flight, prompt muons from the vertex and other particles misidentified as muons (punch through, high energy protons reaching the muon system), and
- muon pairs from decays of charmonium and epsilon.

While the latter can be eliminated by cuts on the invariant mass of the muon pair, the first are spread over the whole mass spectrum, making their rejection

more difficult. Several cuts on kinematic variables have to be applied to reduce this background.

The main difference between muon pairs produced by the Drell Yan process and those from combinatorics is that the Drell Yan muons both come from the primary vertex⁴, while muon tracks from decays in flight do not necessarily point back to the primary vertex. This leads to different dependences of signal and background on the distance of closest approach between the two muons, the distance of muon to primary vertex and the reduced χ^2 of the track fit to hits in the detector. These variables are therefore used to improve the ratio of signal to background.

The limited number of events provided by HERA-b makes it impractical to choose very hard cut values which would result in high purity but low efficiency. Softer cuts result in a larger data sample with a lower signal to background ratio. The background still remaining after the selection process distorts the angular and kinematic distributions of the Drell Yan process. To remove this distortion, a method of background subtraction in each of the plotted variables is necessary. Both the cut optimization and the background subtraction require a simulation of the combinatorial background. Previous analyses have used the method of event mixing to generate a combinatorial background sample ([Abt06]).

3.2 Event Mixing to Simulate Background

Event mixing describes a method frequently used to simulate combinatorial background. Combinatorial background consists of random combinations of unrelated tracks. As tracks from different events are by definition unrelated, an obvious solution is to mix tracks (in this case muons) from different events into a single one. The result is then a purely combinatorial sample of muon pairs.

As shown in Fig. 3.3, the muons generated by a Drell Yan process carry a significant part of the total momentum of 920 GeV in an event. Unfortunately, event mixing does not conserve momentum, due to the random combination of unrelated tracks from different events. This introduces a bias into kinematic distributions generated by this sample. Fig. 3.4 show comparisons between distributions of likesign and event mixed data in different kinematic variables. Since likesign muon pairs also consist of combinatorial background only (see also Sec. 3.3), the distributions from event mixing must reproduce those of likesign data to be usable as a background simulation. As one can see, every distribution shows differences between likesign distributions and those of mixed events data.

Several methods have been applied to remove these discrepancies. [Hul02] suggests to apply weights after the event mixing procedure to match the generated

⁴The primary vertex is the location of the main interaction between incident proton and the target wire, reconstructed from all tracks of an event.

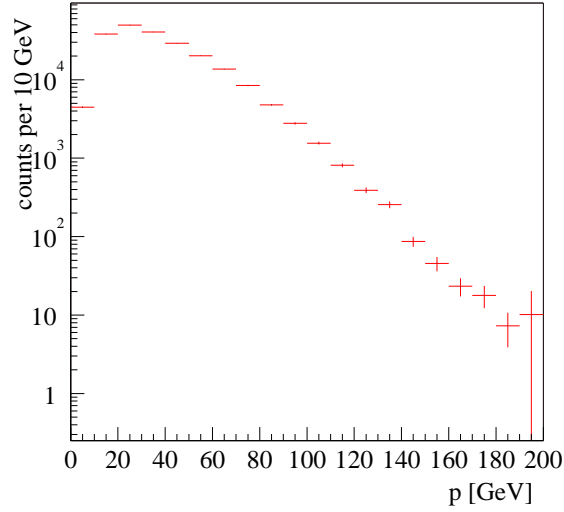


Figure 3.3: *Reconstructed momentum distribution of muons generated by the Drell Yan process in simulated events. The muons carry up to 20% of the total momentum of 920 GeV of an event.*

distributions to the expected ones. While this technique works in matching the event mixed sample to likesign data in one variable, it is not possible to match all distributions simultaneously.

A second possibility is to select mixed muon tracks according to their momentum to restore momentum conservation approximately and only match those with compatible momenta. However, this method also fails to reproduce the likesign data distributions. If one chooses loose bounds on the muons, the resulting distributions still do not match those of likesign data. If the bounds are too strict, no real mixing between events occurs as only the muon pair from the original event fulfills the preselection criteria.

Ultimately, the bias introduced by the nonconservation of momentum intrinsic to event mixing leaves this method unusable in this analysis, where a background subtraction in several kinematic distributions at the same time is needed.

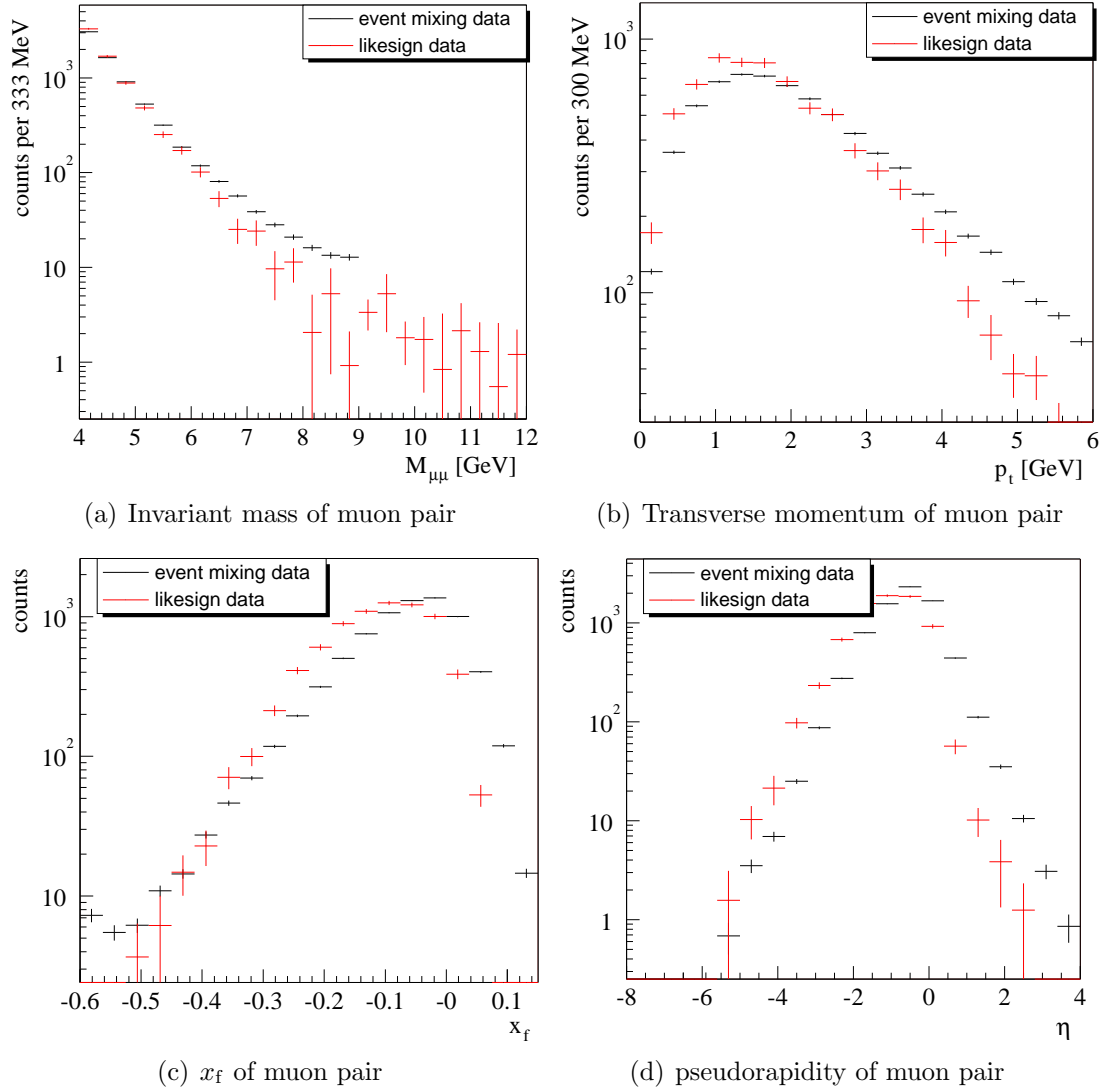


Figure 3.4: Comparison of distributions depending on several kinematic variables between likesign muon pair data and muon pairs generated by an event mixing procedure.

3.3 Likesign Data as Background

Monte Carlo studies ([Ric03]) have shown that likesign combinations of muons can be used as a simulation of the combinatorical background. The background muons contributing to the combinatorical background are mainly generated by decays in flight of pions and kaons with both charges in equal probability with a uniform distribution in ϕ . Thus, the four possible charge combinations $\mu^+\mu^-$, $\mu^-\mu^+$, $\mu^+\mu^+$ and $\mu^-\mu^-$ are expected to have the same probability to occur at production.

Since there is no decay producing two muons of the same charge, both data sets of likesign muon pairs consist entirely of combinatorical background:

$$N_{\text{total}}^{++} = N_{\text{bg}}^{++} \quad \text{and} \quad N_{\text{total}}^{--} = N_{\text{bg}}^{--}$$

On the other hand, the unlikesign muon pair sets contain background and signal events even after the optimization of the selection criteria presented in Sec. 3.5, which are inseparable by further cuts:

$$N_{\text{total}}^{+-} = N_{\text{DY}}^{+-} + N_{\text{bg}}^{+-} \quad \text{and} \quad N_{\text{total}}^{-+} = N_{\text{DY}}^{-+} + N_{\text{bg}}^{-+}$$

Subtracting the likesign datasets from the unlikesign after correction for acceptance differences results in a pure signal sample.

3.3.1 Acceptance Differences between Likesign and Unlikesign Data

The probability to detect a muon pair strongly depends on the charges, the positions of the muons in the magnet and their momentum in the detector. These quantities determine whether a track crosses the active detector volume, disappears in the beampipe or inner tracker region or leaves the detector at the outside. Fig. 3.5 schematically shows the effect of the insensitive region around the beampipe for the four different charge combinations in the detector. Inbending muon pairs travelling close to the beampipe before the magnet are unlikely to be triggered, as the magnet forces the tracks to cross the insensitive inner detector region behind it. On the other hand, outbending muon pair tracks are unlikely to be found close to the inner tracker at the far end of the detector because these tracks pass through the dead inner detector region between the magnet and the last stations and are not detected. Since the track density drops off with increasing distance from the beampipe before the magnet, the total sample of inbending muon track pairs is lower than that of outbending ones.

Likewise, muons from positive likesign pairs can be detected closer to the beampipe if they are on the right side of the detector as seen from the interaction point, while muons from negative likesign pairs tend to be closer on the left side of the

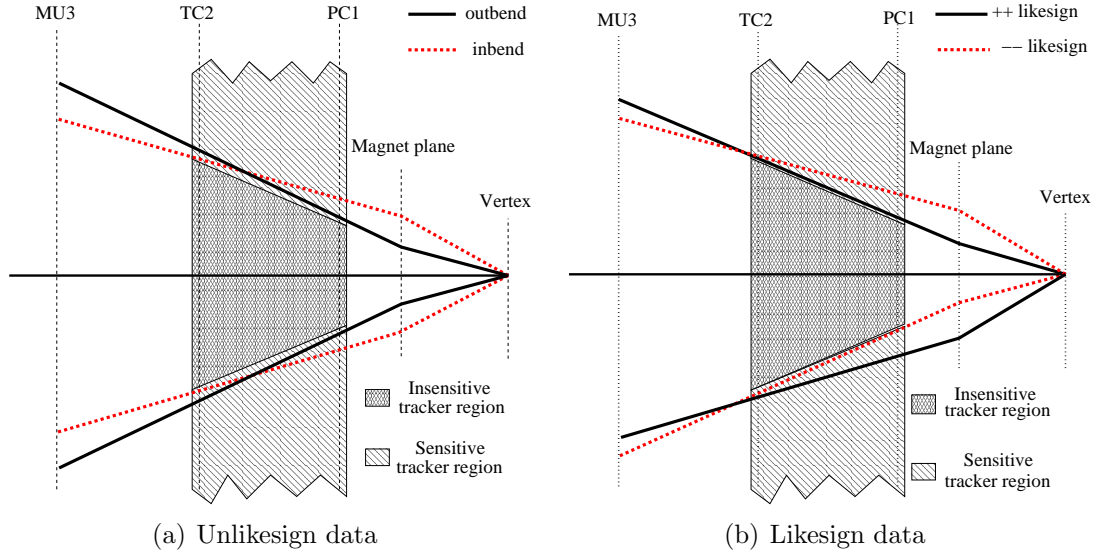


Figure 3.5: Schematic representation of the difference in acceptances between unlike- and likesign muon pairs. The tracks closest to the beam axis that will still pass through the active detector region and thus be accepted by the trigger are shown. Positive particles are deflected to the right as seen from above by the magnet, negative particles to the left. Fig. (a) shows inbending and outbending unlikesign track pairs, Fig. (b) positive and negative likesign track pairs. The different angles of the track pairs at the vertex illustrate the differences in acceptance between the four charge combinations.

detector. This asymmetrical distribution of tracks can also be seen in Fig. 3.6, where the x position of tracks in the magnet focal plane⁵ is plotted.

This only applies to tracks passing through the detector to the left or right of the insensitive region, not above or below, since the magnet only deflects tracks in the horizontal plane. As one can see in Fig. 3.7, which shows the positions of all tracks in station PC1, the majority of tracks are passing to the left or right of the insensitive central detector region. These differences in acceptance have to be accounted for before likesign data can be used to optimize the cuts or to subtract the background from the data distributions.

The final number of Drell Yan events can then be calculated by

$$N_{\text{DY}} = N_{\text{total}}^{+-} + N_{\text{total}}^{-+} - C_1 N_{\text{bg}}^{++} - C_2 N_{\text{bg}}^{--} \quad \text{with} \quad C_{1,2} = \frac{\text{unlikesign acceptance}}{\text{likesign acceptance}}$$

⁵The bending of tracks by the magnet can be simulated by two straight tracks connected by a kink at a vertical plane in the magnet. This plane is called the focal plane.

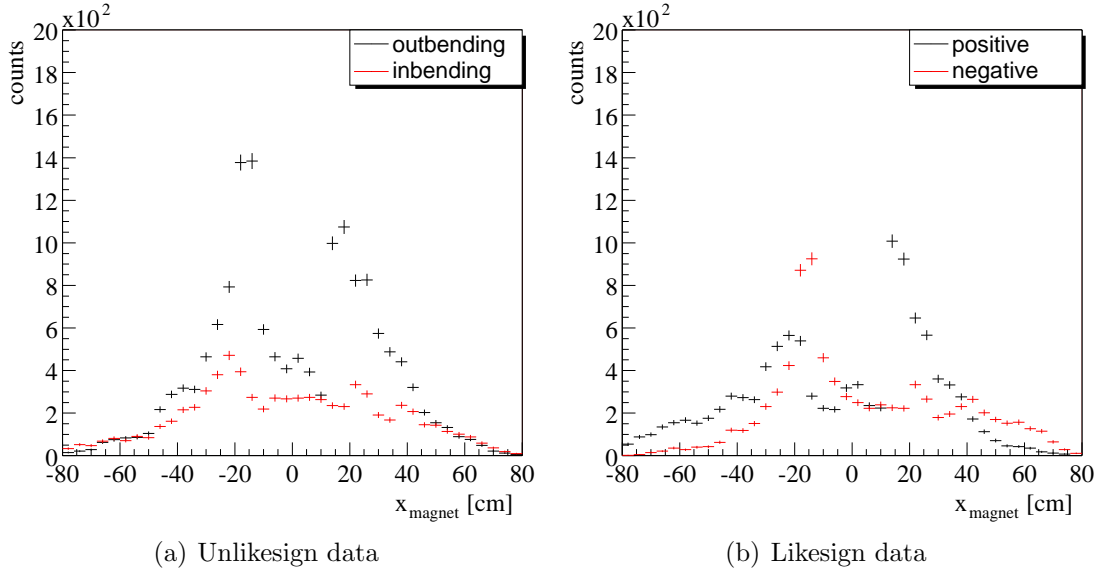


Figure 3.6: x position of muon tracks in the focal plane of the magnet after fiducial cuts. (a) shows outbending and positive likesign data, (b) inbending and negative likesign data. The difference between in- and outbending unlikesign and between positive and negative likesign distributions is caused by the dependance of the acceptance on the muon charge combinations.

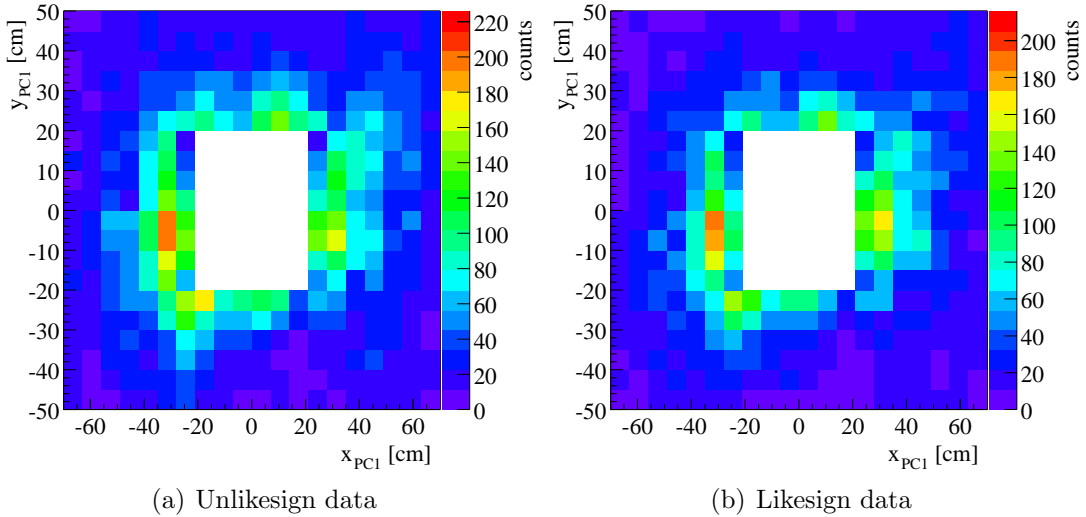


Figure 3.7: x vs. y position of muon tracks in station PC1 after fiducial cuts. (a) shows all unlikesign, (b) all likesign data. The majority of tracks pass the station to the left and right of the insensitive inner detector region within $-20 \text{ cm} < y < 20 \text{ cm}$.

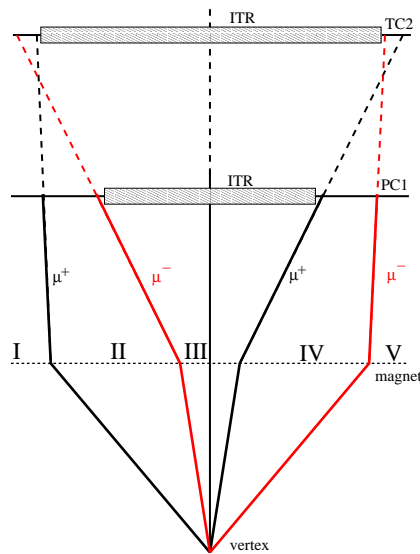


Figure 3.8: The figure shows tracks which touch the insensitive inner tracking regions on their path through the detector. These boundary tracks define five regions (I-V) at the central magnet position which separate accepted from not accepted tracks for the different charge combinations. Muons from inbending ($\mu^+\mu^-$) muon pairs passing through regions II, III or IV are not detected, outbending ($\mu^-\mu^+$) muon pairs are only lost if one or both muons pass region III. Likewise positive likesign muon pairs in regions II and III and negative likesign muon pairs in regions III and IV are not seen.

It is necessary to calculate the total number of Drell Yan events using both inbending and outbending, positive and negative likesign datasets at the same time. As Fig. 3.8 and Tab. 3.1 show, each dataset consists of muons found in different regions of the detector. Every charge combination dataset contains tracks passing through regions I and V. Tracks in region II are only detected if the muon pair is either outbending or negative likesign, tracks in region IV only in the outbending or positive likesign datasets. Muon pairs with tracks passing through region III are not detected regardless of muon charges. While it is possible to correct acceptances downwards using weights, there is no way to restore the data lost in an insensitive region. A negative likesign dataset reweighted to outbending acceptance will thus not correctly describe the outbending combinatorial background. The reason for this is that muon pairs travelling through region IV are present in the outbending unlikesign dataset but not the negative likesign. If both unlikesign and likesign datasets are added though, the numbers of regions containing data match. Regions I and V are seen in both unlikesign datasets, regions II and IV once each, the same as for both likesign datasets.

Unfortunately, the missing central detector region is not the only detector inefficiency present. The First Level Trigger (FLT) shows a very strong dependence on muon track position and has regions with very low efficiency. Fig. 3.9 shows the average FLT efficiency in the $x - y$ plane, plotted at the position of trigger station TC2. Each of the areas with low efficiency contributes further to the difference in statistics seen by the four charge combinations. While it would be possible to reweight both positive and negative likesign datasets to the acceptance of inbending unlikesign data if the acceptance difference was caused only by the missing Inner Tracker, the overlapping areas with little or no data available in one or more datasets caused by the FLT inefficiencies only allow the reweighting to succeed if all datasets are used.

Dataset	Detector Regions				
	I	II	III	IV	V
Outbending $\mu^- \mu^+$	✓	✓	-	✓	✓
Inbending $\mu^+ \mu^-$	✓	-	-	-	✓
Positive like $\mu^+ \mu^+$	✓	-	-	✓	✓
Negative like $\mu^- \mu^-$	✓	✓	-	-	✓
Unlikesign total	2 · ✓	1 · ✓	-	1 · ✓	2 · ✓
Likesign total	2 · ✓	1 · ✓	-	1 · ✓	2 · ✓

Table 3.1: *Detector regions at the magnet as defined in Fig. 3.8 which contain data, separate for the four muon charge combinations. Also, the data in the combined unlikesign and likesign dataset is shown.*

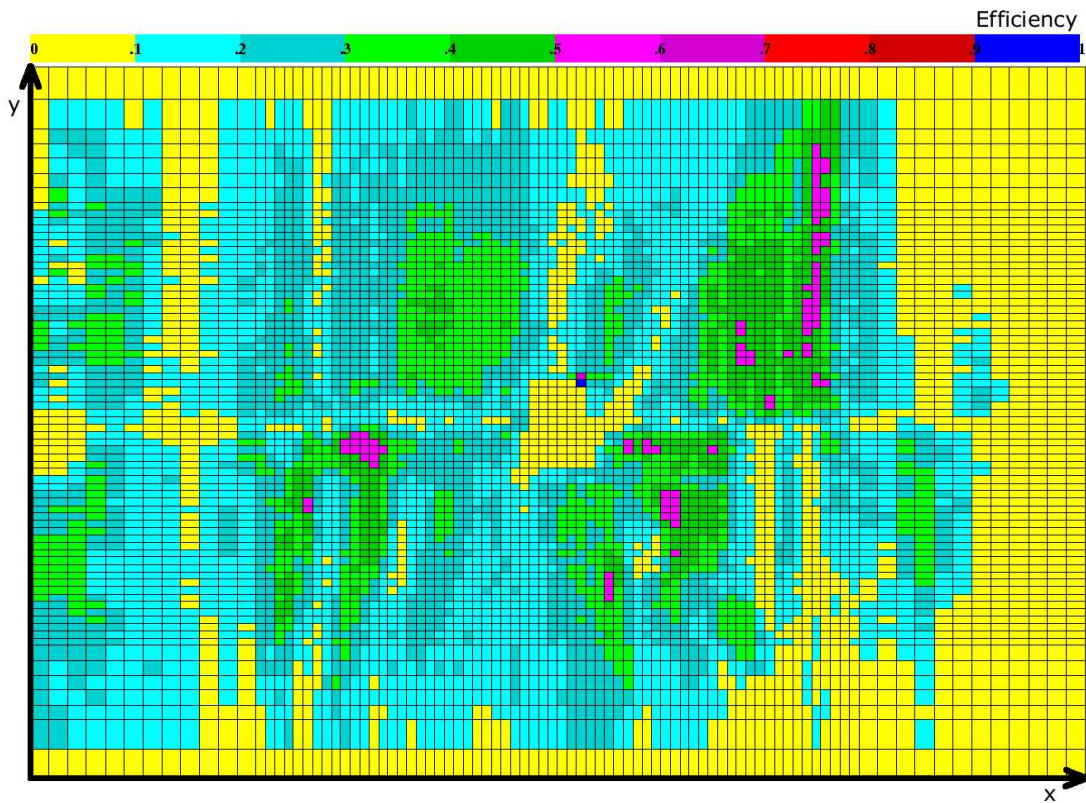


Figure 3.9: *FLT efficiency averaged over the datataking period in the $x - y$ plane at the z position of tracker station TC2 (generated with [Bal03]).*

3.3.2 Corrections for the Acceptance Difference of Opposite- and Likesign Data

The dilepton trigger implemented at HERA-b has two stages that have to be considered for the acceptance correction: the First Level Trigger (FLT) and the Second Level Trigger (SLT). The FLT starts from pretrigger messages sent by the muon system and then tries to follow the tracks through the muon stations MU4, MU3 and MU1 and the tracking stations TC2, TC1, PC4 and PC1. The SLT uses a full detector simulation to reconstruct tracks starting with the same pretrigger message. After the track reconstruction, the vertex is determined using the VDS system. Since the vertex system is located between wire target and magnet, the path of tracks through the VDS is independent of their charge and determined by their momentum vectors only.

The process from which the muon tracks originate does have an influence on the vertexing efficiency. Muons from Drell Yan or a J/ψ decay are more likely to pass the vertex criterion of the trigger, since they come from a common vertex. Muons from the decay of a kaon or a pion are less likely to combine to a vertex with low χ^2 . Provided the muons are created by the same process – combinatorial background or Drell Yan – the vertexing efficiency only depends on the momentum vector of the tracks, not their charge.

During the data taking period of 2002-2003, the HERA-b trigger ran in the so called “1FLT/2SLT*” (star) mode. In this mode, the FLT is used as a count trigger which simply counts the number of tracks found. The SLT reconstructs the leptons independently of the FLT, starting at the pretrigger seeds passed on from the FLT. The final trigger decision requires two pretrigger messages and one track from the FLT and at least two tracks with a common vertex from the SLT. The only connection between the two tracks of each muon pair in the SLT comes from the vertexing, which is not sensitive to the muon charges. Apart from this, both tracks are reconstructed independently in both triggers. The probability to detect a pair of muons with momenta \vec{p}_L and \vec{p}_R and charges q_L and q_R can then be written as the product of the probabilities to detect the single muons ($P_{\mu^L}(\vec{p}_L, q_L)$, $P_{\mu^R}(\vec{p}_R, q_R)$) and the vertexing efficiency ($\varepsilon_{\text{vertex}}$):

$$P_{\mu^L\mu^R}(\vec{p}_L, q_L, \vec{p}_R, q_R) = P_{\mu^L}(\vec{p}_L, q_L)P_{\mu^R}(\vec{p}_R, q_R)\varepsilon_{\text{vertex}}(\vec{p}_L, \vec{p}_R)$$

The indices L and R denote the left and right muon of each muon pair, as seen from the interaction point. Since the FLT and SLT efficiencies are independent of each other and it is not known which muon fulfilled the FLT requirement to find at least one muon track, the single track muon probabilities P_{μ^L} and P_{μ^R} have to be further separated. The three possible trigger combinations are:

- The two pretrigger messages lead to tracks found by both triggers,
- the left muon was found by both the FLT and the SLT, the right one only by the SLT, or

- the left muon was only found in the SLT, while the right muon was triggered by both the FLT and the SLT.

This leads to the event detection probability:

$$P_{\mu^L\mu^R}(\vec{p}_L, q_L, \vec{p}_R, q_R) = \left(P_{\mu^L}^{\text{FLT}}(\vec{p}_L, q_L) P_{\mu^R}^{\text{SLT}}(\vec{p}_R, q_R) + P_{\mu^L}^{\text{SLT}}(\vec{p}_L, q_L) P_{\mu^R}^{\text{FLT}}(\vec{p}_R, q_R) - P_{\mu^L}^{\text{FLT}}(\vec{p}_L, q_L) P_{\mu^R}^{\text{FLT}}(\vec{p}_R, q_R) \right) \varepsilon_{\text{vertex}}(\vec{p}_L, \vec{p}_R) \quad (3.1)$$

The pretrigger efficiencies are included in the trigger probabilities.

In a Monte Carlo simulation, all tracks accepted by the FLT are also accepted by the SLT, the sample of FLT triggered tracks is a subset of the sample of SLT triggered tracks. Therefore, both probabilities $P_{\mu^L}^{\text{FLT}}(\vec{p}_L, q_L) P_{\mu^R}^{\text{SLT}}(\vec{p}_R, q_R)$ and $P_{\mu^L}^{\text{SLT}}(\vec{p}_L, q_L) P_{\mu^R}^{\text{FLT}}(\vec{p}_R, q_R)$ include the probability to find both tracks in the FLT $P_{\mu^L}^{\text{FLT}}(\vec{p}_L, q_L) P_{\mu^R}^{\text{FLT}}(\vec{p}_R, q_R)$. This probability is thus counted twice and has to be subtracted once.

If the single track muon probabilities P are known, it is possible to calculate event weights that reflect the difference in acceptance between two charge combinations (q_L, q_R) and (q'_L, q'_R) for a given muon pair with momenta (\vec{p}_L, \vec{p}_R) :

$$w(\vec{p}_L, \vec{p}_R, q_L, q'_L, q_R, q'_R) = \frac{P(\vec{p}_L, q'_L, \vec{p}_R, q'_R)}{P(\vec{p}_L, q_L, \vec{p}_R, q_R)} \quad (3.2)$$

This event weight gives the probability that a muon pair accepted by the trigger with momenta (\vec{p}_L, \vec{p}_R) and charges (q_L, q_R) would also have been accepted if their momenta had been the same but the charges had been (q'_L, q'_R) . As discussed above, the vertexing efficiency only depends on the momentum vectors of the muons and the process the muons come from, not the charges. The only difference between the two probabilities in (3.2) is the charge of the muons, creation process and momentum vectors are the same. Thus, the vertexing efficiency is also the same in both cases and cancels out in the ratio of the two probabilities.

3.3.3 Single Track Monte Carlo to calculate Acceptance Correction Factors

While it is not possible to generate a full Monte Carlo simulation of the combinatorial background, a simpler model can be used to find the single track detection probabilities described in the previous section. For this purpose, a special Single Track Monte Carlo (STMC) sample was generated in which each event consists of only a single muon of varying momentum and charge. These muons were generated in equal amounts for both charges with a flat distribution in p_x and p_y ,

distributed throughout the whole detector (see Fig. 3.10). The p_z of the tracks was sampled during the Monte Carlo generation from a histogram showing the p_z distribution of likesign data tracks. This constraint on the longitudinal momentum leads to a limit on the usable total momentum of muons. Outside a momentum range of $10 \text{ GeV} < p < 106 \text{ GeV}$, the likesign data sample is too small to be used during the p_z sampling described above. To ensure that this limit on the Single Track Monte Carlo muons introduces no bias in the correction weights for the acceptance differences, muons outside the momentum range given above are also removed from unlikesign data and Drell Yan Monte Carlo. This leads to an loss of efficiency of 4.2%. The sample was reconstructed using a modified trigger simulation which skipped the vertexing stage of the SLT and applied flags to each track whether it was accepted by both triggers or by the SLT only. The result of this are four Monte Carlo selections:

- μ^+ accepted by both FLT and SLT,
- μ^+ accepted by SLT only,
- μ^- accepted by both FLT and SLT, and
- μ^- accepted by SLT only.

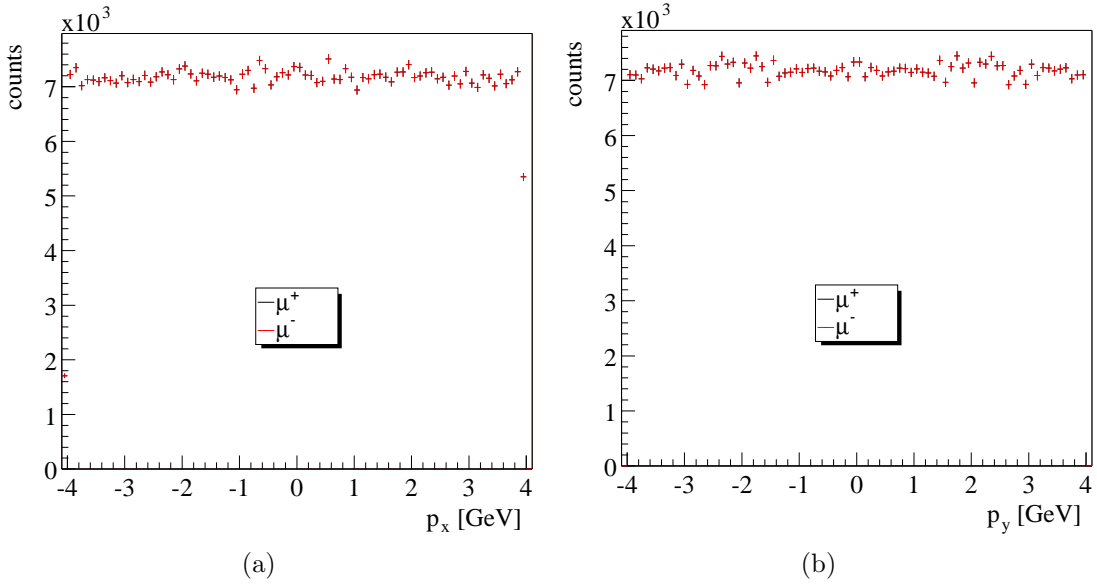


Figure 3.10: *Distributions of p_x and p_y of generated Single Track Monte Carlo muons. The data points of the μ^+ distribution hide those of the μ^- distribution as both are identical.*

The p_x and p_y distributions of accepted events for the four selections are shown in Fig. 3.11 and 3.12. The p_x distributions show large differences between μ^+ and

μ^- because of the different bending direction in the magnet. Also the difference in trigger efficiency is evident in the different numbers of accepted events. Also evident is the difference in efficiency of the First and the Second Level Trigger. Comparing Fig. 3.11(a) and 3.11(c) leads to roughly a factor of eight between the two efficiencies (see also Tab. 3.2). Fig. 3.13 illustrate the cause of this difference in FLT and SLT acceptance. They show the position of the tracks accepted by each trigger in the magnet focal plane. While the tracks accepted by the SLT are distributed throughout the detector with the exception of the central inner tracker region and the “shadow” in the lower right quadrant caused by the electron beampipe, the FLT triggered track distribution shows many low efficiency regions which roughly match the areas of low efficiency seen in Fig. 3.9.

Trigger	generated muons	accepted muons	trigger efficiency
FLT	574523	38214	6.6%
SLT	574523	312757	54.4%

Table 3.2: *Generated and accepted muon tracks for both triggers and corresponding trigger efficiencies in the Single Track Monte Carlo.*

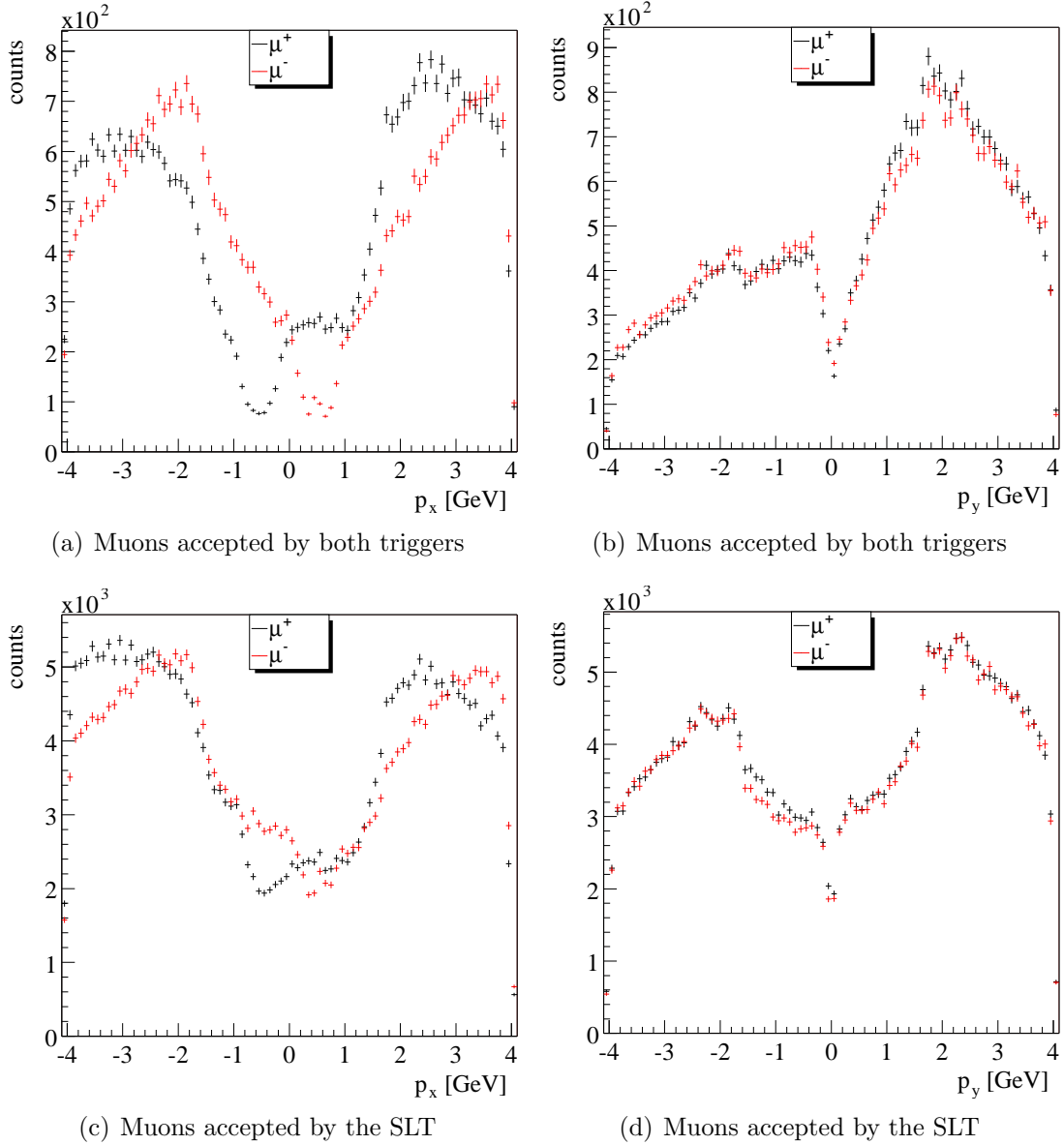
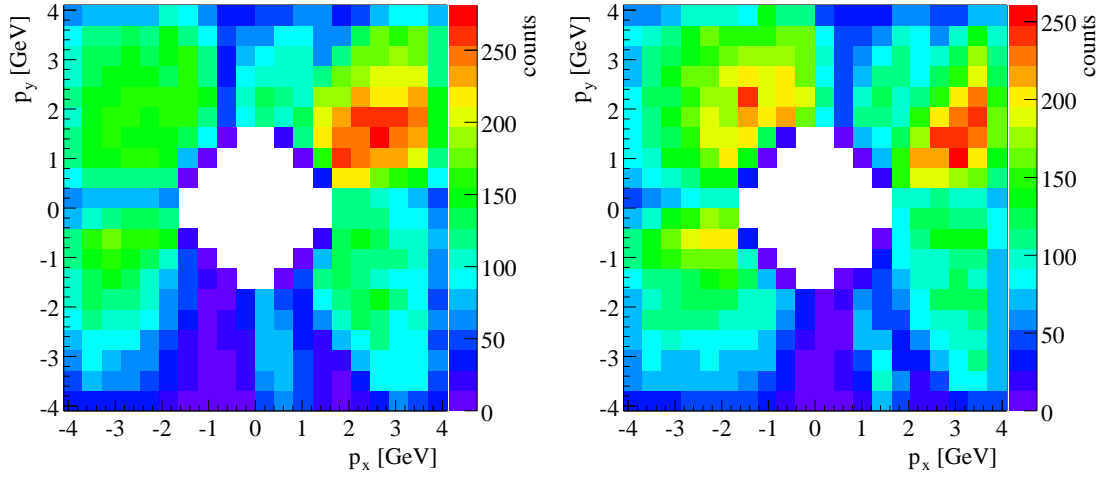
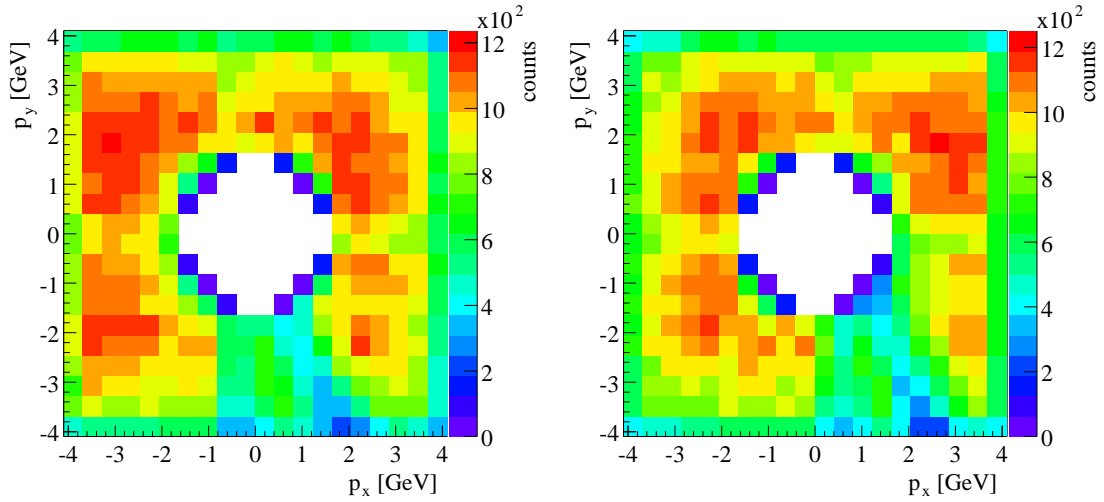


Figure 3.11: *Distributions of p_x and p_y of reconstructed Single Track Monte Carlo muons that were accepted by both the FLT and the SLT (a and b). Muons with a negative p_y are less likely to be detected, as expected from Fig. 3.9 since the FLT efficiency generally is higher in the upper half of the detector. The same distributions requiring only an SLT trigger flag (c and d) show a much less pronounced asymmetry in p_y since most of this asymmetry is caused by FLT inefficiencies. The remaining asymmetry is caused by the electron beampipe.*

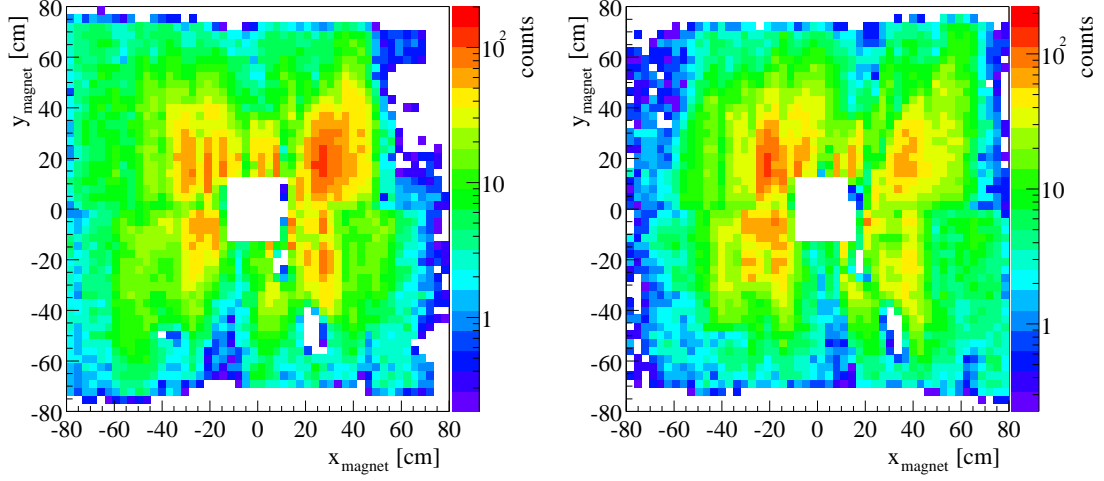


(a) Positive muons accepted by both triggers (b) Negative muons accepted by both triggers

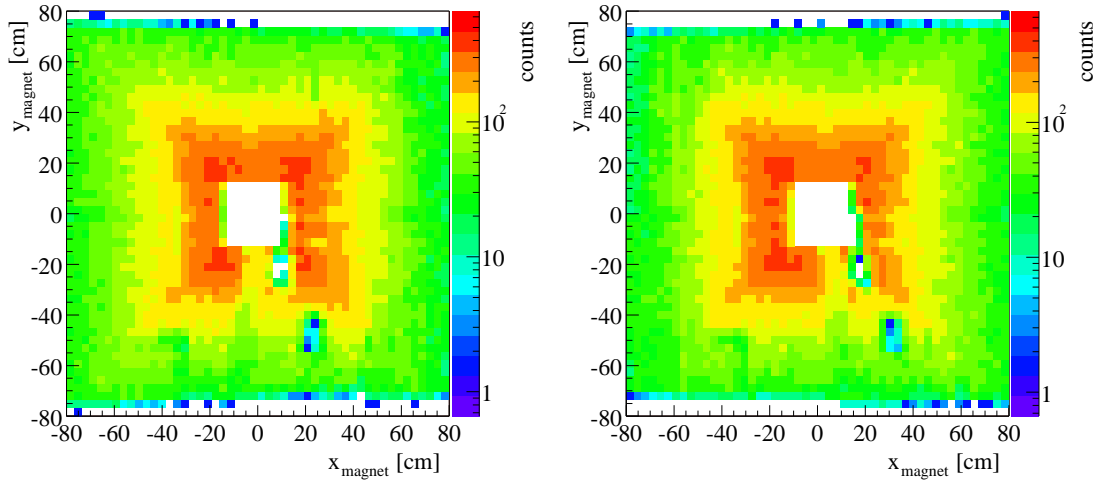


(c) Positive muons accepted by the SLT (d) Negative muons accepted by the SLT

Figure 3.12: Distributions of p_x vs. p_y of (a) positive and (b) negative reconstructed Single Track Monte Carlo muons accepted by both triggers and (c) positive and (d) negative muons requiring only a SLT trigger flag.



(a) Positive muons accepted by both triggers (b) Negative muons accepted by both triggers



(c) Positive muons accepted by the SLT (d) Negative muons accepted by the SLT

Figure 3.13: Track position in the magnet focal plane of (a) positive and (b) negative reconstructed Single Track Monte Carlo muons detected by both triggers. The inefficiency regions closely match those seen in 3.9. Requiring only an SLT trigger flag (c and d) shows a much smoother distribution, only disturbed by the electron beampipe passing through the detector in the lower right quadrant.

3.3.4 Reweighting of Likesign Data to the Acceptance of the Opposite sign Background

Using these Single Track Monte Carlo selections, it is possible to calculate the single track detection probabilities $P_{\mu^L}(\vec{p}_L, q_L)$ and $P_{\mu^R}(\vec{p}_R, q_R)$ used in (3.1). Since the detection efficiency depends on geometrical detector effects such as inefficient chambers, these probabilities are calculated as a function of the geometrical variables $(p, x_{\text{magnet}}, y_{\text{magnet}}, q)$ instead of the momentum vector (\vec{p}, q) . Mathematically, both sets of variables are equivalent, the latter is used in the formulas for clarity.

The two generated (μ^+ and μ^-) and four accepted (μ_{FLT}^+ , μ_{SLT}^+ , μ_{FLT}^- and μ_{SLT}^-) Single Track Monte Carlo samples are divided into ten momentum subsets. Two dimensional histograms are filled with the $x - y$ position of the muon in the magnet focal plane from these subsets. A four dimensional efficiency matrix $P(p, x_{\text{magnet}}, y_{\text{magnet}}, q)$ is then obtained by dividing the histograms filled with accepted by the corresponding ones with generated MC data, once for each trigger. Finally, a local averaging is applied to the $x - y$ distributions in the form of a bilinear interpolation.

To keep the equations readable, the following substitutions are applied in the calculation of the relative acceptance of likesign to the unlikesign events:

$$\begin{aligned}
P_{\mu^L\mu^R}(\vec{p}_L, +, \vec{p}_R, -) &\longrightarrow P^{+-}(\vec{p}_L, \vec{p}_R), & P_{\mu^L\mu^R}(\vec{p}_L, -, \vec{p}_R, +) &\longrightarrow P^{-+}(\vec{p}_L, \vec{p}_R) \\
P_{\mu^L\mu^R}(\vec{p}_L, +, \vec{p}_R, +) &\longrightarrow P^{++}(\vec{p}_L, \vec{p}_R), & P_{\mu^L\mu^R}(\vec{p}_L, -, \vec{p}_R, -) &\longrightarrow P^{--}(\vec{p}_L, \vec{p}_R) \\
P_{\mu^L}^{\text{FLT}}(\vec{p}_L, +) &\longrightarrow P_F^{+L}, & P_{\mu^L}^{\text{SLT}}(\vec{p}_L, +) &\longrightarrow P_S^{+L} \\
P_{\mu^R}^{\text{FLT}}(\vec{p}_R, +) &\longrightarrow P_F^{+R}, & P_{\mu^R}^{\text{SLT}}(\vec{p}_R, +) &\longrightarrow P_S^{+R} \\
P_{\mu^L}^{\text{FLT}}(\vec{p}_L, -) &\longrightarrow P_F^{-L}, & P_{\mu^L}^{\text{SLT}}(\vec{p}_L, -) &\longrightarrow P_S^{-L} \\
P_{\mu^R}^{\text{FLT}}(\vec{p}_R, -) &\longrightarrow P_F^{-R}, & P_{\mu^R}^{\text{SLT}}(\vec{p}_R, -) &\longrightarrow P_S^{-R}
\end{aligned}$$

The event detection probabilities (3.1) of the four charge combinations then are:

$$P^{+-}(\vec{p}_L, \vec{p}_R) = (P_F^{+L}P_S^{-R} + P_S^{+L}P_F^{-R} - P_F^{+L}P_F^{-R})\varepsilon_{\text{vertex}}(\vec{p}_L, \vec{p}_R) \quad (3.3a)$$

$$P^{-+}(\vec{p}_L, \vec{p}_R) = (P_F^{-L}P_S^{+R} + P_S^{-L}P_F^{+R} - P_F^{-L}P_F^{+R})\varepsilon_{\text{vertex}}(\vec{p}_L, \vec{p}_R) \quad (3.3b)$$

$$P^{++}(\vec{p}_L, \vec{p}_R) = (P_F^{+L}P_S^{+R} + P_S^{+L}P_F^{+R} - P_F^{+L}P_F^{+R})\varepsilon_{\text{vertex}}(\vec{p}_L, \vec{p}_R) \quad (3.3c)$$

$$P^{--}(\vec{p}_L, \vec{p}_R) = (P_F^{-L}P_S^{-R} + P_S^{-L}P_F^{-R} - P_F^{-L}P_F^{-R})\varepsilon_{\text{vertex}}(\vec{p}_L, \vec{p}_R) \quad (3.3d)$$

Using these four formulas, it is possible to calculate the probability that a muon pair with given momenta and likesign charge would also have been accepted if one muon had the opposite charge by dividing the probability of the changed unlikesign charge combination ((3.3a) or (3.3b)) by the probability of the original

likesign one ((3.3c) or (3.3d)). This leads to four weights (3.2), two for reweighting positive likesign data to simulate outbending and inbending opposite sign background, and two for reweighting negative likesign data to outbending and inbending background:

$$w_{++}^{+-}(\vec{p}_L, \vec{p}_R) = \frac{P^{+-}(\vec{p}_L, \vec{p}_R)}{P^{++}(\vec{p}_L, \vec{p}_R)} = \frac{P_F^{+L} P_S^{-R} + P_S^{+L} P_F^{-R} - P_F^{+L} P_F^{-R}}{P_F^{+L} P_S^{+R} + P_S^{+L} P_F^{+R} - P_F^{+L} P_F^{+R}} \quad (3.4a)$$

$$w_{++}^{-+}(\vec{p}_L, \vec{p}_R) = \frac{P^{-+}(\vec{p}_L, \vec{p}_R)}{P^{++}(\vec{p}_L, \vec{p}_R)} = \frac{P_F^{-L} P_S^{+R} + P_S^{-L} P_F^{+R} - P_F^{-L} P_F^{+R}}{P_F^{+L} P_S^{+R} + P_S^{+L} P_F^{+R} - P_F^{+L} P_F^{+R}} \quad (3.4b)$$

$$w_{--}^{+-}(\vec{p}_L, \vec{p}_R) = \frac{P^{+-}(\vec{p}_L, \vec{p}_R)}{P^{--}(\vec{p}_L, \vec{p}_R)} = \frac{P_F^{+L} P_S^{-R} + P_S^{+L} P_F^{-R} - P_F^{+L} P_F^{-R}}{P_F^{-L} P_S^{-R} + P_S^{-L} P_F^{-R} - P_F^{-L} P_F^{-R}} \quad (3.4c)$$

$$w_{--}^{-+}(\vec{p}_L, \vec{p}_R) = \frac{P^{-+}(\vec{p}_L, \vec{p}_R)}{P^{--}(\vec{p}_L, \vec{p}_R)} = \frac{P_F^{-L} P_S^{+R} + P_S^{-L} P_F^{+R} - P_F^{-L} P_F^{+R}}{P_F^{-L} P_S^{-R} + P_S^{-L} P_F^{-R} - P_F^{-L} P_F^{-R}} \quad (3.4d)$$

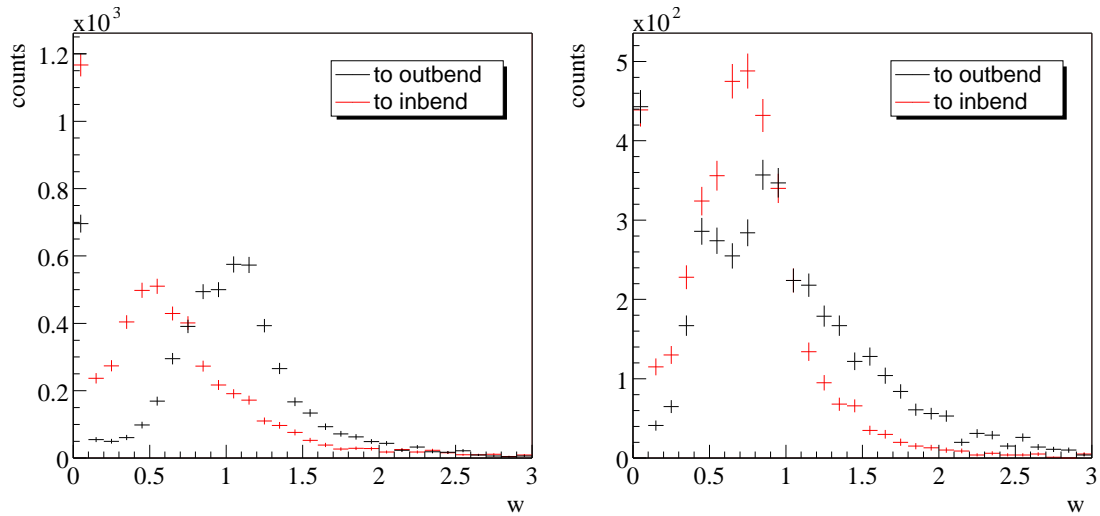
These ratios w (3.4a) to (3.4d) can be applied as event weights to correct the likesign background to the acceptance of the opposite sign background. Fig. 3.2(a) shows that the data sample containing outbending opposite sign muon pairs is larger than that containing inbending ones. Consequently it is expected that weights correcting the acceptance difference between likesign and outbending opposite sign $(-+)$ data are on average larger than those correcting to inbending opposite sign $(+-)$ data. Both distributions in Fig. 3.14 show this clearly: $\langle w_{++}^{-+} \rangle = 0.9 > \langle w_{++}^{+-} \rangle = 0.6$ and $\langle w_{--}^{-+} \rangle = 0.9 > \langle w_{--}^{+-} \rangle = 0.7$. Also, it can be seen in Fig. 3.2(b) that the sample of positive likesign is larger than that of negative likesign muon pairs. Thus the weights applied to positive likesign data should be smaller on average than those to negative likesign. In the case of reweighting to inbending acceptance, this is the case in Fig. 3.14. For reweighting to outbending acceptance, a prediction of the average weight is not possible, as neither likesign sample can be reweighted to simulate the outbending background alone. According to Fig. 3.14, both weights have the same average.

This strong dependence of the weights on the charge combinations shows that the reweighting of the likesign data to the acceptance of the opposite sign background is an essential part of the background subtraction.

Assuming that the number of background events per charge combination fulfill the relation $N_{\mu^+\mu^+} = N_{\mu^-\mu^-} = N_{\mu^+\mu^-} = N_{\mu^-\mu^+}$ at generation, the number of Drell Yan signal events can then be calculated as:

$$N_{\text{DY}} = N_{\text{total}}^{+-} + N_{\text{total}}^{-+} - \frac{1}{2} \sum_{i=1}^{N_{++}} w_{++}^{+-}(\vec{p}_L, \vec{p}_R) - \frac{1}{2} \sum_{i=1}^{N_{++}} w_{++}^{-+}(\vec{p}_L, \vec{p}_R) - \frac{1}{2} \sum_{i=1}^{N_{--}} w_{--}^{+-}(\vec{p}_L, \vec{p}_R) - \frac{1}{2} \sum_{i=1}^{N_{--}} w_{--}^{-+}(\vec{p}_L, \vec{p}_R) \quad (3.5)$$

The factors $\frac{1}{2}$ are necessary since each likesign event is counted twice, once

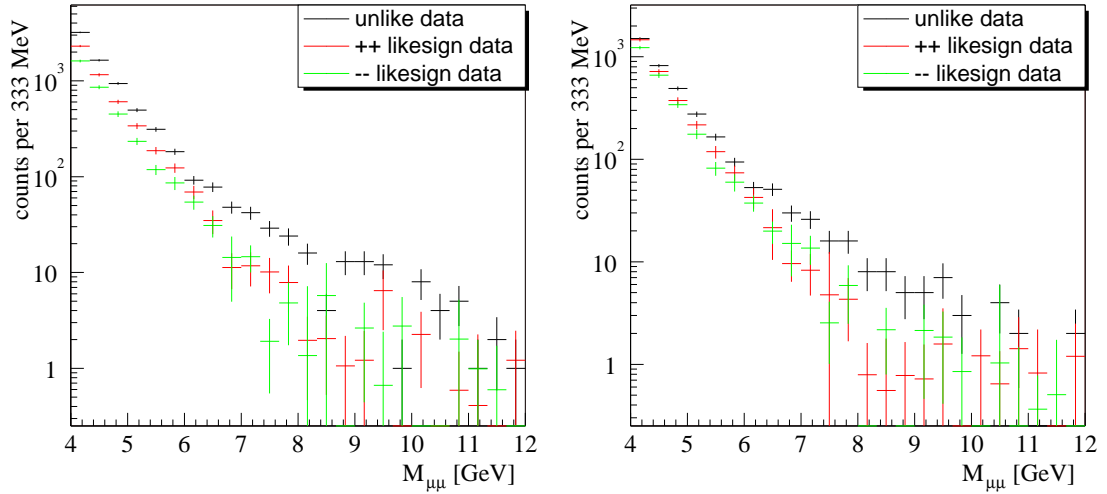


(a) Weights applied to positive likesign data (b) Weights applied to negative likesign data

Figure 3.14: *Distribution of the weights that are applied to likesign data and calculated according to (3.4). The weights applied to positive likesign data are plotted in (a), those used to reweight negative likesign data in (b). The large entries at zero come from likesign muon pairs that would not have been seen by the detector if their charges had been unlike.*

reweighted to simulate outbending background, once to simulate inbending. The mass distribution of all data sets after the likesign acceptance correction is shown in Fig. 3.15. These simulated opposite sign background distributions can now be used in a study to optimise the signal to background ratio by using kinematic selections. They can also be subtracted from the unlikesign data to extract the Drell Yan signal.

A crosscheck of the method applied above is given in the next section.



(a) Outbending unlikesign and reweighted likesign data

(b) Inbending unlikesign and reweighted likesign data

Figure 3.15: Mass distribution of the data after fiducial cuts and likesign reweighting. (a) Outbending and (b) inbending muon pairs, each with corresponding simulated opposite sign background from reweighted likesign distributions. While the positive and negative likesign distributions agree within errors after reweighting to the acceptance of inbending data, the two likesign distributions after reweighting to outbending acceptance differ significantly, as expected (see Sec. 3.3).

3.3.5 Crosscheck of Acceptance Reweighting Method

The acceptance reweighting method described in the last section can be checked by applying the event detection probability shown in Eq. (3.1) as a weight to each generated Drell Yan Monte Carlo event and comparing the result to the reconstructed Drell Yan Monte Carlo. Since the vertexing efficiency $\varepsilon_{\text{vertex}}(\vec{p}_L, \vec{p}_R)$ contained in Eq. (3.1) is not known, only the track efficiencies will be used:

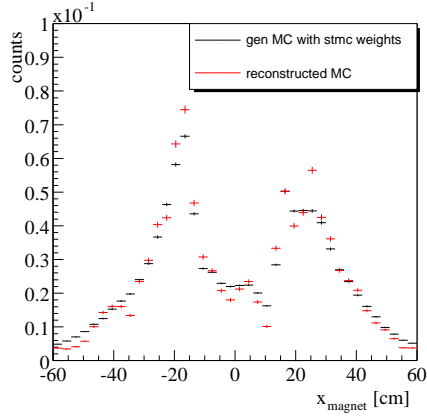
$$P_{\mu^L\mu^R}(\vec{p}_L, q_L, \vec{p}_R, q_R)^* = \left(P_{\mu^L}^{\text{FLT}}(\vec{p}_L, q_L)P_{\mu^R}^{\text{SLT}}(\vec{p}_R, q_R) + P_{\mu^L}^{\text{SLT}}(\vec{p}_L, q_L)P_{\mu^R}^{\text{FLT}}(\vec{p}_R, q_R) - P_{\mu^L}^{\text{FLT}}(\vec{p}_L, q_L)P_{\mu^R}^{\text{FLT}}(\vec{p}_R, q_R) \right) \quad (3.6)$$

The result will not be an exact match between the two samples due to the missing vertexing efficiency, which can of course depend on the kinematic variables. The comparison is still useful, as though the exact dependance of the vertexing efficiency is not known, one expects the shape of the functions to be smooth.

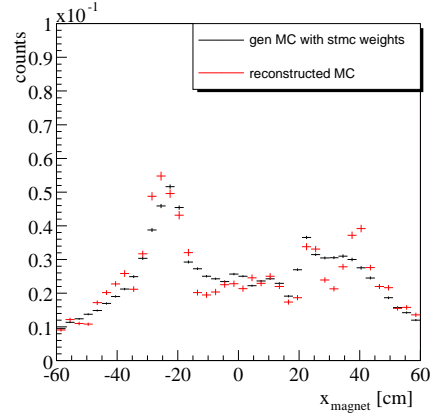
Fig. 3.16 shows the x positions of tracks at three different z positions in the detector both from the reconstructed and the generated Drell Yan Monte Carlo simulation. To the latter the probabilities given in Eq. (3.6) are applied as event weights. These geometrical distributions are chosen because they directly show the influence of the acceptance differences. Both distributions are normalized to an area of one. While the general shape of the distributions is reproduced, efficiency differences on small scales are naturally not reproduced in the reweighted generated Monte Carlo distributions, due to the averaging effect of the rather coarse grained Single Track Monte Carlo efficiency matrix. An exact reproduction of geometrical distributions is not necessary, as the ones in which the background subtraction is finally applied are kinematic distributions, which themselves average over the geometry. If the Single Track efficiencies correctly reflect the reconstruction efficiencies in the Drell Yan Monte Carlo simulation, the kinematic distributions should be identical except for the vertexing efficiency, which itself can be a function of the plotted variable.

Two kinematic distributions are plotted in Fig. 3.17. The left plots show the distributions of generated Drell Yan Monte Carlo data, to which Single Track Monte Carlo weights have been applied, and those of accepted Drell Yan Monte Carlo data as a function of the reconstructed mass and the transverse momentum of the muon pair. As expected the integrals of the reweighted generated Monte Carlo distributions are larger than those of the accepted Monte Carlo distributions by roughly a factor of three due to the vertexing efficiency not present in the reweighted generated Monte Carlo sample. The right plots show a ratio of the two distributions on the left side, which corresponds to the missing vertexing efficiency. As one can see in both kinematic distributions this is a smooth function.

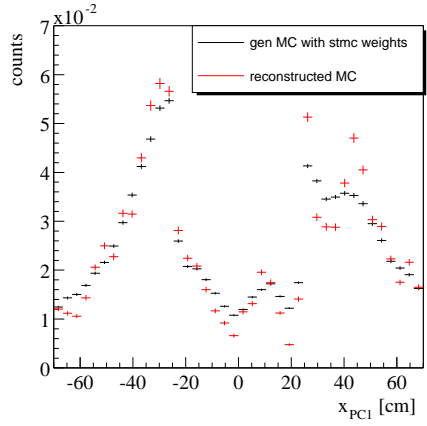
The crosscheck shows no evidence of problems with the calculation of event weights from the Single Track Monte Carlo, the differences between the reweighted generated and reconstructed distributions are compatible with the explanation of the missing vertexing efficiency.



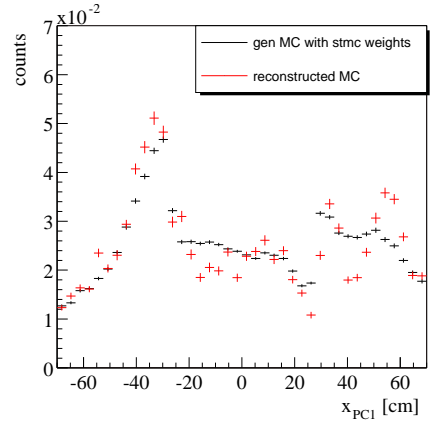
(a) Outbending muon pairs



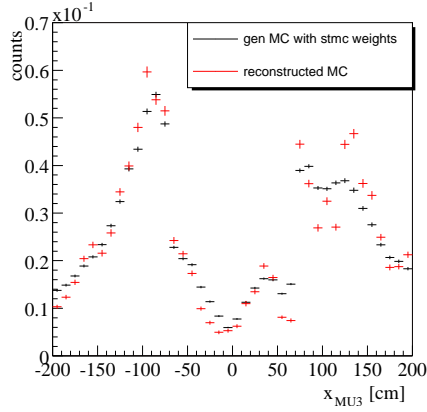
(b) Inbending muon pairs



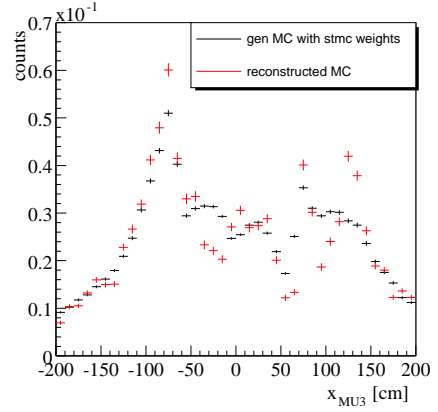
(c) Outbending muon pairs



(d) Inbending muon pairs

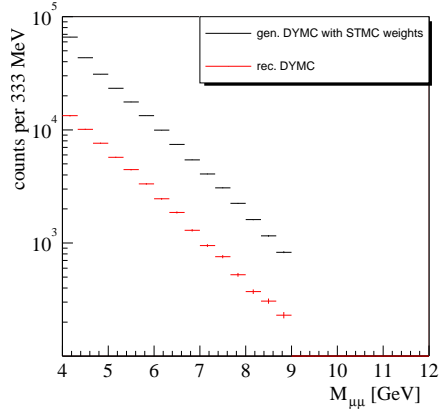


(e) Outbending muon pairs

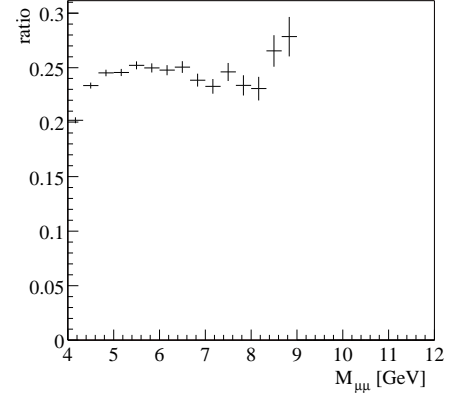


(f) Inbending muon pairs

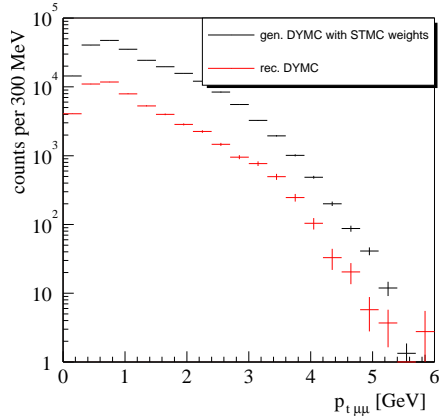
Figure 3.16: Comparison between the x position of tracks in the magnet focal plane (a and b), in station PC1 (c and d) and in station MU3 (e and f). The left distributions show outbending, the right inbending muon pairs. Both reconstructed and generated Drell Yan Monte Carlo are shown. Single Track Monte Carlo weights have been applied to generated Drell Yan Monte Carlo events according to Eq. (3.3a) and (3.3b), without the vertexing efficiency ϵ_{vertex} .



(a) Mass of muon pair



(b) Ratio of mass distributions



(c) Transverse momentum of muon pair

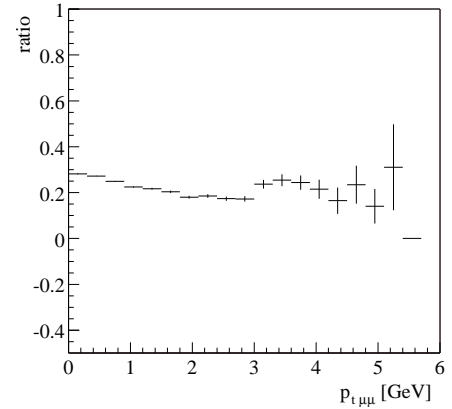
(d) Ratio of p_t distributions

Figure 3.17: Comparisons of kinematic distributions between reconstructed and reweighted generated Drell Yan Monte Carlo. The weights applied to the generated distributions are calculated from Single Track Monte Carlo. The left distributions show the original distributions, the right ones the ratio of the two, which corresponds to the vertexing efficiency.

3.4 Simulation of the Drell Yan Process

The Monte Carlo simulations used at HERA-b use the physics generator packages PYTHIA 5.7 and JETSET 7.4 ([Sjö94]). They are limited to proton nucleon interactions and generate the particles belonging to the Drell Yan reaction itself. All other particles present in an inelastic proton nucleon interaction are generated by the FRITIOF 7.02 package ([Pi92]) with the constraint that the sum of the energies of particles from the inelastic collision and the Drell Yan process are equal to the beam energy.

This event is then fed into a GEANT 3.21 ([Cer94]) detector simulation, which tracks the Monte Carlo particles through the detector. This leads to simulated hits after a digitalization and hit generation. Finally, a simulation of the HERA-b trigger chain is applied. In this simulation, the order in which the triggers are applied is reversed with respect to real data. A simulation of the Second Level Trigger (SLT) is fed with the hit informations from the Monte Carlo tracks passing through the pretrigger detectors. Since the hit information is in the same format as the real data, the same trigger algorithms can be used. The trigger track parameters determined by the SLT are then passed on to the First Level Trigger (FLT) simulation. The FLT efficiency is then determined from a FLT efficiency map, which is a parametrization of the FLT efficiency in relation to the SLT efficiency. A projection of this FLT efficiency map into the plane of station TC2 is shown in Fig. 3.9.

The Monte Carlo runs used in the analysis are listed in table 3.3. After a first loose set of preselection criteria (similar to those discussed later in Sec. 3.5) was applied to Drell Yan Monte Carlo and data, several kinematic distributions of Monte Carlo and data were compared. While most differential kinematic distributions show good agreement between data and MC, the Drell Yan Monte Carlo simulation does not reproduce the distribution of the transverse momentum of the muon pair, as seen in Fig. 3.18. This is a known effect, also seen in the J/ψ analyses ([Hus05]). The Monte Carlo simulation only includes first order processes, while initial and final state radiation increase the transverse momentum. A second effect is that partons with a p_t of less than 1 GeV are dropped during generation, further distorting the p_t spectrum. These effects can be compensated for by reweighting the MC events. A simple reweight in p_t is not sufficient to correct for this distortion, as mass and p_t of the muon pair are correlated. For this reason, a two dimensional reweighting procedure is applied. Instead of mass and p_t , mass and p_t^2 are chosen, since the distribution of the latter has no peak and is easier to fit. The mass vs. p_t^2 distributions of both MC and data are separately fitted. Then for each Drell Yan Monte Carlo event, a weight is calculated from the ratio of the two fitting functions. Fig. 3.19 shows both distribution and fitting function of the reconstructed MC, Fig. 3.20 those of the data.

While the data distribution can be fitted with a simple two dimensional exponential function (Eq. 3.7), the phenomenological function used to fit the MC

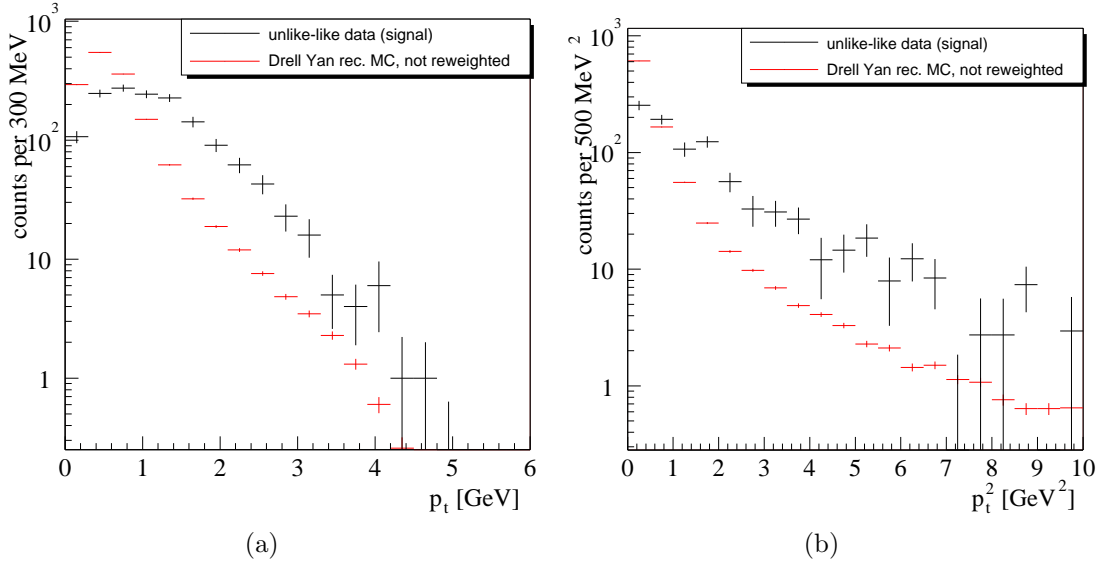


Figure 3.18: *Distribution of the transverse momentum of the muon pair in data and Monte Carlo with no reweighting applied to the Drell Yan Monte Carlo. The Drell Yan Monte Carlo distribution clearly peaks at a lower transverse momentum than the data distribution. p_t^2 was chosen as a reweighting variable since it is easier to fit as it contains no peak.*

distribution is more complicated (Eq. 3.8) and consists of 25 free parameters:

$$f_{\text{data}}(m, p_t^2) = \exp(c_0 + c_1 m + c_2 p_t^2) \quad (3.7)$$

$$f_{\text{MC}}(m, p_t^2) = g(m, p_t^2) \times h(p_t^2) + i(m, p_t^2) \quad (3.8)$$

The p_t^2 dependence of the MC distribution can be described by a sum of two exponential functions. A suitable function for the mass dependence was found in BaBar literature, the so called Novosibirsk function $g(m, p_t^2)$ ([Ada05]):

$$g(m, p_t^2) = c_0 \left[\exp \left[-\frac{1}{2} \left(\frac{\ln^2 \left(1 + \frac{\sinh(\hat{c}_3 \sqrt{\ln 4})}{\sqrt{\ln 4}} \cdot \frac{m - \hat{c}_1}{\hat{c}_2} \right)}{\hat{c}_3^2} + \hat{c}_3^2 \right) \right] - \hat{c}_4 \right] \quad (3.9)$$

Especially the peak position \hat{c}_1 , but also the other parameters of the Novosibirsk function show a dependence on the transverse momentum. This can be seen in Fig. 3.19(a). For $p_t^2 = 0.5 \text{ GeV}^2$, the peak of the mass distribution is outside the graph, below 4 GeV. For $p_t^2 = 3.5 \text{ GeV}^2$, the peak is at $M_{\mu\mu} = 4.75 \text{ GeV}$. To find the subfunctions (3.10) to (3.13), the Drell Yan Monte Carlo data was plotted as a function of the mass $M_{\mu\mu}$ in ten bins of p_t^2 . Each of these ten distributions was fitted separately with a Novosibirsk function whose parameters were then plotted

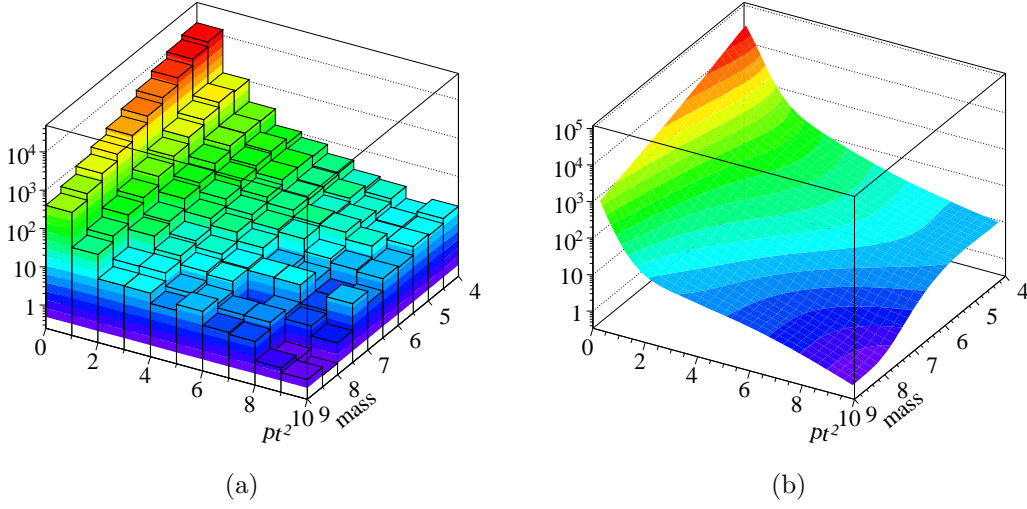


Figure 3.19: (a) mass vs. p_t^2 distribution of reconstructed Drell Yan Monte Carlo events, (b) corresponding fit.

as a function of p_t^2 . Phenomenological fits to these distributions of parameters are:

$$\hat{c}_1 = c_1 \left(1 - \frac{1}{c_{11} + c_{12}p_t^2} \right) \quad (3.10)$$

$$\hat{c}_2 = c_2(1 + c_{13}p_t^2 + c_{14}p_t^4) \quad (3.11)$$

$$\hat{c}_3 = c_3(1 + c_{15}p_t^2 + c_{16}p_t^4) \quad (3.12)$$

$$\hat{c}_4 = c_4(1 + c_{17}p_t^2 + c_{18}p_t^4) \quad (3.13)$$

$$h(p_t^2) = c_5 e^{c_6 + c_7 p_t^2} + c_8 e^{c_9 + c_{10} p_t^2} \quad (3.14)$$

Still, the Novosibirsk function alone multiplied with the sum of two exponential functions of p_t^2 was insufficient to fully describe the Monte Carlo distribution. A third exponential term depending on both $M_{\mu\mu}$ and p_t^2 was needed:

$$i(m, p_t^2) = c_{26} \exp \left[(c_{21} + c_{19}p_t^2 + c_{20}p_t^4) \ln m + c_{22}m^2 + c_{23}m^3 + c_{24} \ln p_t^2 + c_{25}p_t^4 \right] \quad (3.15)$$

The result of this reweighting can be seen in Fig. 3.21. Here, data and Monte Carlo simulated distributions agree well. This reweighted Drell Yan Monte Carlo sample is then used again in an iterative process to optimize the cuts applied to data, which is again compared to the MC distributions and used to adjust the reweighting.

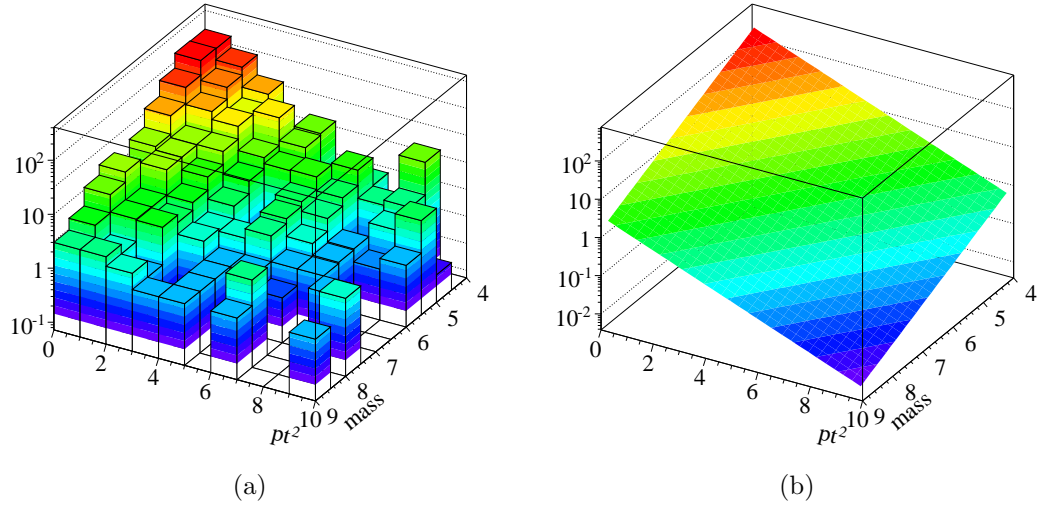


Figure 3.20: (a) mass vs. p_t^2 distribution of data events after cuts and likesign background subtraction, (b) corresponding fit.

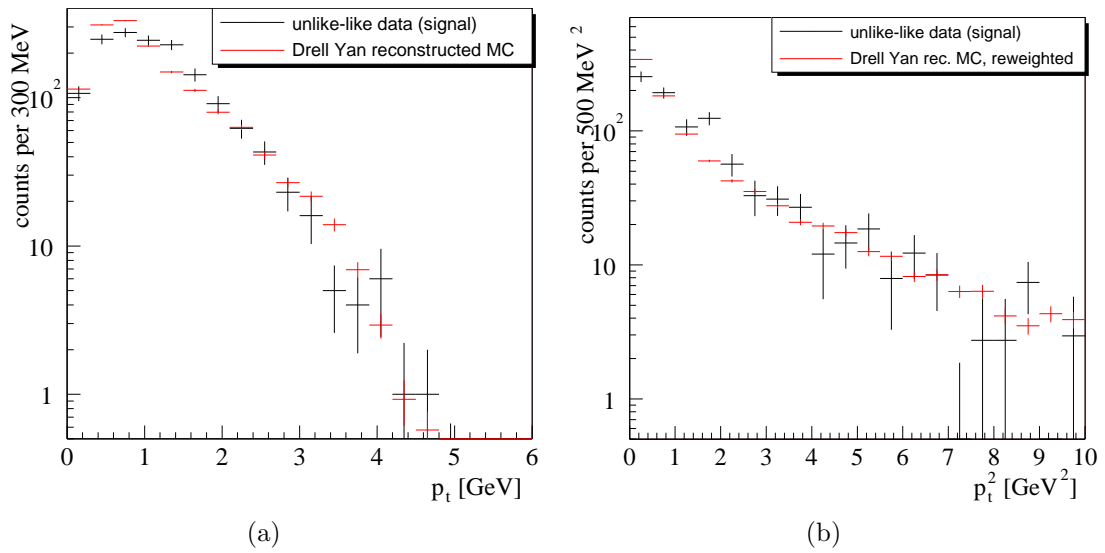


Figure 3.21: p_t and p_t^2 distribution in data and Monte Carlo simulation after reweighting. Data and Monte Carlo agree well.

wire	MC process id	#events (k)	calibration period	run number
b1	15200	379	Jan	09_1566
b1	15200	654	Jan	09_1567
b1(b1o2)	15200	333	Jan	09_1569
b1(b1o2)	15200	688	Jan	09_1570
b1(b1i2)	15200	524	Jan	09_1573
b1(i1b1)	15200	523	Nov	09_1580
b1(b1b2)	15200	524	Feb	09_1564
b1(b1b2)	15200	524	Oct	09_1581
b2	15202	315	Nov	09_1562
b2(b1b2)	15202	315	Oct	09_1563
b2(b1b2)	15203	585	Feb	09_1565
i1(i1i2)	15203	502	Nov	09_1575
i1(i1i2)	15203	401	Dec	09_1577
i1(i1b1)	15203	502	Nov	09_1579
i2	15200	1033	Nov	09_1558
i2(i1i2)	15200	654	Nov	09_1576
i2(i1i2)	15200	401	Dec	09_1578
i2(b1i2)	15200	523	Jan	09_1574
o2	15203	709	Feb	09_1568
o2(b1o2)	15203	465	Jan	09_1571
o2(b1o2)	15203	928	Jan	09_1572

Table 3.3: *List of Drell Yan Monte Carlo runs used.*

3.5 Optimization of Event Selection

In addition to the general event based and fiducial cuts introduced in Sec. 3, cuts on the properties of the muon tracks are applied.

The data sample suffers from a rather large background as can be seen in Fig. 3.15, which makes it difficult to measure Drell Yan cross sections and leads to large errors.

However, the ratio of signal to background can be improved by choosing appropriate cuts to reduce background while keeping a large portion of the signal.

As a first step in extracting the Drell Yan signal from the data, the invariant mass range of the reconstructed muon pair is restricted. Below 4 GeV, muon pairs coming from J/ψ decays contaminate the signal, while $\Upsilon(1S)$ decaying into $\mu^+\mu^-$ dominate the mass spectrum between 9.3 and 9.6 GeV. Also, above 9 GeV there is not sufficient signal leading to a final mass range of 4 to 9 GeV.

3.5.1 Consecutive Kinematic Cuts

Using the reweighted likesign dataset as background and the Monte Carlo simulation as signal, it is now possible to identify cut variables to improve the signal to background ratio.

The following variables show significant differences between signal and background and are used to improve the signal to background ratio:

- First, tracks with a high reduced χ^2 or $\frac{\chi^2}{\text{n.d.f.}}$ in the track fit are removed. High values point to badly reconstructed tracks or kinks due to decays in flight. Eliminating these tracks mainly removes muons coming from decays in flight and bad matches between track segments (Fig. 3.22(a)).
- Both muons from a Drell Yan process are generated at the interaction point in contrast to background muons. Muon pairs with a large significance of the distance between muon vertex and primary vertex $S_{\text{VV}} = \frac{\text{muon vertex} - \text{primary vertex distance}}{\sqrt{(\text{muon vertex error})^2 + (\text{primary vertex error})^2}}$, the impact parameter, are therefore rejected, reducing random combinations between decay muons (Fig. 3.22(b)).
- As a criterion of vertex quality, a cut on the distance of closest approach d_{doc} of both muons is applied, again removing random combinations of unrelated muons or muons coming from kaon or pion decays (Fig. 3.22(c)).
- Background muons from decays in flight have a lower value of the muon likelihood⁶ L_{μ} . A minimum cut on the product of the muon likelihood of both muons is applied (Fig. 3.22(d)).

⁶The tracking software used at HERA-b calculates for each track the likelihood of a muon hypothesis from input from the muon detector.

- The average transverse momentum of the muons in Drell Yan decays is higher than that of background muons as seen in Fig. 3.22(e).
- Finally, background muons from decays in flight have a higher kaon likelihood⁷ value L_K (Fig. 3.22(f)), hence a cut on the maximum kaon likelihood is applied.

Fig. 3.22 shows the dependance of signal and background on the six variables. The signal and background samples in these plots are normalized to an area of one. An optimization of the ratio of signal to background is not the best strategy. Due to the low statistics available and the background subtraction procedure applied to data, a high cut efficiency is preferable over a high purity of the remaining data. For this reasons the significance

$$S = \frac{\text{signal}}{\sqrt{\text{signal} + \text{background}}} \quad (3.16)$$

was chosen as an optimization criterium.

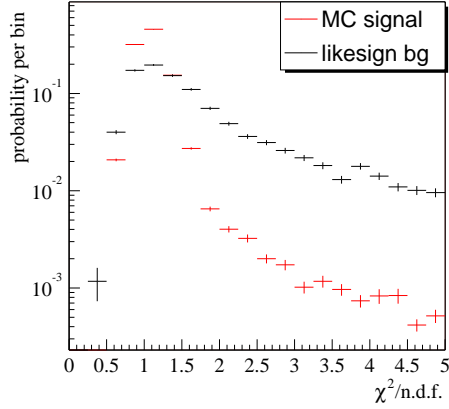
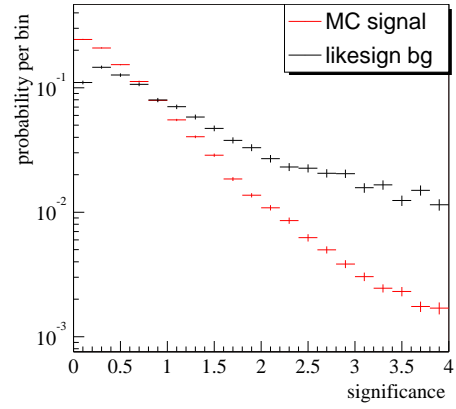
The final choice of cut values is decided on the basis of the distributions shown in Fig. 3.23. In these histograms, the x axis represents the current cut value and the left y axis the number of Drell Yan Monte Carlo signal and simulated opposite sign background events remaining after the cut, normalized to the corresponding number of events with only event based, fiducial and mass range cuts applied. The right y axis represents the value of the significance S depending on the cut. The tightness of the cuts increases in the direction of the arrows.

The six cuts are applied successively in the order of the histograms. Fig 3.23(b) includes the cut chosen from Fig 3.23(a), Fig 3.23(c) includes those chosen from Fig 3.23(a) and 3.23(b), and so on. The chosen cut values are indicated by the dashed lines and are also listed in table 3.4. Events with cut values in the direction of the arrows are accepted by the cut. The values were chosen to maximize the significance S in all six variables.

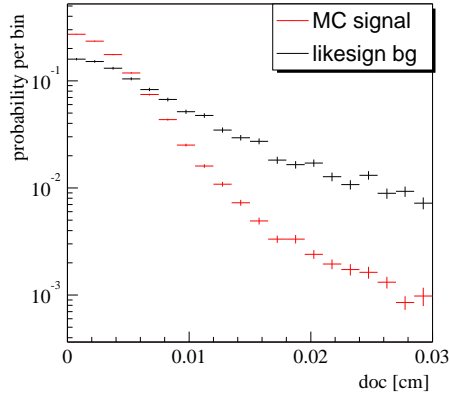
⁷Similar to the muon likelihood, the likelihood of a kaon hypothesis is also provided using data from the RICH.

cut criterium	cut value	efficiency	S/B	S
clone removal	n.a.			
fiducial cuts	n.a.			
mass range	$4\text{GeV} < M_{\mu\mu} < 9 \text{ GeV}$			
hits per track in muon system	> 4	100%	0.22	17.1
track fit χ^2 / ndf	< 1.45	90.8%	0.52	22.2
S_{vv}	< 2.5	88.2%	0.61	23.0
d_{doc}	$< 0.012 \text{ cm}$	86.1%	0.64	23.1
$L_{\mu}(\mu_1) \cdot L_{\mu}(\mu_2)$	> 0.3	79.5%	0.78	23.5
$\max(p_t(\mu_{1,2}))$	$> 1.75 \text{ GeV}$	71.0%	1.62	25.9
$\max(L_K(\mu_{1,2}))$	< 0.8	69.8%	1.92	27.0

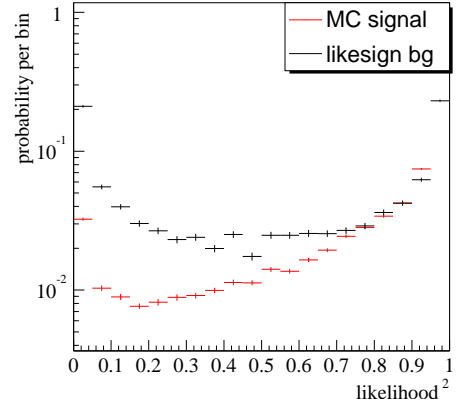
Table 3.4: *Cuts used in muon analysis. Listed are the cut, the chosen value, the amount of signal remaining (efficiency), the signal to background ratio (S/B) and the significance (S) after the cut and all above are applied. Tracks that fail the clone removal, the cut on the number of hits per track in the muon system or the mass cut do not enter the analysis, thus the efficiency is defined to be 100% after these are applied. All cuts were chosen to maximize the significance S.*

(a) Reduced χ^2 

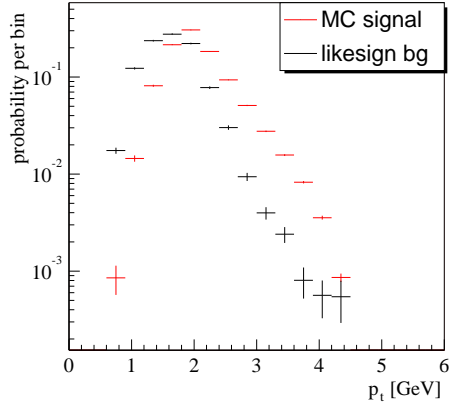
(b) Impact parameter significance



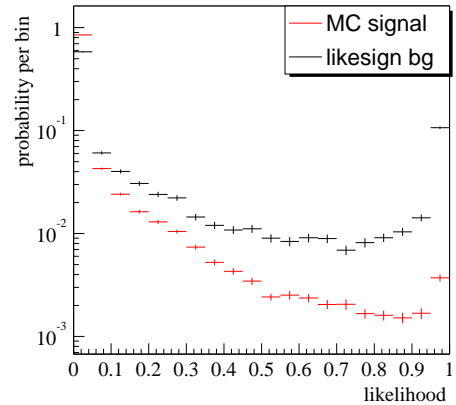
(c) Distance of closest approach of muons



(d) Product of muon likelihoods



(e) Transverse momentum of muon vertex



(f) Kaon likelihood

Figure 3.22: Dependence of signal MC and likesign background on (a) the reduced χ^2 of the muon track fit to the detector hits, (b) the impact parameter significance, (c) the distance of closest approach of the muons, (d) the product of the muon likelihood of the two tracks, (e) the transverse momentum of the reconstructed vertex and (f) the kaon likelihood of the tracks.

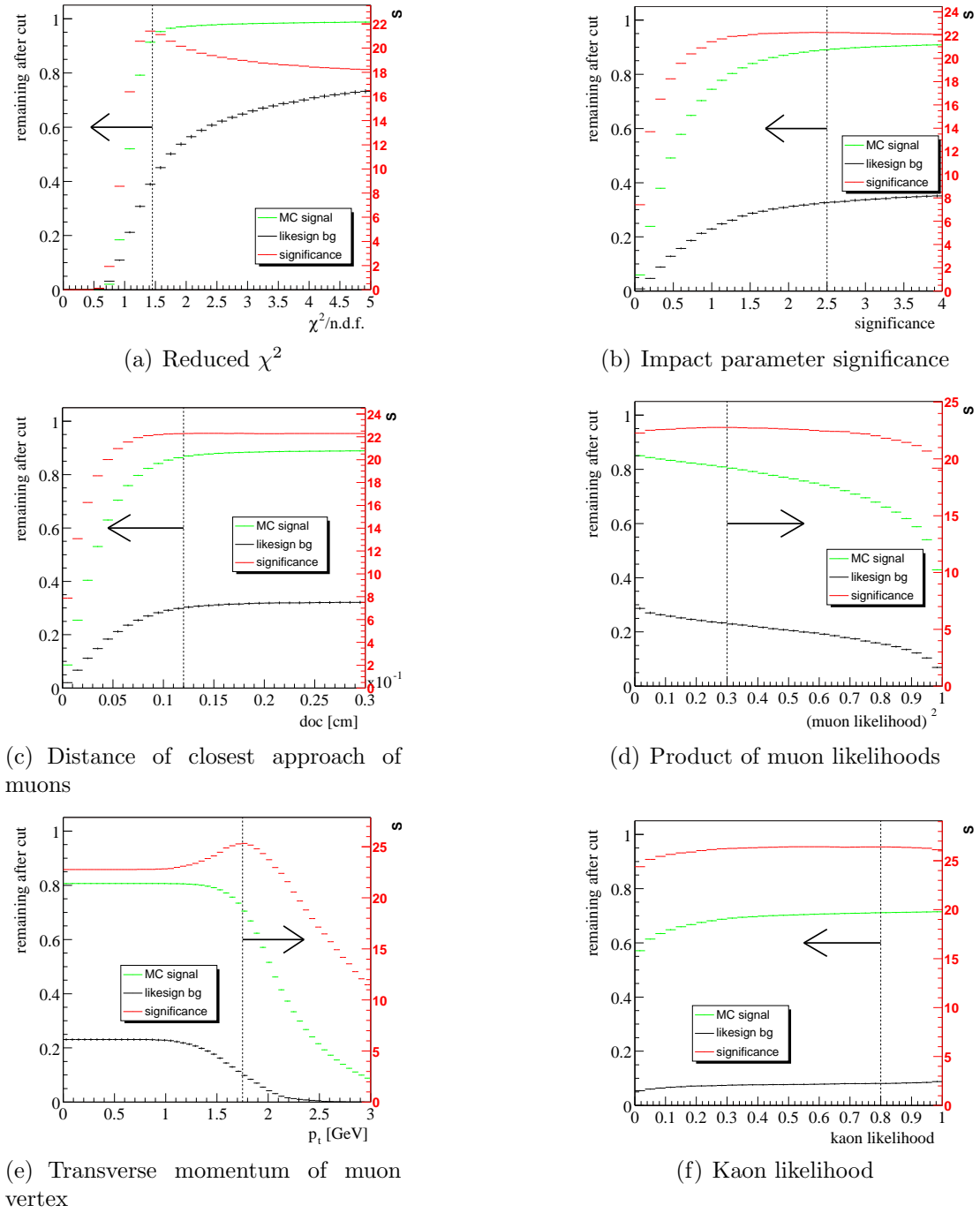


Figure 3.23: Effect of the consecutive cuts on signal and background rates and on the value S , the significance as defined in Eq. (3.16). (a) shows the cut on the reduced χ^2 of the track fit, (b) on the impact parameter significance, (c) on the distance of closest approach of the muons, (d) on the product of the muon likelihoods of the tracks, (e) on the transverse momentum of the reconstructed vertex and (f) on the kaon likelihood of the tracks. The left axis shows the percentage of signal and background events remaining after this and all previous cuts, the right axis corresponds to the optimization value S .

3.5.2 Further Geometrical Cuts

After the definition of the selection criteria they are applied to all data sets and the final Drell Yan Monte Carlo weights can be determined as described in Sec. 3.4. After subtraction of the background, the signal distribution is now compared for the first time to the distributions of accepted Drell Yan Monte Carlo events.

In a first step, geometrical distributions of tracks which are relatively independent of the details of the kinematics are compared in order to verify if data and Monte Carlo are in agreement. Fig. 3.24 shows the x position in the magnet focal plane and in the muon station MU3 of all tracks passing through tracking station PC1 with a y coordinate of $-20.0 \text{ cm} < y < 20.0 \text{ cm}$.

It can be noted that the agreement between data and Monte Carlo is rather poor

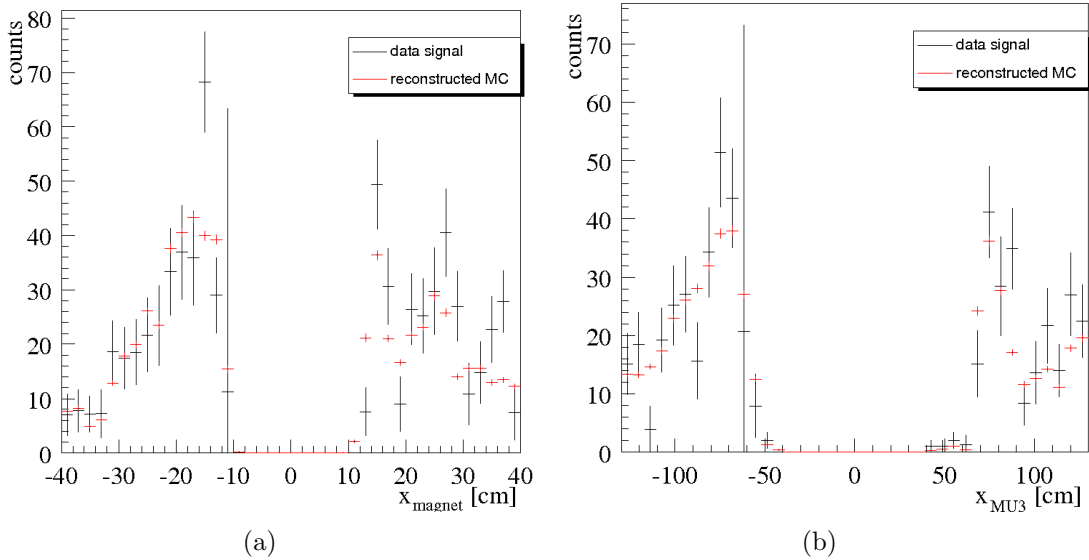


Figure 3.24: x position of tracks passing station PC1 left and right of the insensitive inner region ($-20.0 \text{ cm} < y < 20.0 \text{ cm}$). (a) shows the x coordinate in the magnet focal plane, (b) in the muon station MU3.

in the transition region between Inner and Outer tracker. This is not unexpected. The fiducial cuts introduced at the beginning of the chapter were applied because of discrepancies between simulation and reality in the detector description in this area. Additionally, the Single Track Monte Carlo simulation uses the same detector simulation as the Drell Yan Monte Carlo which introduces an additional bias in the transition region. For these reasons, the fiducial cuts were expanded to include tracks with the coordinates $-14.0 \text{ cm} < x_{\text{mag}} < 14.0 \text{ cm}$ in the magnet focal plane and $-65.0 \text{ cm} < x_{\text{MU3}} < 65.0 \text{ cm}$ at the z position of the muon station MU3. Tracks passing within either one of these regions are also removed. The distributions after the additional geometrical cut can be seen in

Fig. 3.25. The remaining differences can be explained by statistics. A comparison of the distributions gives a $\chi^2/\text{ndf} = 39.4/26$ and a probability of 4.5%.

The data sample remaining after applying all fiducial, kinematic and geometrical

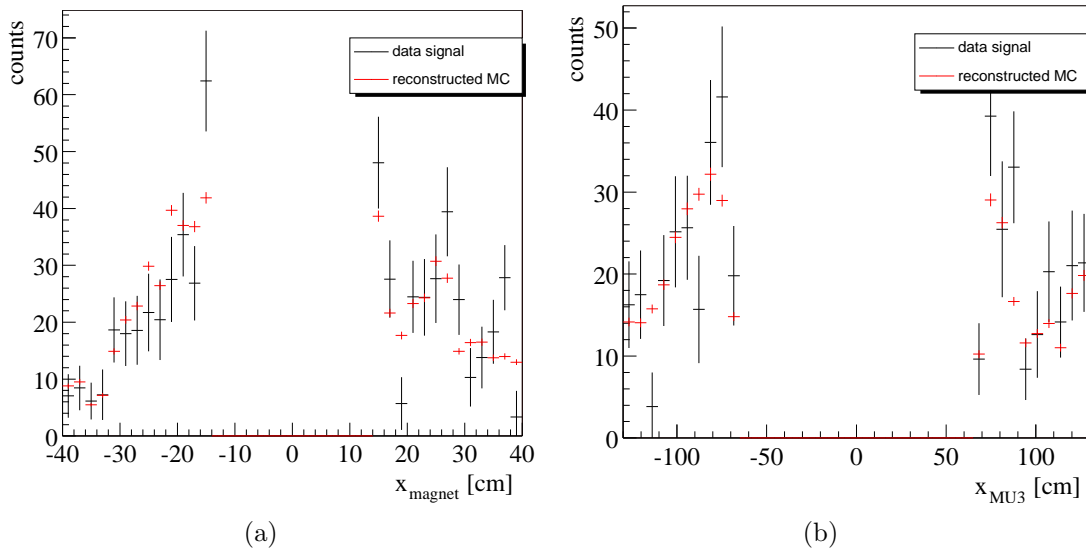


Figure 3.25: x position of tracks passing station $PC1$ left and right of the insensitive inner region ($-20.0 \text{ cm} < y < 20.0 \text{ cm}$). (a) shows the x coordinate in the magnet focal plane, (b) in the muon station $MU3$. A geometrical cut is applied, all tracks passing the magnet focal plane within $-14.0 \text{ cm} < x_{\text{mag}} < 14.0 \text{ cm}$ and the station $MU3$ within $-65.0 \text{ cm} < x_{\text{MU3}} < 65.0 \text{ cm}$ are removed.

cuts consists of 930 ± 30 outbending and 566 ± 24 inbending unlikesign muon pairs. The mass distribution of the unlikesign data after cuts is shown in 3.26. Also included are the likesign distributions with the acceptance reweights from the Single Track Monte Carlo applied. Here a problem is already visible: the bin at a reconstructed invariant mass of 6.1 GeV contains too few unlikesign and too many likesign events compared to the bins to the left and the right. This will be discussed in more detail in Sec. 4.5.

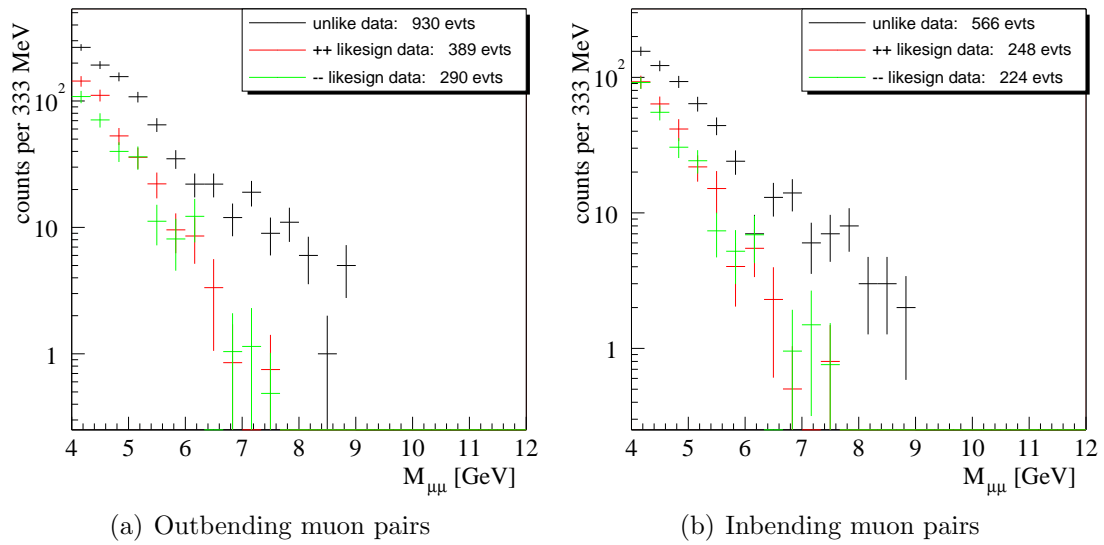


Figure 3.26: Mass distribution of data after cuts and reweighting of likesign background. (a) Outbending and (b) inbending muon pairs, each with correspondingly reweighted likesign pairs. The data has not yet been corrected for detector acceptance and no background subtraction has been applied.

3.5.3 Cut on Event Likelihood

Whereas the first data selection is cutbased, a likelihood based method was also implemented to check if the significance S can be improved. Fig. 3.22 show the dependance of signal and background events as a function of the cut variables i , normalized to unity. The y axis is then proportional to the probability to find a signal or background event with a given value v_i of the plotted variables. For each data event, these probabilities for signal $p_i^{\text{sig}}(v_i)$ and background $p_i^{\text{bg}}(v_i)$ are extracted from the distributions, once for each of the six cut variables. The twelve values are then used to calculate a total event signal likelihood P_{signal} by

$$P_{\text{signal}} = \frac{\prod_i p_i^{\text{sig}}(v_i)}{\prod_i p_i^{\text{sig}}(v_i) + \prod_i p_i^{\text{bg}}(v_i)} \quad (3.17)$$

Instead of applying a hard cut on the six variables this method allows to apply only one cut on the combined variable P_{signal} (3.17).

The distribution of P_{signal} is shown both for Monte Carlo simulated events and

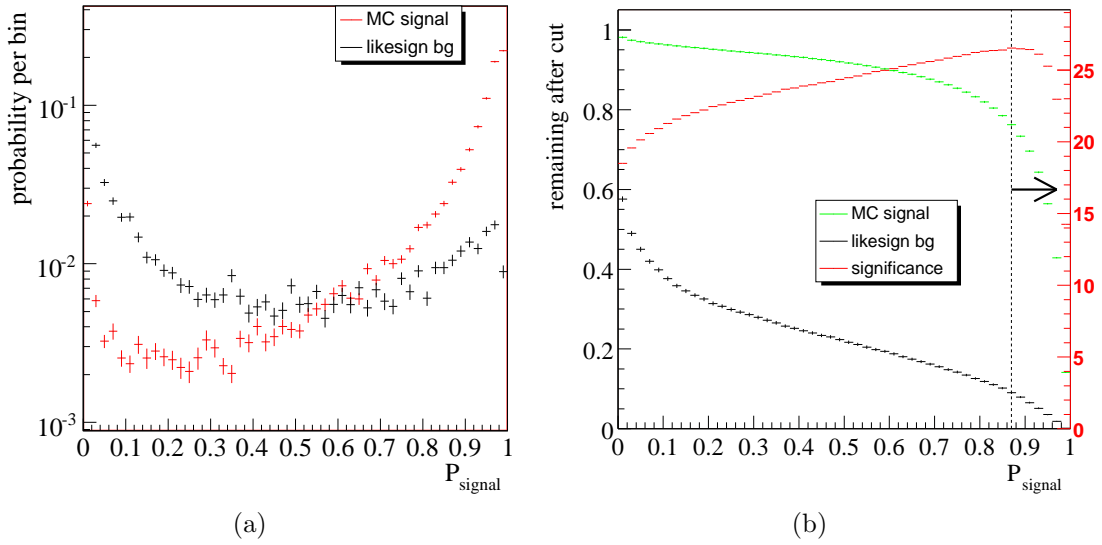


Figure 3.27: *Event likelihood. (a) shows the distribution of likelihood values P_{signal} for Monte Carlo simulated events and simulated opposite sign background. (b) illustrates the effect of a cut on the event likelihood on both Monte Carlo signal and likesign background.*

simulated opposite sign background in Fig. 3.27(a). The signal events have a clear peak at a value of 1, while the background events are distributed evenly across the distribution with a smaller peak around 0. The effect of a cut on P_{signal} on signal and background depending on the chosen value is shown in Fig. 3.27(b). From this distribution, a value of 0.87 was picked, maximizing again the significance S .

76.2% of signal and 9.0% of background survive this cut, leading to a significance of 26.5 and a signal over background ratio of 1.89. Both of these values are slightly lower than those after the cutbased analysis.

The result of this cut is shown in Fig. 3.28(b), compared to the result of the six consecutive cuts. Both results are compatible within errors.

3.5.4 Final Data Sample

After background subtraction according to equation (3.5), a Drell Yan signal of 921 ± 43 events remains using the consecutive cuts method, while the likelihood method results in 911 ± 50 events. The result of both methods is identical within errors. Since the likelihood method does not give a better significance, the cut based method was chosen to derive cross sections. It has the advantage that the effects of the different variables can be seen more easily. The mass distribution after the six kinematic cuts is shown in 3.28(a), the one after a cut on the the signal likelihood in 3.28(b). The dip in the mass distribution at 6.1 GeV, which was already visible in the distributions of opposite sign data shown in Fig. 3.15 before and in Fig 3.26 after cuts, is still present after background subtraction.

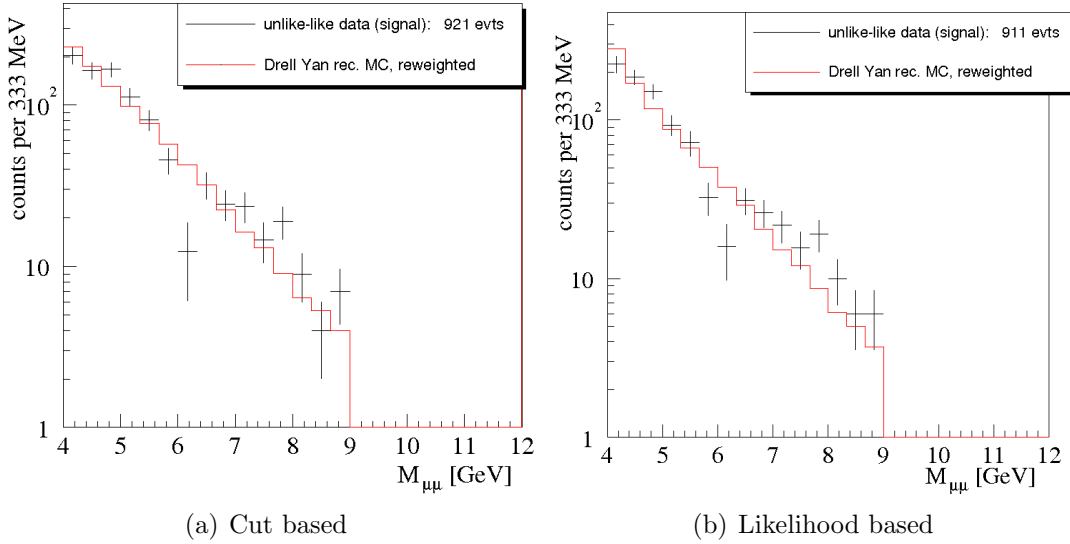


Figure 3.28: *Mass distribution of signal extracted after cuts and background subtraction, not yet corrected for luminosity and acceptance. Histogram (a) shows the data after applying the six consecutive kinematic cuts, histogram (b) after the single cut on P_{signal} (3.17). The results of both analysis methods are consistent.*

3.6 Electron Data

At HERA-b not only muon pairs were observed, a similar sized data sample of electron pairs was also taken. The distribution of the dielectron mass is shown in Fig. 3.29. The data is plotted in the J/ψ and Drell Yan mass region separately for three different selection criteria. Distributions 3.29(a) and 3.29(b) contain the full dataset while 3.29(c) and 3.29(d) show the data that pass a set of preliminary selection criteria. These criteria were chosen to maximize signal over background of the J/ψ peak, since the decay of a J/ψ has a similar experimental signature as the Drell Yan process. They consist of cuts on the value of E/p and the reduced χ^2 of the track fit of both electrons, the significance of the distance between electron vertex and primary vertex S_{vv} , the distance of closest approach of the electrons d_{doc} and the distance between the electron tracks and the corresponding cluster in the electromagnetic calorimeter d_{tc} . Their values are listed in Tab. 3.5. No cut on the transverse momentum of the electrons was applied because the average p_t of electrons coming from a J/ψ is far lower than that of those created by a Drell Yan process.

As easily seen, the amount of likesign data relative to the unlikesign sample is

cut criterium	cut value
clone removal	n.a.
E/p	$0.88 < E/p < 1.18$
track fit χ^2 / ndf	< 2.5
S_{vv}	< 3.0
d_{doc}	< 0.013 cm
d_{tc}	< 2.0 cm

Table 3.5: Preliminary cuts used in the dielectron analysis. Their values were chosen to maximize signal over background of J/ψ , which has the same experimental signature as a Drell Yan event.

much lower than in the dimuon case and almost none of it remains after the loose selection criteria listed above. This is due to the fact that the dielectron trigger asks for at least one positive and one negative electron per event. This is a much more stringent selection compared to the muon trigger and was necessary to keep the trigger rate of electron pairs under control. The few likesign electron events in the data are thus caused by three or more trigger electrons in one event. This makes using the likesign electron data as a background simulation to Drell Yan unusable.

Without a likesign electron pair data sample, the only option to simulate the background that remains is event mixing. After it became obvious that event mixing is unable to simulate the background due to the intrinsic nonconservation of momentum, the analysis of the dielectron data was discontinued.

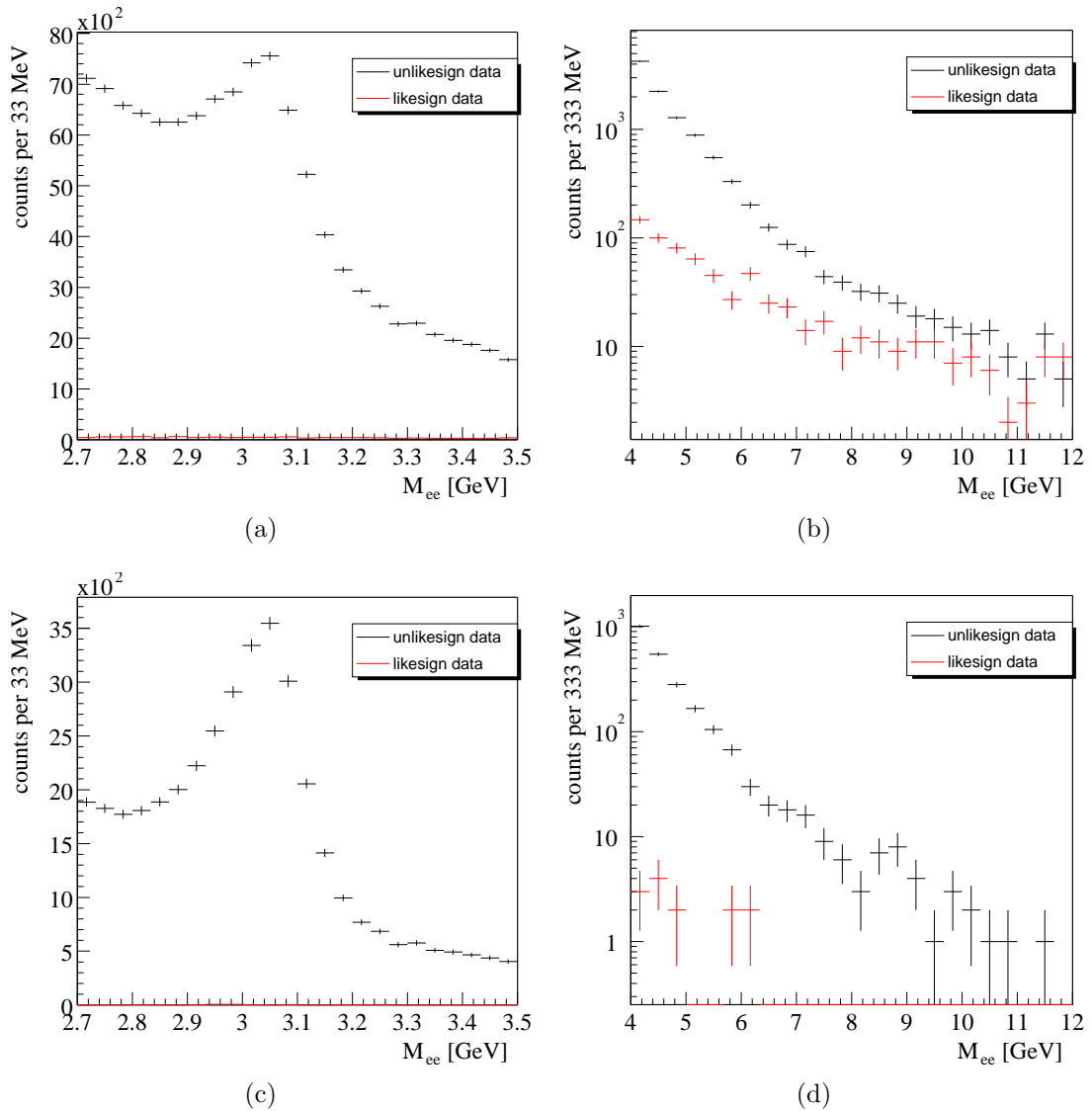


Figure 3.29: *Distribution of the dielectron mass. (a) and (c) show the mass distribution around the J/ψ mass, (b) and (d) the mass range used in the Drell Yan analysis with no cuts or a full set of preliminary cuts applied, respectively. After cuts no likesign data remains.*

Chapter 4

Determination of Cross Sections

In this chapter the measured differential cross sections of the Drell Yan process are presented. Two steps are still necessary to calculate these cross sections. First, the luminosity of the data used in the analysis is determined. Since the luminosity of the lepton triggered runs is not available, it has to be determined indirectly via the yield of a process with a known cross section. As a cross check, the luminosity determined in the first section is also used to calculate the cross section of Υ production, which is compared to the result of a dedicated Υ analysis at HERA-b. Second, the acceptance of the detector is given as a function of several kinematic variables as determined from Drell Yan Monte Carlo.

From the differential cross sections of the Drell Yan process, the nuclear suppression factor α is determined and the parameters of the Lam Tung relation are extracted. Finally, selected results are compared to measurements from the experiments E772 and NA50 and a study of systematic effects is presented.

4.1 Luminosity Determination

At HERA-b, the luminosity is only known for runs which use the minimum bias trigger¹ ([Bru05]). For dilepton triggered runs, the luminosity has to be determined indirectly via a known cross section of a second process. By comparing the number of observed $J/\psi \rightarrow \mu^+ \mu^-$ events $N_{J/\psi}$ in the same data sample that was also used for the Drell Yan analysis to the known J/ψ cross section $\sigma_{J/\psi}$, the luminosity of the triggered data \mathcal{L} can be calculated as:

$$\mathcal{L} = \frac{N_{J/\psi}}{\sigma_{J/\psi} \cdot A^\alpha \cdot Br(J/\psi \rightarrow \mu^+ \mu^-) \cdot \varepsilon_{J/\psi}}, \quad (4.1)$$

¹The minimum bias trigger is a trigger that randomly selects events containing an interaction during datataking, as opposed to the dimuon or dielectron trigger, which requires two muons or electrons to be present in an event.

where A is the mass number of the target nucleus, α the target mass dependence of the cross section, $Br(J/\psi \rightarrow \mu^+\mu^-)$ the branching ratio and $\varepsilon_{J/\psi}$ the detector acceptance for the observed decay $J/\psi \rightarrow \mu^+\mu^-$. Since the data consists of interactions with wires of different materials, the number of events has to be determined separately for each of the wire materials Tungsten, Carbon and Titanium:

$$\mathcal{L}_W = \frac{N_{J/\psi}^W}{\sigma_{J/\psi} \cdot A_W^\alpha \cdot Br(J/\psi \rightarrow \mu^+\mu^-) \cdot \varepsilon_{J/\psi}} \quad (4.2)$$

$$\mathcal{L}_C = \frac{N_{J/\psi}^C}{\sigma_{J/\psi} \cdot A_C^\alpha \cdot Br(J/\psi \rightarrow \mu^+\mu^-) \cdot \varepsilon_{J/\psi}} \quad (4.3)$$

$$\mathcal{L}_{Ti} = \frac{N_{J/\psi}^{Ti}}{\sigma_{J/\psi} \cdot A_{Ti}^\alpha \cdot Br(J/\psi \rightarrow \mu^+\mu^-) \cdot \varepsilon_{J/\psi}} \quad (4.4)$$

To calculate the number of J/ψ events $N_{J/\psi}$, the reconstructed invariant mass distribution of data around the J/ψ mass peak is fitted with a function consisting of three separate parts,

$$f_{J/\psi} = c_0 \cdot f_{\text{gauss}} + c_1 \cdot f_{\text{rad}} + f_{\text{bg}}, \quad (4.5)$$

where f_{gauss} is a double gaussian in which both gauss functions have the same mean μ , a radiation tail f_{rad} ([Spi04]) and a sum of two exponentials as background f_{bg} . A second gauss function is necessary to account for events which suffered from multiple scattering in the detector, see also ([Hus05]), as these events have a lower mass resolution. The radiation tail is caused by the radiative decay $J/\psi \rightarrow \mu^+\mu^-\gamma$. Thus, the formulas for these functions are:

$$\begin{aligned} f_{\text{gauss}} &= \left[(1 - c_2) \cdot \exp\left(-\frac{1}{2} \left(\frac{M - \mu}{\sigma_0}\right)^2\right) + c_2 \cdot \exp\left(-\frac{1}{2} \left(\frac{M - \mu}{\sigma_1}\right)^2\right) \right] \\ f_{\text{rad}} &= \frac{1}{2} \cdot \exp[c_3(M - \mu)] \cdot (M - \mu)^2 \cdot |c_3|^3 \\ f_{\text{bg}} &= \exp[c_4 + c_5 M] + \exp[c_6 + c_7 M] \end{aligned}$$

The signal part of the function is then integrated over the mass range of the J/ψ peak to derive the number of observed J/ψ :

$$N_{J/\psi} = c_0 \int f_{\text{gauss}} dM + c_1 \int f_{\text{rad}} dM \quad (4.6)$$

As already discussed in Sec. 3.4 the transverse momentum of the J/ψ is not simulated properly. Thus, the J/ψ Monte Carlo simulation suffers from the same problem as the Drell Yan Monte Carlo simulation. The discrepancy between data and simulation can be seen in 4.1. As the transverse momentum is not directly used in the luminosity determination, a bin by bin correction was applied to reweight the simulation to match the data distribution. After the reweighting,

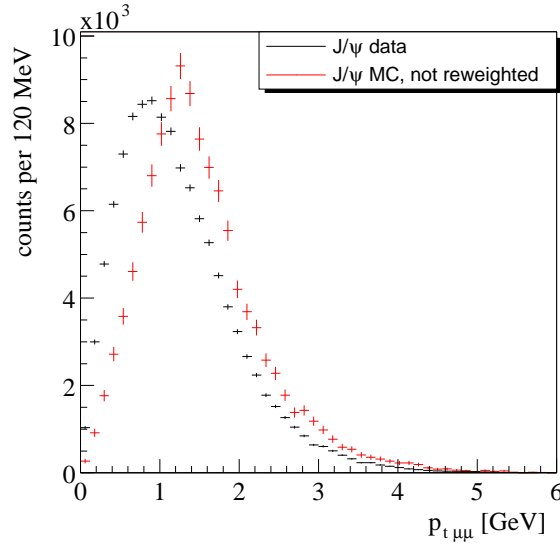


Figure 4.1: *Distribution of the transverse momentum of the J/ψ in data and in the Monte Carlo simulation before reweighting.*

the reconstructed and generated J/ψ Monte Carlo can be used to calculate the acceptance for $J/\psi \rightarrow \mu^+\mu^-$, $\varepsilon_{J/\psi}$.

To improve the signal to noise of the J/ψ peak, a loose set of cuts is applied before fitting the signal peak in the invariant mass distribution. These are given in Tab. 4.1.

The result of these cuts can be seen in Fig. 4.2(a) to 4.2(c), separated according to the material of the target wire. Also shown in each plot is the total fit function and separately the radiation tail and background components of the fit. The results of the fits are given in Tab. 4.2, together with the other variables used in the luminosity calculation. This leads to a total luminosity of the data used in the Drell Yan analysis of:

$$\mathcal{L}_W = (1320 \pm 140) \text{ nb}^{-1} \quad (4.7)$$

$$\mathcal{L}_C = (32000 \pm 3000) \text{ nb}^{-1} \quad (4.8)$$

$$\mathcal{L}_{Ti} = (36 \pm 5) \text{ nb}^{-1} \quad (4.9)$$

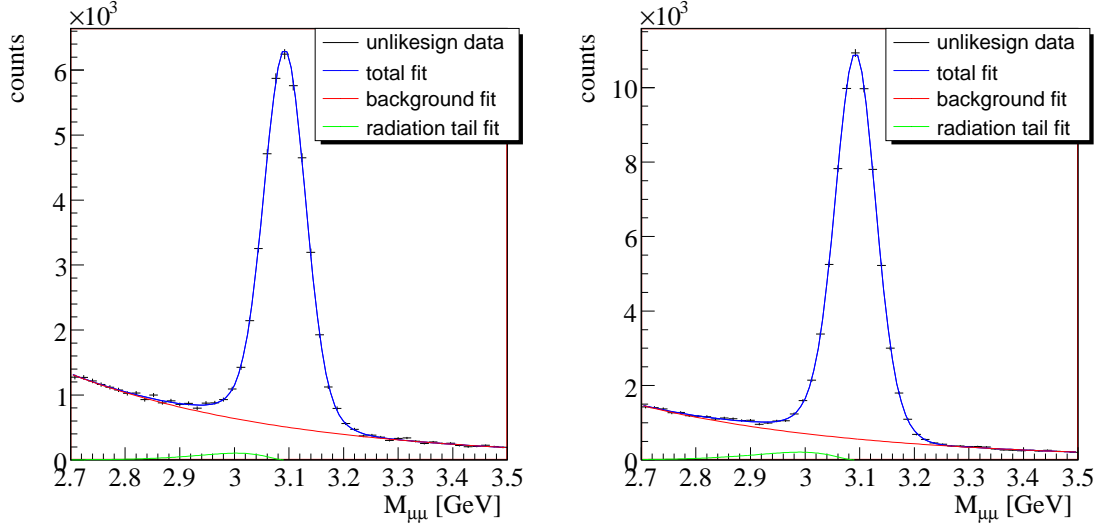
The error on the luminosity is dominated by the uncertainty of the J/ψ cross section of roughly 10%. Studies on the systematical effect of the kinematic selection given in Tab. 4.1 and the shape of the fit function 4.5 on the total error have shown that their influence is smaller than the statistical error of $N_{J/\psi}$, which is about 1%. The systematic error is thus negligible in comparison to the error on the J/ψ cross section and the total error of the luminosity.

cut criterium	cut value
clone removal	n.a.
fiducial cuts	n.a.
hits per track in muon system	> 4
track fit χ^2 / ndf	< 2.5
S_{vv}	< 3.0
d_{doc}	< 0.02 cm
$L_{\mu}(\mu_1) \cdot L_{\mu}(\mu_2)$	> 0.2
$\max(L_{\text{K}}(\mu_{1,2}))$	< 0.99

Table 4.1: Cuts used in J/ψ selection. The selection variables are the same as those listed in Tab. 3.4 and explained in Sec. 3.5.

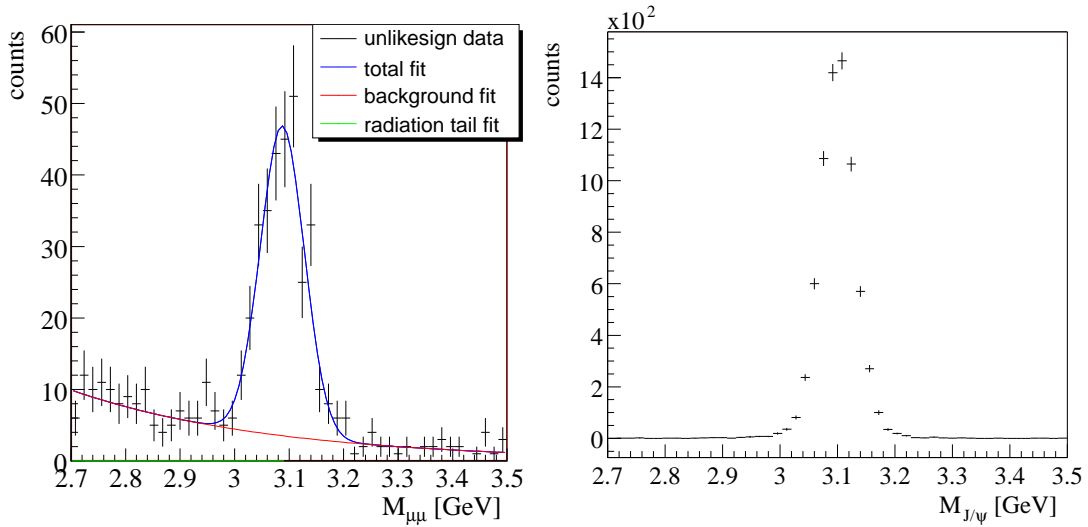
	Tungsten	Carbon	Titanium
$N_{J/\psi}$	36771 ± 509	65095 ± 586	273 ± 26
A	183.84	12.0107	47.867
$\sigma_{J/\psi}$ ([Bar05])	501 ± 44 nb/nucleon		
α ([Lei00])	0.96 ± 0.01		
$Br(J/\psi \rightarrow \mu^+ \mu^-)$ ([Pdg06])	0.0593 ± 0.0006		
$\varepsilon_{J/\psi}$	$0.732 \% \pm 0.008 \%$		

Table 4.2: Values used in luminosity calculation.



(a) Mass distribution from Tungsten target

(b) Mass distribution from Carbon target



(c) Mass distribution from Titanium target

(d) Reconstructed J/ψ Monte Carlo

Figure 4.2: *Invariant mass distribution of the reconstructed muon pair at the J/ψ mass. (a) shows the distribution of unlikesign data from the Tungsten wire including a fit to the J/ψ peak, (b) from Carbon and (c) from a Titanium target wire. (d) shows the distribution of a reconstructed J/ψ Monte Carlo simulation. The fits to the data distributions are according to Eqn. (4.5).*

4.2 $\Upsilon(1S)$ Cross Section

During the event selection (Sec. 3.5), a cut on the invariant mass of the muon pair of $4 \text{ GeV} < M_{\mu\mu} < 9 \text{ GeV}$ was applied to remove muon pairs generated by decays of J/ψ and Υ . Fig. 4.3(a) shows the invariant mass distribution above 8.6 GeV without this cut. A clear $\Upsilon(1S)$ signal can be seen. With the $\Upsilon(1S)$ Monte Carlo simulation shown in Fig. 4.3(b) and the luminosity calculated in Sec. 4.1 it is possible to determine the cross section, which is calculated as follows:

$$\sigma_{\Upsilon} = \frac{N_{\Upsilon}}{\mathcal{L} \cdot A^{\alpha} \cdot Br(\Upsilon \rightarrow \mu^+\mu^-) \cdot \varepsilon_{\Upsilon}}, \quad (4.10)$$

where $Br(\Upsilon \rightarrow \mu^+\mu^-)$ is the branching ratio of the decay into two muons, N_{Υ} is the number of Υ events seen, A is the mass number of the target nuclei, α the target mass dependance of the cross section and ε_{Υ} the detector efficiency which is calculated from the reconstructed and the generated Υ Monte Carlo simulation.

The mass distribution was fitted between 8 and 11 GeV with three gaussians and

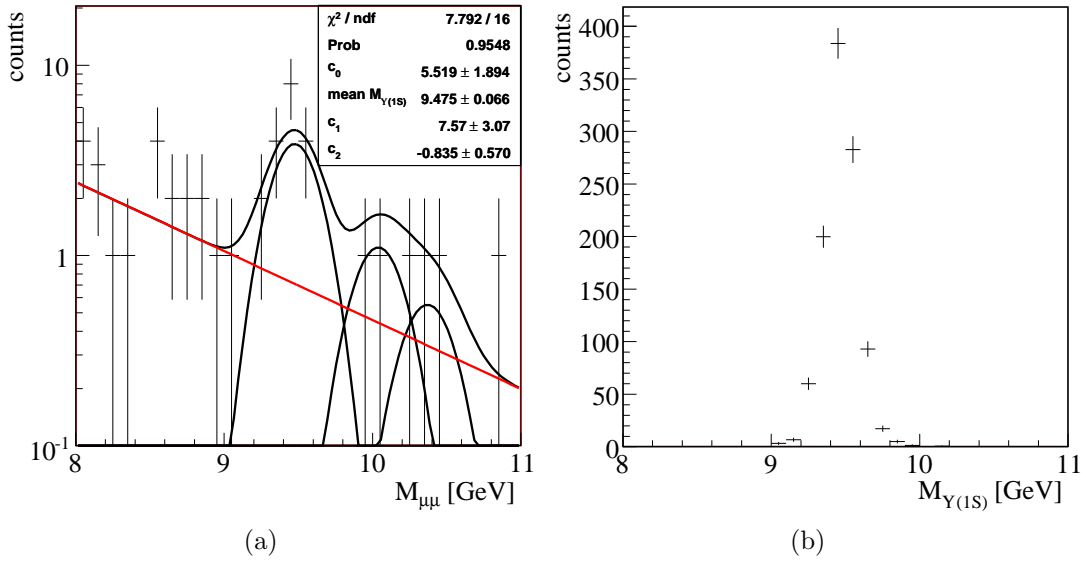


Figure 4.3: Invariant mass distribution of the reconstructed muon pair above 8.6 GeV. (a) shows the distribution of unlikesign data and a fit (4.12), (b) shows the distribution of a reconstructed $\Upsilon(1S)$ Monte Carlo simulation.

an exponential distribution. The mean values of the two higher mass gauss peaks were fixed with respect to the lower gauss peak according to the mass values of the Υ states (1S), (2S) and (3S) as given in [Pdg06]. Their relative size was also fixed according to results from E605 ([Mor91]):

$$N(1S) : N(2S) : N(3S) = (70 \pm 3) : (20 \pm 2) : (10 \pm 1) \quad (4.11)$$

The width of the gauss distributions is also fixed. For the first peak corresponding to the (1S) state it is set to $159 \text{ MeV}/c^2$, the expected muon momentum resolution gained by extrapolating from the resolution measured in J/ψ decays ([Abt06]); for the two peaks corresponding to the higher mass states (2S) and (3S) the widths are scaled up proportional to their mass as given in [Pdg06]. The fit function is then given by:

$$N(M_\Upsilon) = c_0 \left[0.7 \cdot \exp \left(-\frac{1}{2} \frac{(M_{\mu\mu} - M_{\Upsilon(1S)})^2}{(159 \text{ MeV}/c^2)^2} \right) + 0.2 \cdot \exp \left(-\frac{1}{2} \frac{(M_{\mu\mu} - M_{\Upsilon(2S)})^2}{(168 \text{ MeV}/c^2)^2} \right) + 0.1 \cdot \exp \left(-\frac{1}{2} \frac{(M_{\mu\mu} - M_{\Upsilon(3S)})^2}{(174 \text{ MeV}/c^2)^2} \right) \right] + \exp(c_2 + c_3 \cdot M_{\Upsilon(2S)}) \quad (4.12)$$

The mass of the $\Upsilon(1S)$ M_Υ , the overall number of Υ c_0 and the two parameters of the exponential background, c_1 and c_2 , are the four free parameters.

The fit shown in Fig. 4.3(a) returns $N_{\Upsilon(1S)} = 15.4 \pm 5.3$, $N_{\Upsilon(2S)} = 4.6 \pm 1.6$ and $N_{\Upsilon(3S)} = 2.4 \pm 0.8$ events. As the mass of the $\Upsilon(1S)$ state, a value of $9.47 \pm 0.07 \text{ GeV}$ is determined. This agrees well with the PDG value of $9.46030 \pm 0.00026 \text{ GeV}$.

Inserting the total number of Υ , $N_\Upsilon = 22.4 \pm 5.6$, the luminosity (4.7) and the Υ detector efficiency $\varepsilon_\Upsilon = 0.74 \pm 0.02\%$ into (4.10) yields:

$$\sigma_\Upsilon = 225 \pm 64 \text{ pb/nucleon} \quad (4.13)$$

at a center-of-mass energy of $\sqrt{s} = 41.6 \text{ GeV}$ and within the acceptance of HERA-b of $-0.45 < x_F < 0.05$. A dedicated analysis searching for Υ at HERA-b ([Abt06]) published an $\Upsilon \rightarrow \mu^+\mu^-$ cross section of

$$Br(\Upsilon \rightarrow \mu^+\mu^-) \cdot \frac{d\sigma}{dy}|_{y=0}(\Upsilon) = \frac{N_\Upsilon}{\mathcal{L} \cdot A^\alpha \cdot \varepsilon_\Upsilon} \cdot \frac{1}{\Delta_{y_{\text{eff}}}} = 4.0 \pm 1.0 \frac{\text{pb}}{\text{nucleon}}, \quad (4.14)$$

	$\Upsilon(1S)$	$\Upsilon(1S)$	$\Upsilon(1S)$
N	15.4 ± 5.3	4.6 ± 1.6	2.4 ± 0.8
$N(\Upsilon)$	22.4 ± 5.6		
ε_Υ	$0.74\% \pm 0.02\%$		
$\Delta_{y_{\text{eff}}}$	$1.14 \pm 0.12_{\text{stat}}$		
$\mathcal{L} \cdot A^\alpha$	$546 \pm 381/\text{pb}$		
$Br(\Upsilon \rightarrow \mu^+\mu^-)$ ([Pdg06])	$2.48 \pm 0.05\%$		

Table 4.3: Values used in the determination of the Υ cross section.

where $\Delta_{y_{\text{eff}}} = 1.14 \pm 0.12_{\text{sys}}$ is a factor connecting full and differential cross sections at mid rapidity. Calculating the same value using the measurement from above results in:

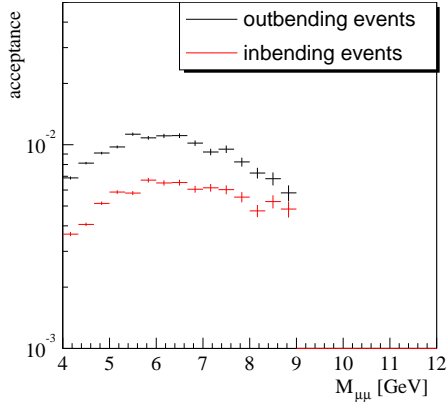
$$Br(\Upsilon \rightarrow \mu^+ \mu^-) \cdot \left. \frac{d\sigma}{dy} \right|_{y=0}(\Upsilon) = (4.9 \pm 1.4) \frac{\text{pb}}{\text{nucleon}}, \quad (4.15)$$

which is in good agreement with the value published in [Abt06].

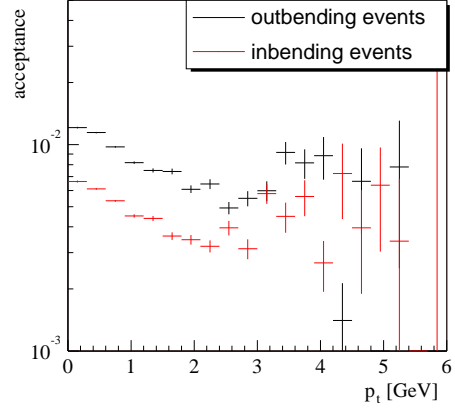
4.3 Detector Acceptances

The detector acceptance as a function of kinematic variables is calculated from generated and reconstructed Drell Yan Monte Carlo events. The kinematic selection chosen in Sec. 3.5 is applied to the reconstructed Drell Yan Monte Carlo dataset for this calculation. Fig. 4.4 shows these acceptances as a function of the reconstructed mass (4.4(a)), the transverse momentum (4.4(b)), the Feynman $x_F = 2p_z/\sqrt{s}$ (4.4(c)) and the pseudorapidity $\eta = -\ln[\tan(\frac{\theta}{2})]$ (4.4(d)) of the muon pair for outbending and inbending muon pairs. In Fig. 4.4(e) and 4.4(f), the acceptance is plotted as a function of $\cos(\theta_{CS})$ and ϕ_{CS} of the positive muon. The index CS here implies that the angles are calculated in the Collins Soper ([Col77]) frame (see Sec. 2.3 for a definition of the Collins Soper frame).

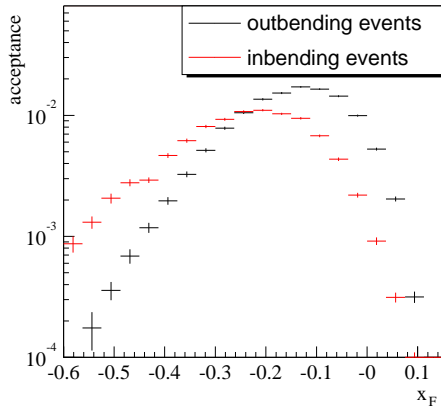
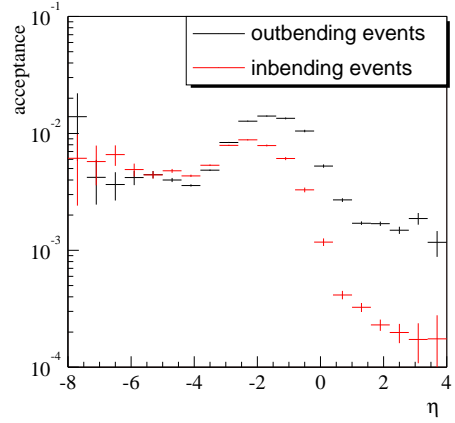
As expected from the effects of the charge combination of the muon tracks explained in Fig. 3.8, the acceptance of outbending muon pairs is larger than that of inbending ones. While the acceptance is relatively flat in the reconstructed mass and transverse momentum of the muon pair, the other distributions show a significant dependence on their kinematic variances. In x_F , the detector limits the detectable range to $-0.45 < x_F < 0.05$, with outbending muon pairs having a slightly more positive average x_F value than inbending muon pairs. The difference between out- and inbending muon pairs is especially pronounced in Fig. 4.4(f) showing dependence of acceptance on the ϕ_{CS} of the positive muon. Outbending muon pairs are only detected if the positive muon has a $|\phi_{CS}| < 1.8$. For inbending muon pairs, the requirement on ϕ_{CS} is just the opposite: $|\phi_{CS}| > 1.2$.



(a) Mass of muon pair



(b) Transverse momentum of muon pair

(c) Feynman x (x_F) of muon pair

(d) Pseudorapidity of muon pair

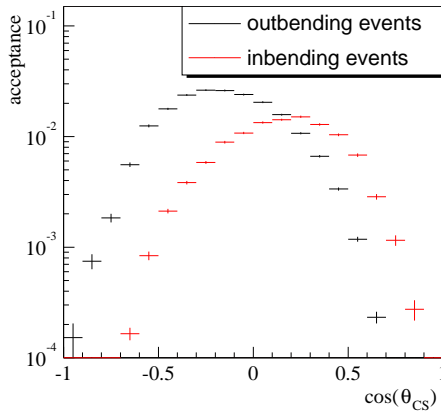
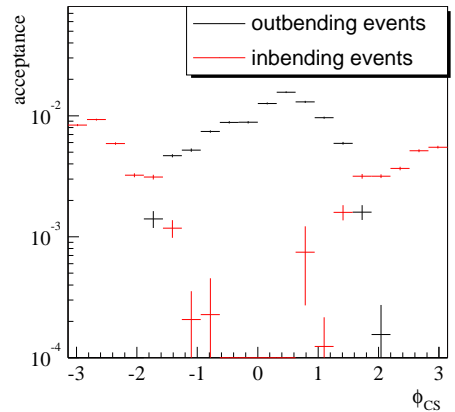
(e) $\cos \theta_{CS}$ of positive muon(f) ϕ_{CS} of positive muon

Figure 4.4: Detector acceptance as a function of reconstructed mass (a), transverse momentum (b), x_F (c) and pseudorapidity η (d) of the muon pair. (e) and (f) show the acceptance as depending on $\cos(\theta_{CS})$ and ϕ_{CS} of the positive muon. All distributions were calculated by dividing distributions from reconstructed DYMC by those from generated DYMC.

4.4 Acceptance corrected Kinematic Distributions

Using the luminosity calculated in Sec. 4.1 and the detector acceptance distributions from Sec. 4.3 it is now possible to calculate differential cross sections. At other experiments, it is usually assumed that the Drell Yan cross section depends linearly on the mass number of the target material. [Ale06] published a value of $\alpha = 0.98 \pm 0.02$. Fig 4.5(a) and Fig 4.5(b) show the distribution of data, corrected for acceptance and luminosity as a function of the transverse momentum of the muon pair, separated for the two target materials Tungsten and Carbon. No corrections for target material have been applied yet. Fig 4.5(c) shows a ratio of the two distributions, with a constant function fitted to the ratio. Using the mass numbers of Tungsten and Carbon, one can calculate the A dependance of the Drell Yan cross section from this constant fit: $\alpha = 1.03 \pm 0.03$, which is also compatible with 1.

For the calculations of the Drell Yan differential cross sections a value of $\alpha = 1$ is used. Four differential cross sections are shown in Fig. 4.6, as a function of invariant mass (4.6(a)), the square of the transverse momentum (4.6(b)), x_F (4.6(c)) and the pseudorapidity of the muon pair from the Drell Yan process. The mass distribution again shows a deficit around 6.2 GeV, which will be examined in the next section. The differential cross section $\frac{d\sigma}{dM_{\mu\mu}}$ as shown in Fig. 4.6(a) is fitted with the phenomenological function:

$$\frac{d\sigma}{dM_{\mu\mu}} \propto M_{\mu\mu}^{-c}. \quad (4.16)$$

This function was derived from the distribution of the dimuon mass in generated Drell Yan Monte Carlo. The fit value for the exponent c is $c = 5.52 \pm 0.31$. The low probability of the fit is caused by the bin at 6.2 GeV. Excluding this bin from the fit yields a value of $c = 5.18 \pm 0.26$ with a reduced χ^2 of 13.2/12 and a fit probability of 35%.

Fig. 4.6(b) shows the differential Drell Yan cross section as a function of p_t^2 of the muon pair. The fit is an exponential function. No significant deviation from an exponential decrease is visible.

The x_F distribution (Fig. 4.6(c)) is fitted with the empirical function

$$\frac{d\sigma}{dx_F} \propto (1 - |x_F - x_0|)^C, \quad (4.17)$$

which gives a value of $C = 4.18 \pm 0.47$ for the exponent. The mean of the distribution is compatible with zero at $x_0 = -0.0002 \pm 0.0228$. This is the first measurement of the differential Drell Yan cross section in the negative x_F range. The shape of the distribution is as expected. A more detailed comparison to measurements from the experiment E772 at Fermilab will follow in Sec. 4.7.1.

The total cross section measured in the the mass range of 4 GeV to 9 GeV at a center-of-mass energy of $\sqrt{s} = 41.6$ GeV and within the x_F range seen at HERA-b of $-0.45 < x_F < 0.05$ is gained by integrating over the x_F distribution:

$$\sigma_{\text{DY}_{x_F} \rightarrow \mu\mu} = (172 \pm 10) \text{ pb/nucleon.} \quad (4.18)$$

The cross section over the full range of x_f can be calculated by integrating the function (4.17). The result is

$$\sigma_{\text{DY} \rightarrow \mu\mu} = (289 \pm 35) \text{ pb/nucleon.} \quad (4.19)$$

The differential cross section $d\sigma/d\eta$ as seen in Fig. 4.6(d) shows a flat behavior at small values of the pseudorapidity and a sharp drop between -2 and -4 . The corresponding behavior in the positive range cannot be seen as it is just outside the acceptance of HERA-b.

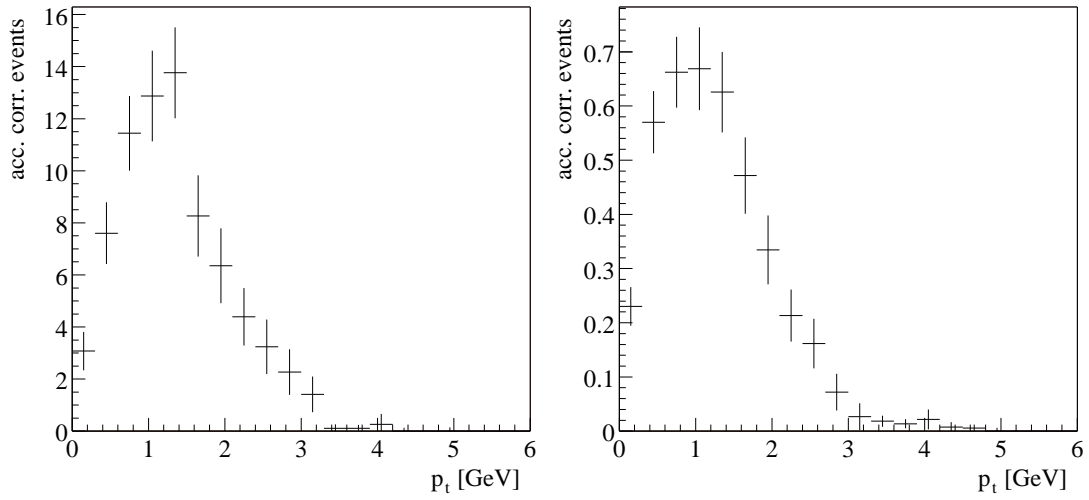
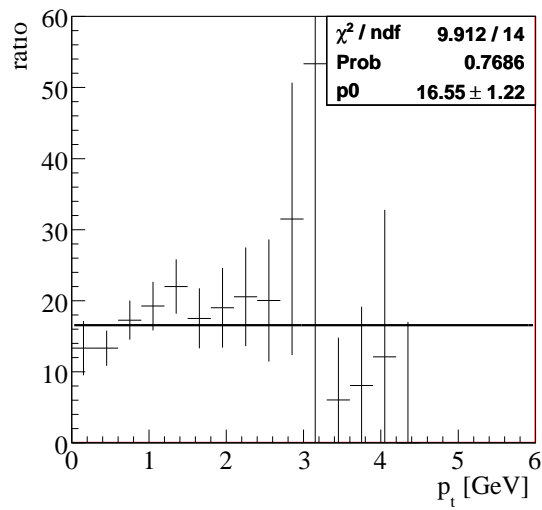
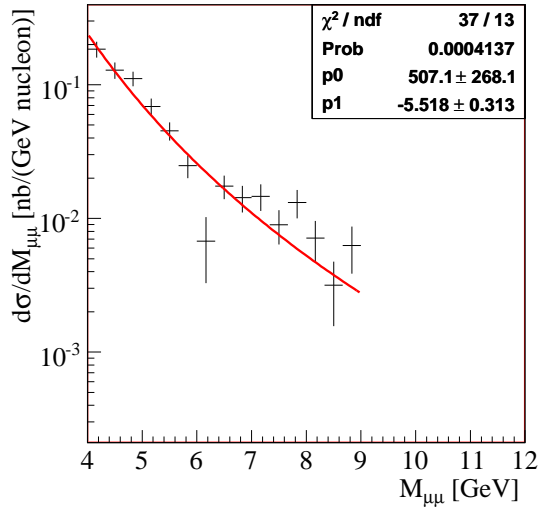
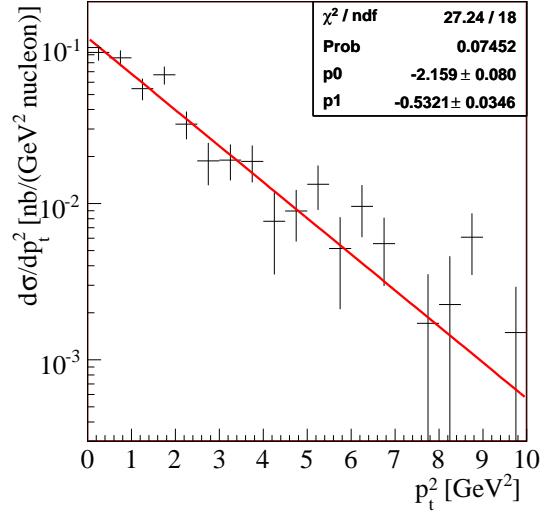
(a) p_t of muon pairs from Tungsten wire(b) p_t of muon pairs from Carbon wire(c) Ratio of p_t distributions

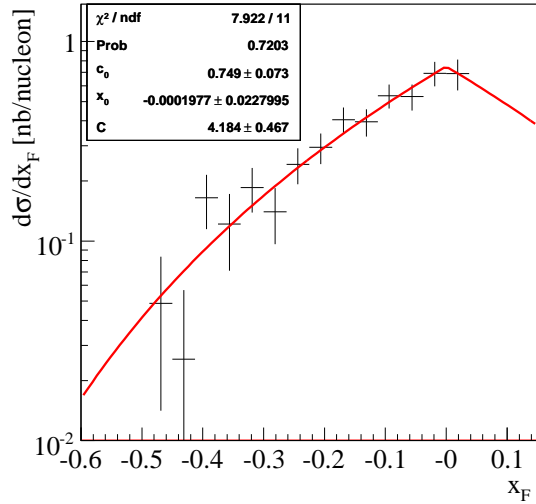
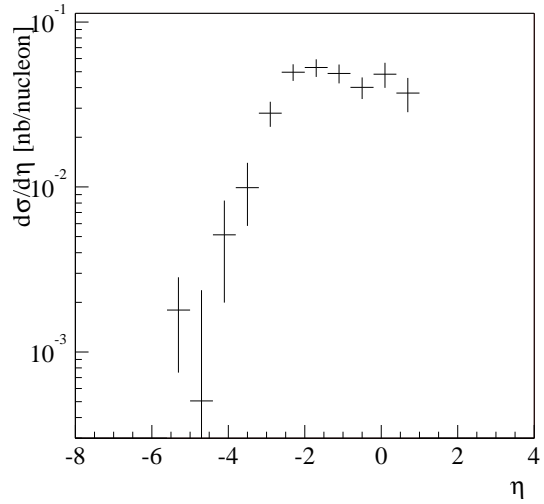
Figure 4.5: (a + b): Acceptance corrected p_t distributions of data, separated according to target material. (c): Ratio of distributions (a) and (b), fitted with a constant function.



(a) Mass of muon pair



(b) Squared transverse momentum of muon pair

(c) Feynman x (x_F) of muon pair

(d) Pseudorapidity of muon pair

Figure 4.6: Differential cross sections of Drell Yan depending on the reconstructed mass (a), the square of the transverse momentum (b), the Feynman x (x_F) (c) and the pseudorapidity (d) of the muon pair.

4.5 Systematic Checks of the Mass Distribution

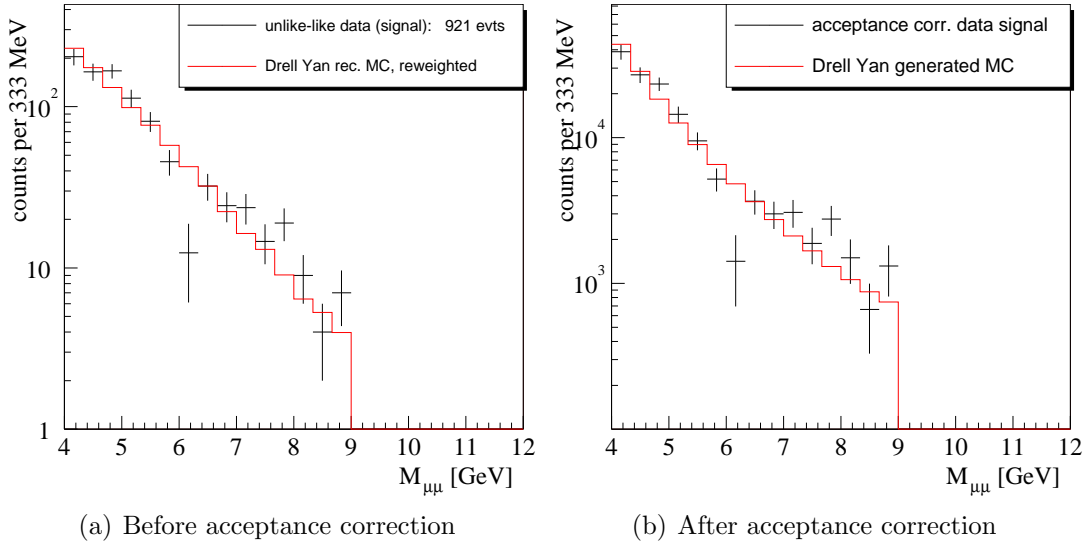


Figure 4.7: Mass distribution (a) of data after background subtraction and reconstructed MC, (b) of acceptance corrected data and generated Drell Yan Monte Carlo. The “dip” in the distribution around 6.2 GeV is evident in both plots.

As already seen in Fig. 3.28 in the last chapter and again in greater detail in Fig. 4.7 and 4.8, the measured Drell Yan signal differs from the Monte Carlo signal in the mass region between 6.1 and 6.3 GeV. This difference remains after acceptance corrections (Fig. 4.6(a)) when compared to generated Drell Yan Monte Carlo distribution.

A χ^2 test to determine if the discrepancy between data and Drell Yan Monte Carlo simulation can be explained by a statistical fluctuation returns a $\chi^2/\text{ndf} = 41.0/15$ and a probability of 0.03%. Excluding the bin at 6.2 GeV in Fig. 3.28, the test gives a $\chi^2/\text{ndf} = 18.4/14$ and a probability of 18.9%. A statistical fluctuation is unlikely to be the explanation.

Also, the effect of the chosen kinematic and fiducial cuts was examined to further exclude a problem with the analysis. No change in cuts was able to remove the discrepancy, though it is less apparent with softer cuts. Since the data deficit is already present before the background subtraction in unlikesign data (see Fig. 3.26), the reweighting applied on the likesign background cannot be the reason.

A similar effect was already seen in the reconstructed muon pair mass distribution published in ([Abt06]). This distribution is shown in Fig. 4.9. The “dip”, which is marked by the red circle, is less pronounced here as the cuts used in the Υ analysis are less stringent than the ones used in the search for Drell Yan. The

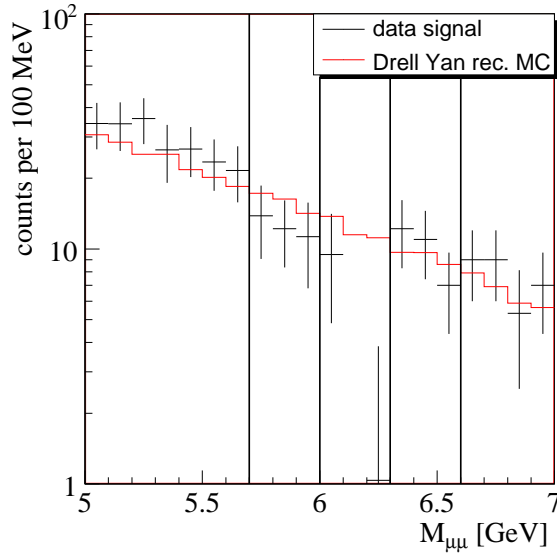


Figure 4.8: Zoomed mass distribution of reconstructed Drell Yan Monte Carlo and data after background subtraction. The vertical lines indicate the three regions of which $x - y$ muon track distributions in the magnet focal plane and in station MU3 are plotted separately in Fig. 4.10 and 4.11.

fact that this discrepancy is seen in two independent analyses points to a detector inefficiency not included in the Monte Carlo simulation.

To check if a detector inefficiency missing in the simulation is the reason, the positions of muon tracks in the detector are examined. For this events with an invariant muon pair mass in the affected region and in regions slightly below and slightly above it were plotted separately both for data and for Drell Yan Monte Carlo simulated events. The three mass regions are indicated by vertical lines in Fig. 4.8. Fig. 4.10 shows the position of tracks coming from muon pairs with invariant masses below ($5.7 \text{ GeV} < M_{\mu\mu} < 6.0 \text{ GeV}$), in ($6.0 \text{ GeV} < M_{\mu\mu} < 6.3 \text{ GeV}$) and above ($6.3 \text{ GeV} < M_{\mu\mu} < 6.6 \text{ GeV}$) the problematic mass region at the magnet focal plane. Fig. 4.11 shows the track position in the station MU3 for the same mass regions. All distributions are plotted separately for in- and outbending muon pairs.

This method suffers from the low statistics, especially in the problematic region for the data. The data distributions have too few entries to be able to find problematic detector regions. Some differences are visible in the distributions of Drell Yan Monte Carlo simulated data. In the distributions showing the $x - y$ position of tracks at the station MU3, one can see that below (Fig. 4.11(d)) and above (Fig. 4.11(f)) the problematic mass region, tracks are distributed evenly to the left and the right of the Inner Tracker area, while in the problematic mass region (Fig. 4.11(e)), there are more tracks on the left side of the detector. Also,

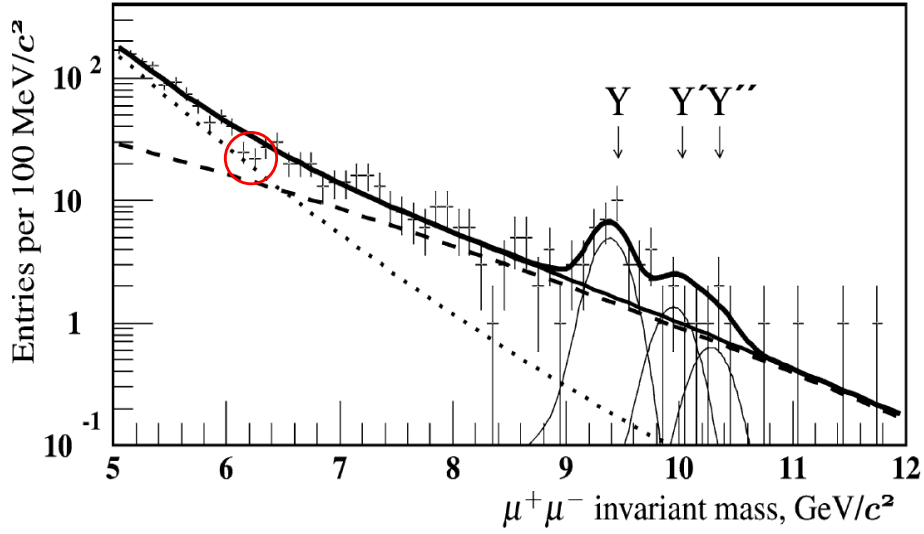
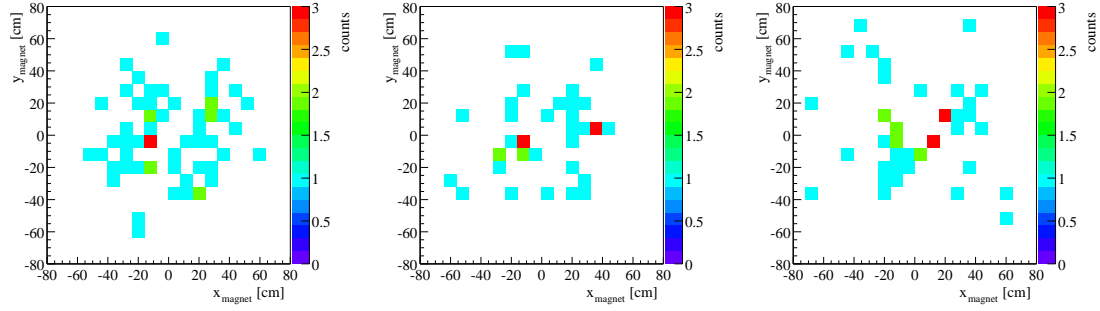


Figure 4.9: *Distribution of reconstructed invariant mass of muon pairs as published in [Abt06]. The red circle marks the “dip” in the mass range of 6.1 to 6.3 GeV. Since the cuts used in the Υ analysis are less strict than those used in this analysis, the discrepancy between data and Monte Carlo is less pronounced. The plot also shows the combinatorial background (dotted line) and Drell Yan (dashed line) in addition to a fit to the Υ signal.*

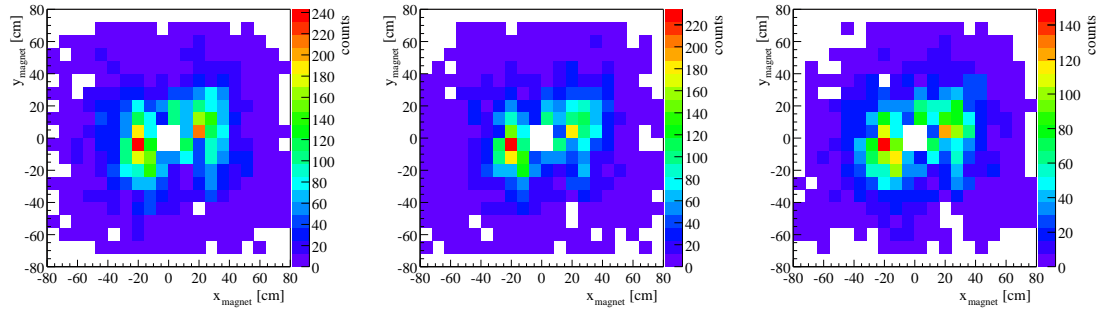
in this middle mass bin, the tracks are concentrated in a smaller area than in the bins above and below.

In the inbending muon pair distributions at station MU3 (Fig. 4.11), the situation is reversed. Both Fig. 4.11(j) and 4.11(l) show more tracks on the left detector side, while Fig. 4.11(k) shows a more even distribution. Considering that the data distributions before background subtraction (see Fig. 3.26) show a larger “dip” in the inbending distributions, this might be the cause. On the other hand, the distributions showing track positions at the magnet focal plane (Fig. 4.10) show no visible differences.

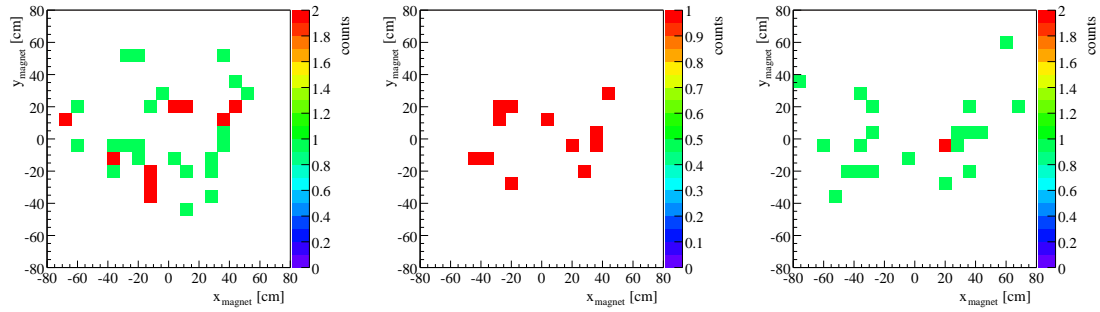
While there are differences in the distribution of tracks in the three mass regions, no significant differences that would explain the missing events can be seen, the cause remains unknown.



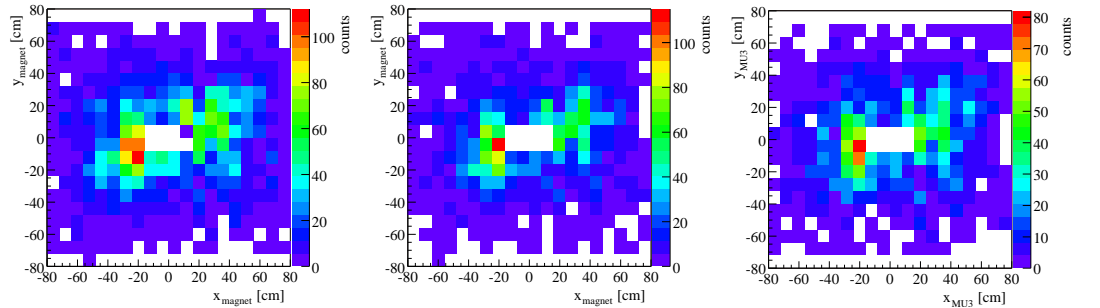
(a) $5.7\text{GeV} < M_{\mu\mu} < 6.0\text{GeV}$, outbending (b) $6.0\text{GeV} < M_{\mu\mu} < 6.3\text{GeV}$, outbending (c) $6.3\text{GeV} < M_{\mu\mu} < 6.6\text{GeV}$, outbending



(d) $5.7\text{GeV} < M_{\mu\mu} < 6.0\text{GeV}$, outbending (e) $6.0\text{GeV} < M_{\mu\mu} < 6.3\text{GeV}$, outbending (f) $6.3\text{GeV} < M_{\mu\mu} < 6.6\text{GeV}$, outbending



(g) $5.7\text{GeV} < M_{\mu\mu} < 6.0\text{GeV}$, inbending (h) $6.0\text{GeV} < M_{\mu\mu} < 6.3\text{GeV}$, inbending (i) $6.3\text{GeV} < M_{\mu\mu} < 6.6\text{GeV}$, inbending



(j) $5.7\text{GeV} < M_{\mu\mu} < 6.0\text{GeV}$, inbending (k) $6.0\text{GeV} < M_{\mu\mu} < 6.3\text{GeV}$, inbending (l) $6.3\text{GeV} < M_{\mu\mu} < 6.6\text{GeV}$, inbending

Figure 4.10: Position of tracks in the magnet focal plane belonging to out- and inbending muon pairs for both data and reconstructed Drell Yan Monte Carlo.

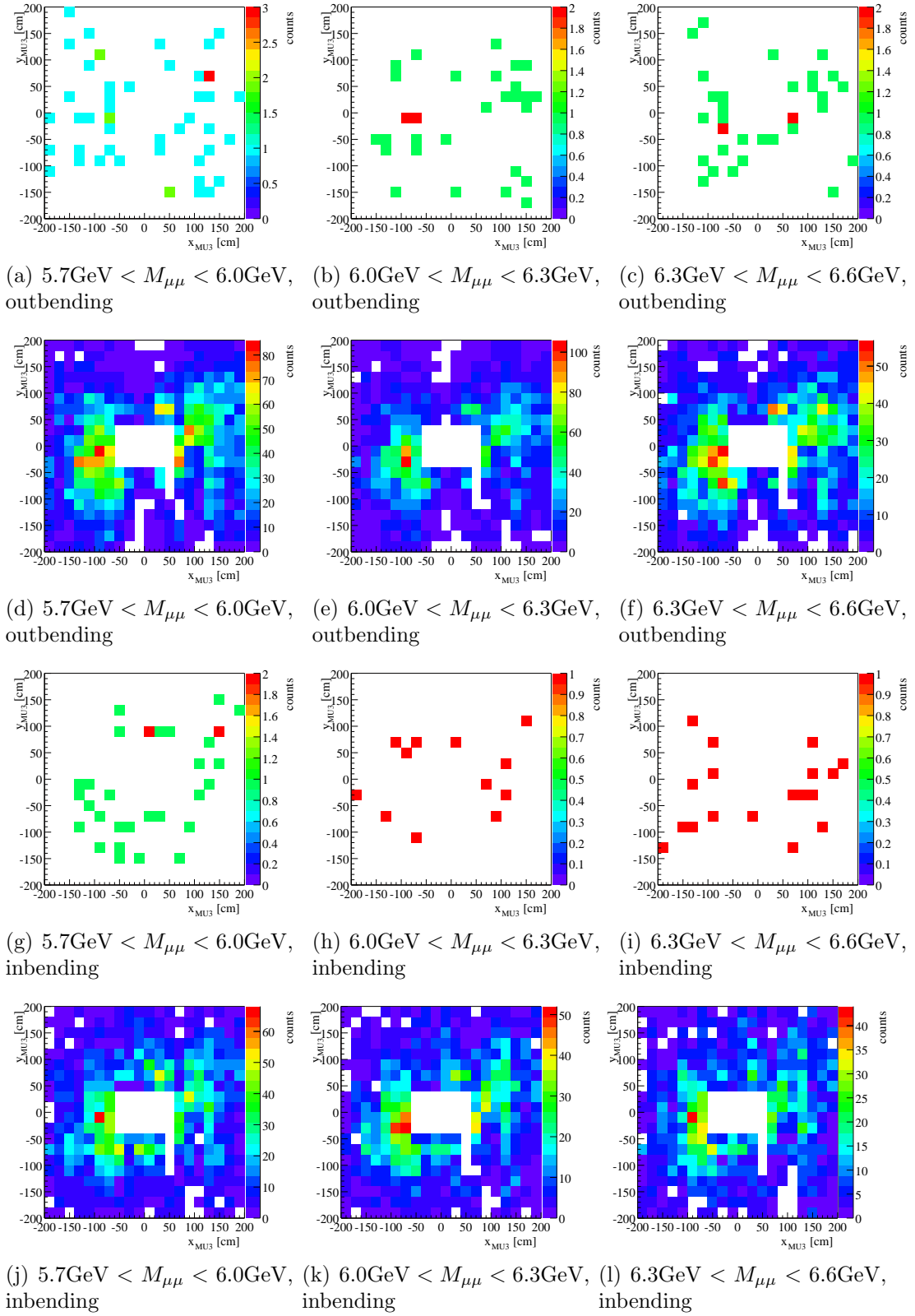


Figure 4.11: Position of tracks in station MU3 belonging to out- and inbending muon pairs for both data and reconstructed Drell Yan Monte Carlo.

4.6 Angular Distributions

As seen in chapter 2.3, the double differential cross section $\frac{d\sigma}{d\cos\theta_{CS}d\phi_{CS}}$ is of special interest. The theoretical prediction including leading order QCD processes is:

$$\frac{1}{\sigma} \frac{d\sigma}{d\Omega} = \left[\frac{3}{4\pi} \frac{1}{\lambda + 3} \right] \left(1 + \lambda \cos^2 \theta + \mu \sin 2\theta \cos \phi + \frac{\nu}{2} \sin^2 \theta \cos 2\phi \right), \quad (4.20)$$

where θ is the polar angle of the positive muon in the rest frame of the virtual photon, and ϕ is the azimuthal angle. λ , μ and ν are variables independent of the angles which take the role of structure functions. If the mass of the virtual photon is small compared to the Z_0 mass, the middle term disappears, $\mu = 0$. The parameters λ and ν are connected by the Lam Tung relation ([Lam80])

$$1 - \lambda - 2\nu = 0 \quad (4.21)$$

While first order QCD corrections have no influence on the Lam Tung relation, higher order corrections point to a slightly positive value of $1 - \lambda - 2\nu$.

A two dimensional fit of equation (4.20) to data yields $\lambda = 0.04 \pm 0.45$ and $\nu = 0.09 \pm 0.16$. This gives for the Lam Tung relation a value of 0.78 ± 0.50 . The data available at HERA-b is not sufficient for a two dimensional fit. Also, the fit function does not describe the data very well, the fit probability is only 1.7% and $\chi^2/\text{ndf} = 58/37 = 1.55$. Because of this, the one dimensional distributions of $\cos\theta_{CS}$ and ϕ_{CS} were also fitted. The distributions and the corresponding fits are shown in Fig. 4.12.

For the fit of the $\cos\theta_{CS}$ distribution, Eqn. (4.20) was integrated over ϕ in the range from $-\pi$ to $+\pi$. The fit result is $\lambda = 0.60 \pm 0.58$. Integrating Eqn. (4.20) over $\cos\theta_{CS}$ in the acceptance range of HERA-b and using the result for λ from the first fit, one gets a value of $\nu = 0.14 \pm 0.14$ from a fit to the ϕ_{CS} distribution. The Lam Tung relation then is $1 - \lambda - 2\nu = 0.12 \pm 0.61$.

Within the large errors, the value of λ is compatible with one, while both the value of ν and the resulting value of the Lam Tung relation is compatible with zero.

Unfortunately the amount of data available does not allow a measurement of the dependance of the coefficients λ and ν on the transverse momentum of the muon pair, which would be necessary to help distinguish between the two theoretical models for the quark correlation presented in Sec. 2.4.2.

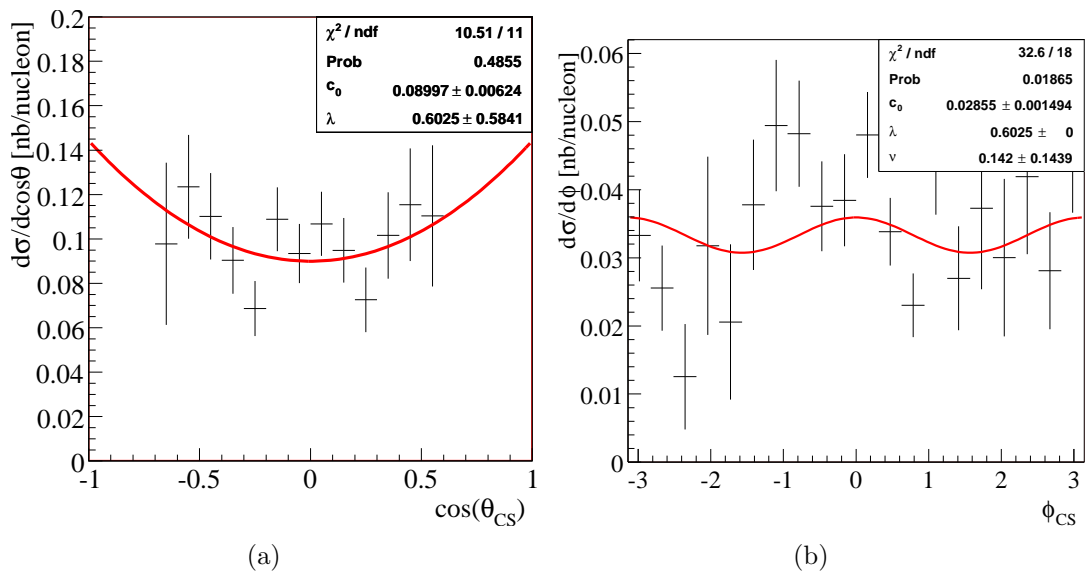


Figure 4.12: One dimensional angular differential cross sections.
 (a) shows $\frac{d\sigma}{d\cos\theta_{CS}}$, (b) $\frac{d\sigma}{d\phi_{CS}}$

4.7 Comparisons with other Experiments

4.7.1 E772

HERA-b is unique compared to other measurements of Drell Yan with respect to the covered x_F range. The sensitive region extends from -0.45 to 0.05 , which corresponds to a back scattering of the incident quark. The experiment E772 ([McG94]) at Fermilab measured the dependence of the Drell Yan cross section on mass and x_F with a mass range of $4.5 \text{ GeV} < M_{\text{DY}} < 13.5 \text{ GeV}$ and an x_F range of $0.0 < x_F < 0.7$. Since the Drell Yan cross section exhibits scaling in the variable $\tau = M^2/s$ and the center-of-mass energies at E772 (38.8 GeV) and HERA-b (41.6 GeV) differ, the mass values of HERA-b were adjusted by the ratio of the center-of-mass energies to be able to compare the cross sections. The comparisons are shown in Fig. 4.13.

A problem can be seen in Fig. 4.13(c), where the measurement from HERA-b is below that of E772. This discrepancy is caused by the problematic mass bin at 6.2 GeV which was described in Sec. 4.5. Apart from this problem, the distributions match very well and extend the measurement performed by E772 into the negative x_F range.

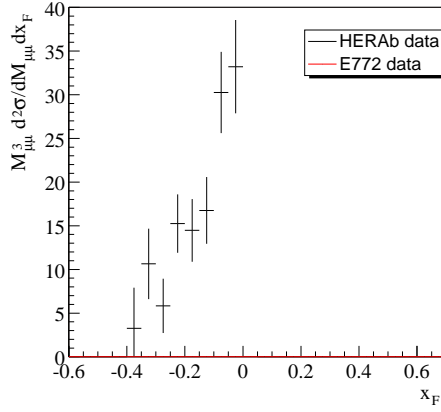
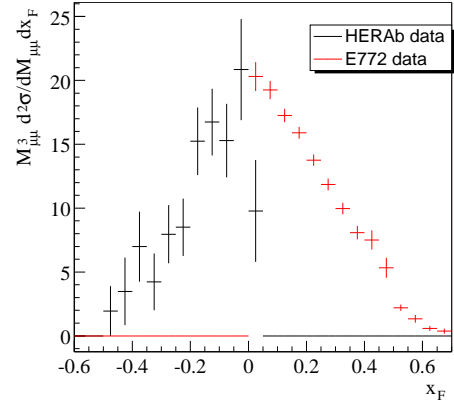
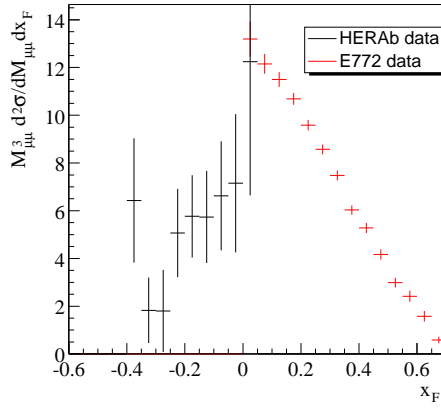
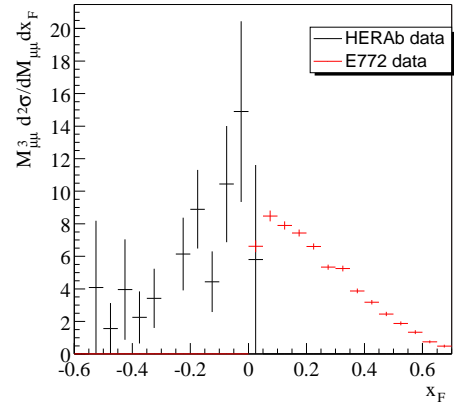
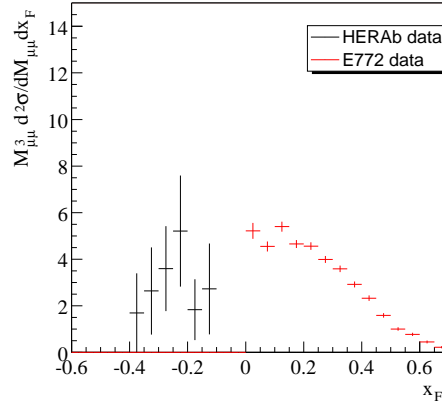
(a) $3.7\text{GeV} < \text{mass} < 4.5\text{GeV}$ (b) $4.5\text{GeV} < \text{mass} < 5.5\text{GeV}$ (c) $5.5\text{GeV} < \text{mass} < 6.5\text{GeV}$ (d) $6.5\text{GeV} < \text{mass} < 7.5\text{GeV}$ (e) $7.5\text{GeV} < \text{mass} < 8.5\text{GeV}$

Figure 4.13: x_F distribution of data from E772 and HERA-b. The data is divided in mass bins, the mass measured at HERA-b was adjusted to the center-of-mass energy of E772. The deviation between data from E772 and HERA-b in plot (c) is caused by the problematic mass bin described in Sec. 4.5.

4.7.2 NA50

The experiment NA50 at CERN is a muon spectrometer situated at the SPS. Here, protons with a beam energy of 450 GeV hit a fixed target of different materials. A dimuon trigger selects events containing bottomonium and the Drell Yan process. A recent publication ([Ale06]) gives transverse momentum distributions of high mass (> 6 GeV at $\sqrt{s} = 29.1$ GeV) Drell Yan events. The paper uses the following function to fit the differential cross section dependence on p_t :

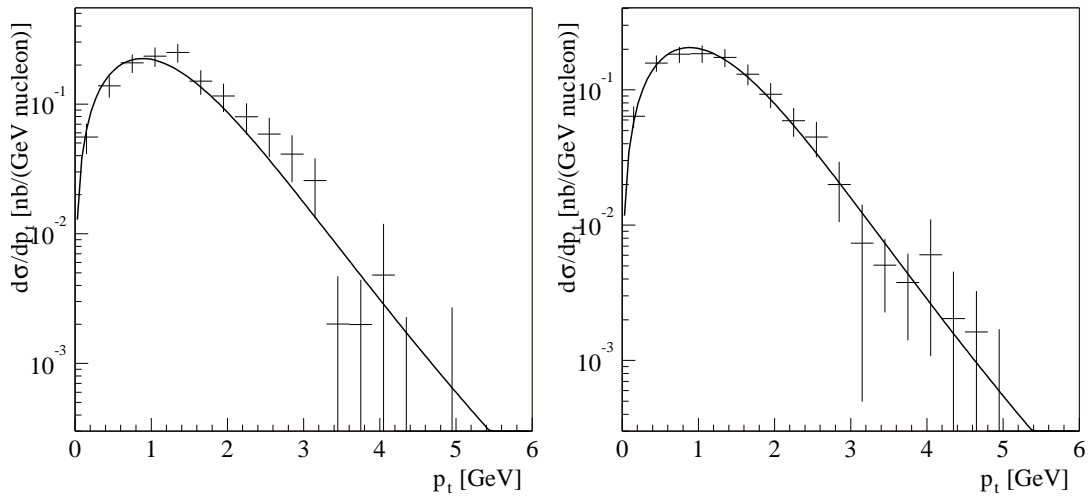
$$\frac{d\sigma}{dp_t} \propto \frac{p_t}{[1 + (p_t/p_0)^2]^6} \quad (4.22)$$

The fitted value of p_0 , the average transverse momentum $\langle p_t \rangle$ and the average transverse momentum squared $\langle p_t^2 \rangle$ are compared for different target materials. The p_t distributions of the data taken at HERA-b are shown in Fig. 4.14, for all data and separately for two of the three target materials. The Titanium data sample taken at HERA-b is too small to be fitted by function (4.22) as it consists of only three Drell Yan events after the data selection.

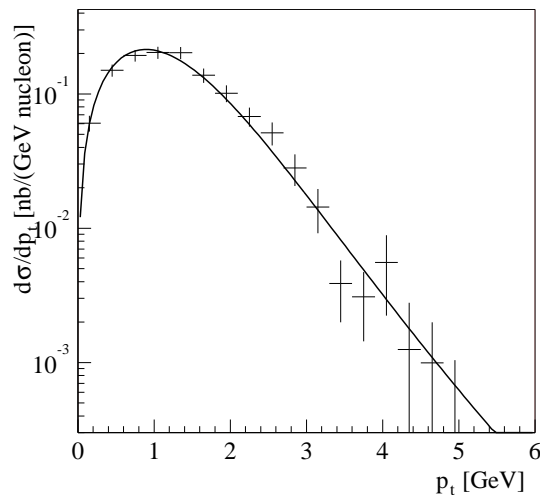
The result of the fit to the three distributions as well as the average transverse momentum values are given in Tab. 4.4. Also given as a comparison are the values from NA50 for a Tungsten target. The measurements agree within their errors, showing no dependency on the target material.

Target	A	p_0 , [GeV]	$\langle p_t \rangle$, [GeV]	$\langle p_t^2 \rangle$, [GeV ²]
All data		2.99 ± 0.05	1.31 ± 0.05	1.49 ± 0.22
W	183.84	2.96 ± 0.08	1.35 ± 0.10	1.75 ± 0.23
C	12.0107	2.94 ± 0.08	1.27 ± 0.08	1.68 ± 0.19
W @ NA50	183.84	2.80 ± 0.03	1.20 ± 0.01	1.96 ± 0.04

Table 4.4: Fit results of p_0 (as defined in Eq. (4.22)), $\langle p_t \rangle$ and $\langle p_t^2 \rangle$ of Drell Yan events in data depending on mass number of the target wire. Also given are the values measured with a Tungsten target at NA50 ([Ale06]).



(a) Drell Yan originating from a Tungsten wire (b) Drell Yan originating from a Carbon wire



(c) All Drell Yan data

Figure 4.14: *Differential cross sections of Drell Yan depending on the transverse momentum of the muon pair. The distributions are fitted with function (4.22). The data sample originating from a Titanium wire is too small to be used.*

4.8 Systematic effects

To study systematic influences on the results, the analysis was repeated several times with changed input parameters. Four sources of systematic errors were identified:

- The reweighting procedure of the likesign data. To check the influence of the Single Track Monte Carlo weights, the binning of the efficiency matrix was changed from 20×10 to 19×11 . A new efficiency matrix was then calculated and used to reweight the likesign data (“stmcc” in Tab. 4.5).
- The reweighting of the Drell Yan Monte Carlo to match the distribution of transverse momentum of the muon pair found in data. The function used to fit the Monte Carlo $M_{\mu\mu}$ vs. p_t^2 distribution was modified slightly by removing the third exponential term (3.15) and using the remaining function to reweight the Drell Yan Monte Carlo (“dymc” in Tab. 4.5).
- The kinematic selection. This influence was checked in two different ways. First, all six cuts applied to data were tightened by 5% each (“hard”), then loosened again by 5% (“soft”). Second, the two cuts with the largest influence on data, the cut on the reduced χ^2 of the track fit and on the transverse track momentum were changed up and down by 5% individually (“ p_t hard”, “ p_t soft”, “ χ^2 hard” and “ χ^2 soft”).
- The determination of the luminosity. As already described in Sec. 4.1, the systematic influence of the fit function used to fit the J/ψ peak and the choice of cuts is negligible compared to the error on the value of the J/ψ cross section from literature.

In Tab. 4.5 the results of the systematic changes above are given. “n.c.” stands for no change and represents the unchanged analysis presented in the last chapters. The systematic influence of the changed Single Track Monte Carlo and the kinematic selection are correlated, as the cuts are also applied to the reweighted likesign distributions. To examine this correlation, the hard and soft cut selection was also applied simultaneously with the STMC change (“hard stmcc” and “soft stmcc”). The last column gives the events in the data sample. Especially the hard and soft cut selections change the size of the sample. This change introduces an additional statistical error, which can be calculated by $\Delta_{stat} = \sqrt{|N_{new} - N_{old}|/N_{new}}$. Since this value is in no sample larger than 2%, it is not sufficient to explain the deviations, which thus are real systematic effects. It can also be seen easily that the changed Drell Yan Monte Carlo reweight function has almost no influence on the results.

Due to the correlations between the samples, the deviations cannot simply be added to get the total systematic error. Some of the correlations are positive, e.g. in the case of ν , where the combined error of STMC reweighting and changed

kinematic selection is larger than the individual contributions. Others are negative as that between STMC reweighting and kinematic selection for the value of λ . Here, the combined deviation of the measurement is smaller than the individual ones. Thus, the largest deviation from the measurement was chosen as the systematical error. The chosen value is marked in bold in Tab. 4.5.

The results of the analysis including statistical and systematic errors are summarized in Tab. 4.6. Except for two values, the systematic errors are smaller than the statistical ones. The first of these is ν . As one can see from Fig. 4.12(b), the fit does not describe the data very well. Small changes of the fitted distribution can easily lead to large changes in the fit. The second value is $p_0(W)$, which is the result from the fit in Fig. 4.14(a). In this distribution the shape of the fit does not quite match the shape of the distribution, which also leads to a larger systematic error.

	σ_{DY} [pb/n]	λ	ν	$p_{0\text{W}}$ [GeV]	$\langle p_{\text{tW}} \rangle$ [GeV]	$\langle p_{\text{tW}}^2 \rangle$ [GeV ²]	$p_{0\text{C}}$ [GeV]	$\langle p_{\text{tC}} \rangle$ [GeV]	$\langle p_{\text{tC}}^2 \rangle$ [GeV ²]	α	#evts
n.c.	289	0.60	0.14	2.93	1.35	2.20	2.93	1.27	1.94	1.03	921
dymc	0	-0.02	0.00	0.00	0.00	0.00	0.00	0.00	0.00	0.00	921
stmC	0	-0.21	-0.04	-0.01	0.00	0.00	-0.02	0.00	0.00	-0.01	924
hard	-11	-0.35	-0.09	-0.02	-0.03	-0.11	-0.01	0.01	-0.01	-0.01	733
soft	-12	-0.35	-0.04	0.13	0.02	0.02	0.01	0.02	0.05	0.03	1022
hard stmC	1	-0.21	-0.16	-0.01	-0.03	-0.11	-0.01	0.01	0.00	-0.02	767
soft stmC	2	-0.27	-0.10	0.13	0.02	0.03	0.00	0.02	0.05	0.03	1074
p_{t} hard	-3	-0.20	-0.05	-0.02	-0.02	-0.05	-0.01	0.01	0.00	-0.01	979
p_{t} soft	-4	-0.47	-0.06	0.14	0.02	0.02	0.00	0.01	0.04	0.02	787
χ^2 hard	-11	-0.01	0.03	0.00	0.01	0.01	0.01	0.00	0.01	-0.01	909
χ^2 soft	+5	-0.12	0.02	0.01	-0.01	-0.03	0.00	-0.01	-0.02	0.00	934

Table 4.5: Influence of systematic effects on analysis results. Given are the deviations from the default analysis values listed in the first row. The top row names the value given below, the left column indicates the change applied to the analysis. The abbreviations of the changes are explained in the text.

α	$1.03 \pm 0.03_{\text{stat}} \pm 0.03_{\text{syst}}$
σ_{DY}	$(289 \pm 35_{\text{stat}} \pm 12_{\text{syst}})$ pb/nucleon
λ	$0.60 \pm 0.58_{\text{stat}} \pm 0.47_{\text{syst}}$
ν	$0.14 \pm 0.14_{\text{stat}} \pm 0.16_{\text{syst}}$
$p_0(\text{W})$	$(2.96 \pm 0.08_{\text{stat}} \pm 0.13_{\text{syst}})$ GeV
$\langle p_{\text{t}} \rangle(\text{W})$	$(1.35 \pm 0.10_{\text{stat}} \pm 0.03_{\text{syst}})$ GeV
$\langle p_{\text{t}}^2 \rangle(\text{W})$	$(1.75 \pm 0.23_{\text{stat}} \pm 0.11_{\text{syst}})$ GeV ²
$p_0(\text{C})$	$(2.94 \pm 0.08_{\text{stat}} \pm 0.02_{\text{syst}})$ GeV
$\langle p_{\text{t}} \rangle(\text{C})$	$(1.27 \pm 0.08_{\text{stat}} \pm 0.02_{\text{syst}})$ GeV
$\langle p_{\text{t}}^2 \rangle(\text{C})$	$(1.68 \pm 0.19_{\text{stat}} \pm 0.05_{\text{syst}})$ GeV ²

Table 4.6: Analysis results including systematic errors.

Chapter 5

Conclusions

In this thesis, the cross section of the Drell Yan process was measured. The data used was gathered at the HERA-b detector, one of the four experiments at the HERA storage ring at DESY in Hamburg, Germany. Unlike other experiments dedicated to measure muon pair production, there is no absorbing material between interaction point and detector at HERA-b. Because of this open geometry the level of background is much higher and presents a difficult challenge. Due to the large background and the low number of events taken during the short data taking period in 2002/2003, the main difficulty was to extract and conserve the Drell Yan events by applying a kinematic selection and subtracting the remaining background. The cross section of the Drell Yan process was determined to be $\sigma_{\text{DY} \rightarrow \mu\mu} = (289 \pm 35_{\text{stat}} \pm 12_{\text{syst}})$ pb/nucleon in the mass range of 4 GeV to 9 GeV. Using the same selection, the Υ cross section was also measured. The result is $Br(\Upsilon \rightarrow \mu^+\mu^-) \cdot \frac{d\sigma}{dy}|_{y=0}(\Upsilon) = (4.9 \pm 1.4)$ pb/nucleon.

Due to the requirement of electrons with opposite charge in the HERA-b dielectron trigger, the extension of the search for Drell Yan to include the dielectron data set was not possible.

After the background subtraction, a difference between measurement and expectation was observed: a significant deviation of Monte Carlo and data was found in the distribution of reconstructed mass of the muon pair. This deviation is also visible in an independant analysis of the same dataset presented in [Abt06]. While no conclusive reason for this discrepancy was found, it is likely that unknown detector inefficiencies are the cause.

The measurement of the double differential cross section $d\sigma/dM_{\mu\mu}dx_F$ performed at the Fermilab experiment E772 ([McG94]) was extended for the first time into the negative x_F range. Except for the mass bin containing the mass deviation mentioned above, the data between the two experiments agree very well.

The distribution of transverse momentum of the muon pair was compared with measurements performed by the NA50 collaboration ([Ale06]). A fit to the p_t distribution and the average p_t and p_t^2 agree within errors. No dependance on the mass number of the target material was found.

A measurement of the A dependence of the Drell Yan cross section $\sigma \propto A^{-\alpha}$ yielded the result $\alpha = 1.03 \pm 0.03_{\text{stat}} \pm 0.03_{\text{syst}}$, which is compatible with one as expected from other Drell Yan measurements, e.g. [Ale06].

Unfortunately, the number of Drell Yan events remaining after the kinematic selection was not sufficient to perform a significant measurement of the angular distributions. The statistical errors of the parameters λ and ν are too large to yield a conclusive result for the Lam Tung relation.

List of Figures

1.1	Overview of the HERA accelerator complex.	7
1.2	Schematic overview of HERA-b.	9
1.3	Schematic view of VDS and Target.	10
1.4	Schematic drawing of a GEM MSGC.	12
1.5	Illustration of the honeycomb structure of the OTR.	13
1.6	Cross section of the RICH.	14
1.7	Overview of the ECAL and drawing of a single cell.	15
1.8	Cutout illustration of the muon system.	16
2.1	Feynman graph of the Drell Yan process at parton level.	19
2.2	Factorisation model of the Drell Yan Process.	21
2.3	QCD corrections to the Drell Yan process.	22
2.4	Theoretical calculation of the differential Drell Yan cross section.	23
2.5	Illustration of the Collins Soper reference frame.	24
2.6	λ , μ and ν as a function of p_t , measured at NA10.	26
2.7	λ , μ and ν as a function of p_t , measured at E615.	27
2.8	Comparison between measurements of λ , μ and ν from NA10, E615 and E866.	28
2.9	Comparison between data from E615 and a Higher Twist simulation.	29
2.10	Comparison between data from E615 and a vacuum fluctuation simulation.	31
2.11	Comparison between data from E615 and a simulation using time reversal (T) odd distribution functions.	32
3.1	Fiducial cuts at stations PC1 and MU3.	34
3.2	Invariant mass of muon data after preselection.	35
3.3	p distribution of muons in Drell Yan Monte Carlo.	37
3.4	Comparison of distributions between likesign and event mixing data.	38
3.5	Difference in acceptance between likesign and unlikesign muon pairs.	40
3.6	x position of muon tracks in the focal plane of the magnet after fiducial cuts.	41
3.7	x vs. y position of muon tracks in station PC1 after fiducial cuts.	41
3.8	Detector regions containing data depending on muon charges.	42

3.9	Efficiency map of the First Level Trigger.	44
3.10	Distributions of p_x and p_y of generated Single Track Monte Carlo muons.	47
3.11	p_x and p_y distributions of Single Track Monte Carlo muons accepted by FLT and SLT.	49
3.12	p_x vs. p_y distribution of Single Track Monte Carlo muons accepted by FLT and SLT.	50
3.13	Track position in the magnet focal plane of Single Track Monte Carlo muons accepted by both triggers.	51
3.14	Distribution of the weights applied to likesign data.	54
3.15	Mass distribution of the data after fiducial cuts and likesign reweighting.	55
3.16	Comparison between the x position of tracks for rec. and reweighted gen. Drell Yan Monte Carlo.	58
3.17	Comparison of kinematic distributions of rec. and reweighted gen. Drell Yan Monte Carlo.	59
3.18	Distribution of the transverse momentum of the muon pair in data and Monte Carlo.	61
3.19	Mass vs. p_t^2 distribution and fit of reconstructed Drell Yan Monte Carlo events.	62
3.20	Mass vs. p_t^2 distribution and fit of data events.	63
3.21	p_t and p_t^2 distribution in data and Monte Carlo simulation after reweighting.	63
3.22	Dependance of signal MC and likesign background on kinematic variables.	68
3.23	Effect of the consecutive kinematic cuts.	69
3.24	x position of tracks passing station PC1 left and right of the insensitive inner region.	70
3.25	x position of tracks passing station PC1 left and right of the insensitive inner region after additional geometrical cut.	71
3.26	Mass distribution of data after cuts and reweighting of likesign background.	72
3.27	Event likelihood distribution for signal and background.	73
3.28	Mass distribution of signal extracted after cuts and background subtraction for both selection methods.	75
3.29	Distribution of the dielectron mass in the J/ψ and Drell Yan mass region.	77
4.1	p_t distribution of J/ψ in data and Monte Carlo.	81
4.2	Invariant mass distribution of the reconstructed muon pair at the J/ψ mass.	83
4.3	Invariant mass distribution of the reconstructed muon pair above 8.6 GeV.	84

4.4	Detector acceptance as a function of kinematic variables.	88
4.5	Acceptance corrected p_t distributions of data, separated according to target material.	91
4.6	Differential cross sections of Drell Yan.	92
4.7	Mass distribution of data after before and after acceptance correction.	93
4.8	Zoomed mass distribution of reconstructed Drell Yan Monte Carlo and data.	94
4.9	Distribution of reconstructed invariant mass of muon pairs as published in [Abt06].	95
4.10	Track position in the magnet focal plane below, in and above the problematic mass region.	96
4.11	Track position in station MU3 below, in and above the problematic mass region.	97
4.12	One dimensional angular distributions.	99
4.13	x_F distribution of data from E772 and HERA-b, separated in mass bins.	101
4.14	Differential cross sections of Drell Yan depending on p_t of the muon pair, separated for target material.	103

List of Tables

3.1	Detector regions at the magnet as defined in Fig. 3.8 which contain data.	44
3.2	Trigger efficiencies in Single Track Monte Carlo.	48
3.3	List of Drell Yan Monte Carlo runs used.	64
3.4	Cuts used in muon analysis.	67
3.5	Preliminary cuts used in the dielectron analysis.	76
4.1	Cuts used in J/ψ selection.	82
4.2	Values used in luminosity calculation.	82
4.3	Values used in the determination of the Υ cross section.	85
4.4	p_0 (as defined in Eq. (4.22)), $\langle p_t \rangle$ and $\langle p_t^2 \rangle$ of Drell Yan.	102
4.5	Influence of systematic effects on analysis results.	106
4.6	Analysis results including systematic errors.	106

Bibliography

- [Abt94] I. Abt et al. (HERA-b Collaboration), *An Experiment to Study CP Violation in the B System Using an Internal Target at the HERA Proton Ring*, DESY-PRC-94-02, Hamburg, Germany, 1994.
- [Abt06] I. Abt et al., *Measurement of the Υ Production Cross Section in 920 GeV Fixed-Target Proton-Nucleus Collisions*, hep-ex/0603015, Hamburg, Germany, March 2006
- [Ada05] A. Adametz, *Preshower Measurement with the Cherenkov Detector of the BABAR Experiment*, Diploma thesis, Universität Heidelberg, Germany, 2005
- [Alb95] H. Albrecht, *ARTE. (Analysis and Reconstruction Tool)* HERA-b Internal Note 95-065, DESY, Hamburg 1995
- [Ale06] B. Alessandro et al. (NA50 Collaboration), *Bottomium and Drell-Yan production in $p-p$ collisions at 450 GeV*, Phys. Lett. B 635 (2006), 260-269
- [And84] L. Anderson et al. (NA10 Collaboration), *A High Resolution Spectrometer for the Study of High Mass Muon Pairs Produced by Intense Hadron Beams*, Nucl. Instr. Meth. A223 (1984), 26
- [Ari04] I. Arino et al., *The HERA-b Ring Imaging Cherenkov Counter*, Nucl.Instrum.Meth.A516:445-461, 2004
- [Bag02] Y. Bagaturia et al., *Studies of aging and HV break down problems during development and operation of MSGC and GEM detectors for the inner tracking system of HERA-b*, ICFA Instrum. Bull. 24 (2002), 54–84
- [Bal03] V. Balagura, *Efficiency Map Viewer*, 2003, /hb/fit/balagura/eff_map-viewer/viewer
- [Bar05] M. Bargiotti et al., *J/ψ production cross section at $\sqrt{s} = 41.6$ GeV by means of NRQCD calculations*, HERA-b note 05-015, DESY, Hamburg, 2005
- [Bau03] C. Bauer et al., *Performance of the HERA-B vertex detector system*, Nucl. Instrum. Meth. A501 (2003), 39-48.

- [Bii86] C. Biino et al. (E615 Collaboration), *An Apparatus to Measure the Structure of the Pion*, Nucl. Instr. Meth. A243 (1986), 323
- [Boe99] D. Boer, *Investigating the Origins of Transverse Spin Asymmetries at RHIC*, Phys. Rev. D60 (1999) 014012
- [Boe05] D. Boer, A. Brandenburg, O. Nachtmann and A. Utermann, *Factorization, Parton Entanglement and the Drell-Yan Process*, Eur. Phys. J. C 40, 55-61 (2005)
- [Bra93] A. Brandenburg and O. Nachtmann, *Spin Effects and Factorization in the Drell-Yan Process*, Z. Phys. C60 (1993), 697-710
- [Bra94] A. Brandenburg, S.J. Brodsky, V.V. Khoze and D. Müller, *Angular distributions in the Drell-Yan process: A Closer look at higher twist effects*, Phys. Rev. Lett. 73 (1994), 939-942, hep-ph/9403361
- [Brä01] M. Bräuer, *Die Alignierung des HERAB Vertexdetektors*, Ph.D. thesis, Universität Heidelberg, Germany, 2001
- [Bru02] M. Bruinsma, *Performance of the First Level Trigger of Hera-B and Nuclear Effects in J/ψ Production*, Ph. D. thesis, Universiteit Utrecht, Netherlands, 2002
- [Bru05] M. Bruschi, *Luminosity Determination at HERA-b*, HERA-b Internal Note 05-011, DESY, Hamburg, 2005
- [Cal69] C.G. Callan and D.J. Gross, *High-energy electroproduction and the constitution of the electric current*, Phys. Rev. Lett. 22 (1969) 156
- [Cer94] CERN, *GEANT 3.21 detector description and simulation tool*, CERN Library Long Writeup W5013, CERN, Genève, 1994
- [Cha03] *Webpage of the Charmonium Analysis Group*, <http://www-hera-b.desy.de/subgroup/physics/herab/analysis/cc2003/welcome.html>, 2003
- [Col77] J.C. Collins, D.E. Soper, *Angular distributions of dileptons in high-energy hadron collisions*, Phys. Rev. D16 (1977) 2219
- [Col89] J.C. Collins, D.E. Soper and G. Sterman, *Factorization of hard processes in QCD*, Perturbative QCD, ed. A.h. Mueller, World Scientific (1989) 1
- [Con89] J.S. Conway et al. (E615 Collaboration), *Experimental study of muon pairs produced by 252-GeV pions on tungsten*, Phys. Rev. D39 (1989), 92
- [Dam04] M. Dam et al., *HERA-b Data Acquisition System*, Nucl. Instrum. Meth. A525:566-581, 2004

- [Des00] DESY, Hamburg, *Press and Public Relations Department*, 2000
- [Dre70] S.D. Drell and T.M. Yan, *Massive lepton-pair production in hadron-hadron collisions at high energies*, Phys. Rev. Lett. 25, 316 (1970); Ann. Phys. (NY) 66, 578 (1971)
- [Egb02] K. Egberts, H. Rick, *A Background Generator for Muons from Decay in Flight of Charged π and K Mesons*, HERA-b Internal Note 02-044, 2002
- [Fey69] R.P. Feynman, *Very high-energy collisions of hadrons*, Phys. Rev. Lett. 23 (1969) 1415
- [Gle01] T. Glebe, *Cluearte 0-42 - The ARTE Interface to BEE*, HERA-b Internal Note 01-110, DESY, Hamburg, 2001
- [Gra01] W. Gradl, *The Readout System of the HERA-B Inner Tracker and Prospects of HERA-B in the Field of Drell-Yan Physics*, Ph. D. thesis, Universität Heidelberg, Germany, 2001
- [Gor03] I. Gorbunov, *ITR Performance for Analysis*, talk given at Coll. Meeting, May 12-16th 2003, also HERA-b Internal Note 03-027, DESY, Hamburg, 2003
- [Gua88] M. Guanzioli et al. (NA10 Collaboration), *Angular distributions of muon pairs produced by negative pions on deuterium and tungsten*, Z. Phys. C37 (1988), 545
- [Har95] E. Hartouni et al. (HERA-b Collaboration), *HERA-b - An Experiment to Study CP Violation in the B System Using an Internal Target at the HERA Proton Ring*, Technical Design Report, DESY-PRC 95/01, January 1995
- [Hul02] W. Hulsbergen, *A Study of Track Reconstruction and Massive Dielectron Production in HERA-b*, Ph. D. thesis, Universiteit van Amsterdam, Netherlands, 2002
- [Hus05] U. Husemann, *Measurement of Nuclear Effects in the Production of J/ψ Mesons with the HERA-B Detector*, Ph. D. thesis, Universität Siegen, Germany, 2005
- [Kis99] I. Kisel, S. Masiocchi, *CATS - A Cellular Automaton for Tracking in Silicon for the HERA-B Vertex Detector*, HERA-b Internal Note 99-242, 1999
- [Lam80] C.S. Lam and W.-K. Tung, *Parton-model relation without quantum-chromodynamic modifications in lepton pair production*, Phys. Rev. D21 (1980), 2712

- [Lei00] M.J. Leitch et al (E866/NuSea Collaboration), *Phys. Rev. Lett.* 84 (2000) 3256
- [Pdg06] Particle Data Group, *Review of Particle Physics*, *J. Physics G: Nucl. Part. Phys* 33 1., 2006
- [Pi92] H. Pi, *An event generator for interactions between hadrons and nuclei: FRITIOF version 7.0*, *Comput. Phys. Commun.* 71 (1992), 173-192
- [Mas00] Silvia Masciocchi, Private Communication, May 2000
- [McG94] P.L McGaughey et al. (E772 Collaboration), *Cross-sections for the production of high mass muon pairs from 800-GeV proton bombardment of H-2*, *Phys.Rev.D50:3038-3045*, 1994, Erratum-ibid.D60:119903, 1999
- [Mor91] G. Moreno et al. (E605 Collaboration), *Phys. Rev. D* 43 (1991) 2815
- [Nee92] W. L. van Neerven and E. B. Zijlstra, *The $\mathcal{O}(\alpha_s^2)$ corrected Drell-Yan K-factor in the DIS and $\overline{\text{MS}}$ schemes*, *Nucl. Phys. B* 382, 11 (1992)
- [Otr02] *Webpage of the HERA-b OTR group*, <http://www-hera-b.desy.de/subgroup/detector/tracker/outer/>, 2002
- [Ric03] H. Rick, private communication, Spring 2004
- [Sch01] B. Schwenninger, *Das Myon-Pretrigger-System für das HERA-bB Experiment*, Ph.D. thesis, Universität Dortmund, Germany, 2001
- [Spe04] J. Spengler, *HERAB detector components*, <http://www-hera-b.desy.de/subgroup/detector/>, 2004
- [Sjö94] T. Sjöstrand, *High-energy physics event generation with PYTHIA 5.7 and JETSET 7.4*, *Comput. Phys. Commun.* 82 (1994), 74-90
- [Spi04] A. Spiridonov, *Bremsstrahlung in Leptonic Onia Decays: Effects on Mass Spectra*, HERA-b Internal Note 04-016, 2004
- [Web02] J. Webb, *Measurement of Continuum Dimuon Production in 800-GeV/c Proton-Nucleon Collisions*, New Mexico State University, Sept 2002
- [Zhu06] L.Y. Zhu, *Measurement of Angular Distributions of Drell-Yan Dimuons in $p + d$ Interaction at 800 GeV/c*, arXiv:hep-ex/0609005, Sept 2006

Danksagung

Zuallererst möchte ich mich bei Herrn Prof. Eisele für die Gelegenheit, beim Experiment HERA-b mitzuarbeiten, bedanken. Nach meiner Diplomarbeit in der Designphase eines Detektors war es sehr aufregend, an einem laufenden Detektor mitzuwirken. Außerdem konnte ich jederzeit mit Fragen zu ihm kommen, wenn mal wieder eine Untergrundbetrachtung im Sande zu verlaufen schien.

Bei Herrn Prof. Knöpfle möchte ich mich für die Bereitschaft, die Zweitkorrektur dieser Arbeit zu übernehmen und die nette Zusammenarbeit in Hamburg bedanken.

Ich danke meinen ehemaligen Inner Tracker Kollegen Juri Bagaturia, Iouri Gorbounov, Sonja und Wolfgang Gradl, Carsten Krauss, Hartmut Rick, Stefan Rieke, Roger Wolf und Torsten Zeuner, die mich in die Geheimnisse von ARTE, Rooibostee und BEE einführten, in dieser Reihenfolge.

Meinen Heidelberger Kollegen möchte ich dafür danken, dass sie mir immer wieder zuhörten und eine sehr angenehme Arbeitsumgebung schafften. Christoph Werner ertrug die meisten Fragen und gewann den Kampf der Teemauern eindeutig, Matthias Mozer stand immer bei Fragen zu Root und Nethack zur Verfügung. Aleksandra Adametz, Johannes Albrecht, Dr. Stephanie Hansmann-Menzemer und Stefan Schenk halfen besonders durch ihre Bereitschaft, diese Arbeit Korrektur zu lesen. Tanja Haas gebührt Dank für ihren unerschöpflichen Optimismus und ihre gute Laune, die durch das Zusammenschreiben half.

Ohne die ständige Unterstützung, Anteilnahme und Liebe meiner Eltern wäre weder mein Studium noch diese Arbeit jemals zustande gekommen. Auch wenn sie dies bereits wissen und mein Vater daher eine Reinkarnation als sein eigener Sohn plant: Danke für Alles, Ihr seid die Besten.

My American family, the Crowells took an unknown boy into their home, gave him their love and helped him grow up. It was there that I decided to study physics. Thanks for all your support and love throughout the years, Mom, Dad and Grandma.

Meinen Schwiegereltern möchte ich mich für die Aufnahme in ihre Familie und die Gebete danken.

Meiner Gilde danke ich für den Ausgleich zur Arbeit. Gegenschlawüt!

Mein besonderer Dank gilt meiner Frau Salma, deren Liebe mich durch alle Tiefen im Laufe dieser Arbeit trug. Enhebek Habibti.

Widmen möchte ich diese Arbeit meinen beiden Großmüttern Oma Katrin und Oma Liesel, die mich im Studium sehr unterstützt haben, dessen Abschluss sie aber leider nicht mehr miterleben durften.